Data Evaluation, Analysis and Scientific Study

NAS8-36955 D. O. 19

FINAL REPORT

Submitted by
UAH

Dr. S. T. Wu
Principal Investigator
Department of Mechanical Engineering and
Center for Space Plasma and Aeronomic Research
The University of Alabama in Huntsville
Huntsville, AL 35899
(205) 895-6413

Submitted to:

National Aeronautics and Space Administration
George C. Marshall Space Flight Center

Extensive work was performed in data analysis and modeling of solar active phenomena. The work consisted in the study of UV data from the UVSP instrument on board the Solar Maximum Mission satellite. These data were studied in conjunction with X-rays from the HXIS instrument, and with H-alpha and magnetographic data from ground-based observatories.

The processes we studied are the active phenomena which results from the interaction of the solar magnetic fields with the plasma in the outer regions of the solar atmosphere. These processes include some very dynamic processes such as the prominence eruptions and the "microflares". Our research aimed at characterizing: the observed phenomena, the possible physical models, and the relevance to the chromospheric and coronal heating. As a product of our research we are enclosing published, in press, and submitted papers which show the progress achieved in our research.

This research has lead to improved insight in the processes of "microflaring" which occur almost continuously in active regions. Also, we have made significant progress in the understanding of prominence eruptions. These phenomena are important both, for the understanding of the interaction of magnetic fields with dense plasmas, and for the effects they have in the earth upper atmosphere. Our research gives important background in the constraining of the possible physical mechanisms and in the intensity and distribution of the different emissions in the UV, X-ray, and optical.

We refer the reader to the appendix of copies of eleven papers for a more complete description of the work performed. Some of these papers contain observational studies while others contain theoretical developments necessary for interpreting and modeling the data.

APPENDIX

Submited to Astron. Ap.

A Microflare-Related Activation of a Filament Observed in Hα and C IV Lines

by

B. Schmieder

Observatoire de Paris, Section de Meudon
F92195 Meudon Principal CEDEX, France

J. Fontenla and E. Tandberg-Hanssen

Space Science Laboratory
Marshall Space Flight Center
NASA, Huntsvile, AL 35812 USA

Abstract

A filament in active region 2717 was observed in two lines formed at different temperatures (Hα at 10^4 K and C IV at 10^5 K) with the Multi-Channel-Double-Pass (MSDP) spectrograph and the Ultraviolet Spectrometer and Polarimeter (UVSP). The partial disparition brusque (DB) of the filament as observed in Hα was due to the heating of a filament section in the vicinity of a bright point. A propagating disturbance followed this event. A detailed analysis of C IV rasters shows that this disturbance was not a passive perturbation, but was itself triggering active phenomena at various locations along its path, resulting in energy releases. We suggest that this propagation of brightness was due to fast successive reconnections between fine loop-like structures of the filament.

1. Introduction

Prominences are frequently subjected to instabilities which, in extreme cases, may lead to their destruction. For reviews of prominence instabilities see Schmieder (1989, 1990). When the prominence instability results in an eruption, generally referred to as a dynamic disparition brusque (DB), the escaping material may reach velocities of several hundred km/s (Raadu et al., 1987; Rompolt, 1990). In less catastrophic cases the prominence rises slowly or untwists (Schmieder et al., 1985, Vrsnak et al., 1988).

The proposed trigger for these dynamic instabilities of prominences is a disturbance of the magnetic field that supports the prominence. The disturbance may be due to submergence of flux (Hermans and Martin, 1986), new emerging flux (Martres and Soru-Escaut, 1977; Raadu et al., 1988), or global evolution of large regions on the Sun (Schmieder et al., 1989, 1990).

Prominences or filaments (i.e., prominences seen in absorption against the solar disk) are also observed to disappear in situ, i.e., they disappear in Hα while still visible in higher temperature spectral lines. This phenomenon of sudden heating of the prominence plasma has been described by Mouradian et al. (1981) Simon et al. (1984), and Mouradian and Soru-Escaut (1989) and the thermal destabilization has been studied by Kuin and Martens (1986) and Démoulin and Einaudi (1989). In many cases we do not have either a clear-cut dynamic eruption or a heating phenomenon; the two types of instability co-exist (Widing et al., 1986, Fontenla and Poland, 1989), and ultimately a magnetic trigger may be the cause in both types of destabilization. For instance, in the magnetically unstable case, twisted magnetic flux tubes in the prominence may become unstable and lead to eruption (Hood and Priest, 1980), while reconnection between the tubes would lead to extra heating (van Ballegooijen and Martens, 1989; Küijpers, 1989). This

extra heating may start a runaway process of thermal instability (Poland and Mariska, 1986).

In this paper we study a filament destabilization observed simultaneously on 9 October, 1988 in the Hα and C IV 1548 Å lines, and with Doppler shift measurements in both lines. The Hα observations lead to the detailed knowledge of the geometry of the filament and show the onset of mass motions in the filament as a result of its destabilization. The observations in C IV show that dynamic and heating disturbances propagate along a large portion of the filament. The filament destabilization appears related to the development of an underlying microflare or bright point. First, in order to show the filament destabilization that we focus on in an evolutionary context, we present data on the activity in the active region obtained at Debrecen 2 to 4 hours before the Hα and C IV observations. Then we study, in detail, the sequence of events to discern the nature of the filament destabilization and to show the role of the thermal and magnetic processes.

2. Instrumentation

The present detailed study of this filament-flare interaction is made possible by combining data obtained with three different instruments; viz. the spectrograph and the magnetograph at Meudon and the UV spectrograph on the Solar Maximum Mission, supplemented with additional information from Hα and white-light photos obtained at Debrecen.

a. The Meudon spectrograph

The MSDP spectrograph simultaneously records nine images of a 1 x 8 arc min field-of-view with a resolution of 1-2 arc sec taken in nine different wavelengths 0.3 Å apart in the Hα profile. In this case, successive images

were taken 1 min apart. At each time-step maps of intensity fluctuations and Dopplershifts were computed from the nine points in the profiles using the technique described by Mein (1977). The intensity and velocity values are referenced to a mean value obtained over the whole field-of-view, excluding flaring and sunspot areas. The intensity difference ΔI is negative for the filament and sunspots and positive for faculae. The units are such that a value of $\Delta I = -0.01$ means that the intensity is 0.1% lower than the mean intensity value. The velocity (V) is calculated in units of km s^{-1}. Positive velocity values indicate blueshifts, negative redshifts. The observation with the MSDP was continuous during the orbit of the UVSP, but the Hα observations between 12:27:34 and 12:48:04 UT are not useful because of bad seeing.

b. The Meudon magnetograph

The data processing of the Meudon magnetograms is described by Rayrole (1981). The measurements are made in the photospheric line of FeI λ 5302 Å, and intensity, radial velocity, and magnetic field B are obtained. The spatial resolution is 1.2 x 2 arc sec^2 and the field-of-view size in 4 x 4 arc min^2.

c. The UV spectrograph

The UVSP instrument has been described by Woodgate et al. (1980). The relevant UVSP observations started at 12:27:47 UT with a large raster covering a 4 x 4 arc min^2 field-of-view. The pixel size was 3 x 3 arc sec^2 and data were obtained from two detectors in the Doppler mode for the C IV 1548 Å line. The positioning of the slits and detectors was such that we obtained signals from the core and both wings of the line. From these signals and using the procedure outlined by Fontenla et al. (1989), we obtained the

two signals corresponding to intensity and Dopplershift. However, the Doppler-shift signal should be treated with caution because: (i) the line may contain several differently-shifted components resulting from various structures along the line-of-sight, and (ii) the positioning of the slits and detectors did not correspond to the ideal centered setup. With these points in mind the Doppler data should only be interpreted as indicating changes in the line due to a relative increase in one wing with respect to the other, which corresponds to the presence of a Doppler-shifted emission. From 12:35:22 to 12:45:57 UT, sequences of a smaller field-of-view (1 x 1 arc min^2) were taken with a cadence of one every 31.4 s. Subsequently other similar data sets were secured until 13:26 UT, thus covering practically the total duration of the event considered here. We have combined all data sets to obtain a long sequence of small raster observations describing the behavior of the C IV line for almost an hour.

d. The Debrecen instruments

Both white-light and Hα filtergrams were observed at the Heliophysical Observatory in Debrecen and at its Gyula observing station. The data give white-light images with 10.4 cm diameter at the secondary focus of the telescope and Hα filtergrams from a 53 cm Nikolsky-type coronograph equipped with an 0.5 Å Halle filter. The observing sequences consist of five frames (at Hα ±1 Å ±0.5 Å, and line center) and are referred to as the Hα quintets (Dezso et al., 1988). These instruments were not operating during the orbit of the UVSP (12:35 to 13:36 UT) but provided important data during the period between 07:00 and 10:00 UT.

3. Optical Observations

a. Previous activity

Active region 2717 (N14, E24) had been studied for some time in Hα and white-light prior to the occurrence of the small flare detected in C IV. In Fig. 1 we show two brightenings of facular points, one located in the eastern part of the filament at 07:48:27 UT and one in the central part at 08:12:31 UT in the same location where the small C IV flare occurred later, at 12:35 UT. Parts of the filament close to the bright points became visible in the far wings of the Hα line (±1.0 Å from line center), indicating the presence of either enhanced turbulence (Doppler broadening) or twisting motions. At the location of the bright points we noticed that the filament was no longer visible. This filament disappearance was related to certain changes in the magnetic pattern. If we compare the two white-light images (Fig. 1), we notice the appearance of two new pores just below the end of the filament close to the bright point of 08:12 UT. We surmise that the pore activity was associated with emerging magnetic flux and the evolution of the overlying magnetic field.

This release leads to thermal or dynamic events of varying importance. The two first events were well observed at Debrecen; the third event was recorded with the MSDP spectrograph in Hα and with the UVSP in the C IV line. Both these instruments give velocity values with good timing: every minute for the MSDP and every 15 s for the UVSP.

b. Bright points

Figures 2a and 2b show Hα intensity and velocity maps obtained with the MSDP. Two bright regions are present in the corridor of the filament. One is located at the eastern footpoint of the filament (point BE) with the

remaining brightening of the subflare observed at 07:48 UT at Debrecen; the other is located in the central part of the filament (point BP). Bright point BP as seen in Hα corresponds well to that in C IV (next paragraph), while bright point BE is outside the field-of-view of the UVSP. These points still have an absorption profile but with an Hα line center intensity 10% larger than that of the mean chromosphere. This intensity corresponds to bright facular or subflaring regions. The observed peak intensity occurred for BE at 13:22 UT, while three maxima in BP occurred at 12:48, 13:02, and 13:22 UT.

During these small flares the Hα filament disappeared near the location of the bright points. This behavior is consistent with heating of that section of the filament to temperatures at which hydrogen becomes ionized and the Hα emission vanishes (becomes too optically thin). The presence of heating is confirmed by the enhanced UV emission in the area surrounding the bright points.

Further, it is interesting to note that we observed, at the location of point BE, a sudden formation of filament around 13:14 UT, like an eastern extension of the active filament (Fig. 2a). Chromospheric fibrils were previously visible at 12:54 UT at this location. They came close together to form an extension of the filament. This new section was visible in all channels of the MSDP instrument. The Hα lines were broadened, which confirms the existence of increased turbulence or unresolved twisting motions.

c. Velocity field in the filament

During the entire observing time, we observed great activity in the filament, which was visible in the extreme channels of the MSDP; i.e., we noticed structures in the extreme blue channel and some in the red channel. The magnitudes of the measured velocities were relatively high. We used the

standard method to determine the velocities. Consequently we only found lower limits to the velocities. A "cloud method" (Beckers, 1964) would give values 4 times larger than the standard method (Schmieder et al., 1988). The Hα velocity field was basically stationary. In the western part (W) a redshifted, elongated area was observed with some discrete blue shifts in the southern part, suggesting flows along loops aligned with the axis of the filament.

In the eastern part (E), we mainly observed redshifts, with some blueshifted areas in the northern portion, suggesting a series of loops crossing the magnetic inversion line at a non-negligible angle (Fig. 2 at 12:47 UT). A loop-like structure can be well identified close to BP with a persistent upflow (3 km s^{-1}) east of BP and a downflow (-4 km s^{-1}) located 20 arc sec away toward the east. Close to BE, strong downflows (7 km/s) were registered. The individual small structures in the Hα filament could be followed over 5 or 10 minutes. The evolution of the global feature continued for over 1 hour.

d. Magnetic field

Apparently the photospheric magnetic field was very weak in the whole filament region and not as well defined as is usually the case in active region filaments (Fig. 3). The bright point was located in a magnetic field intrusion on the magnetic polarity inversion line, underlying most of the filament. The longitudinal magnetic field at the location of the bright point was between 140 and 170 G, which corresponds to weak facular fields, but this location was close to a strong gradient of the field.

4. C IV observations

a. Previous data on the filament

As in most cases an Hα filament has a C IV emission counterpart, albeit of quite low intensity. The appearance of the filament prior to the occurrence of the brightening we studied is shown in Fig. 3. In this figure we have saturated the brightest facular areas in order to show the overall aspect of the region and the filament. The filament was visible but faint in the C IV line during this early period, and an enhanced emission area was visible to the east of the location at which BP occurred. This emission did not have an Hα counterpart, and may have corresponded either to a filament which was invisible in Hα or to a location of enhanced coronal heating where the transition region had increased emission but where the upper chromosphere did not.

b. The small flare (or bright point)

In Fig. 4 we show some selected frames in the C IV line (using the composite intensity signal). The figure has two panels; one shows the evolution of the small flare, while in the other the flare is saturated to show the dimmer features. The figure shows the compactness of the flare and its large contrast with the facular area and also displays the morphology of the surrounding area.

Some enhancement in the bright point (3200 counts) was already observed at 12:34:11 UT. At the time we found no significant velocity features associated with the event we studied. The sharp peak intensity of about 8000 counts (about 2×10^5 erg cm^{-2} s^{-1} $ster^{-1}$) was reached at 12:37 UT, lasting for not more than 30 s. This intensity is about 80 times that corresponding to the average quiet Sun. To show the location in the UVSP field-of-view of

the bright point and the east and southwest section of the filament we have indicated their mutual relationship in Fig. 5.

In Fig. 6 we show plots of the time evolution of the intensity of the bright point and surrounding pixels. After the main spike the intensity decayed for about 10 min. However, this decay may have consisted of several similar progressively smaller short-lived secondary events, some of which can be well identified. The different distribution of the intensity in these secondary events between consecutive pixels indicates that several slightly offset small locations were involved in these events. Some low level brightenings appeared later between 12:54 and 13:05 UT and a strong, fast spike reaching 4000 counts occurred at 13:10 UT. This last spike was brightest at the pixel to the north of the 12:37 UT event, indicating that a different magnetic structure was involved. All the fast spikes lasted for less than 30 s and had fast rise and decay times. In other words, they were similar to the microflares studied by Porter et al. (1984) in a different active region.

c. Propagating disturbances

Several brightenings were seen in C IV at various locations through the filament as a result of some disturbance originated by the small flare or bright point (BP). These brightenings did not reach the large values found in the BP, however, they were very significant as Fig. 4b shows. The brightenings appeared in two groups which seem related to the events in the BP, but their temporal structure was different, and even at the pixels close to the BP the brightenings were substantially non-simultaneous (by several minutes). This indicates that the evolution was not just a propagation of a passive perturbation, but that the propagating disturbance actually triggered

active phenomena at various locations. Another characteristic displayed by the brightenings is that they showed fast spikes, sometimes not as fast as the BP, and the slow varying background enhancements were relatively more important than at the BP.

One key feature shown by the brightenings is the spatial structure of the time variations. This structure is shown by the presence of particularly well-defined spikes in adjacent pixels. The presence of the spikes and their relative intensities define several spatial structures that suddenly brightened and decayed almost simultaneously. Some of this behavior is evident in Fig. 4b. However, more complete information is displayed in Fig. 7 which shows the temporal variation of the composite intensity (1 count ≡ 25 erg cm^{-2} s^{-1} $ster^{-1}$) for the pixels which correspond to the filament. These include the two sections of the filament (E and SW), and the C IV enhanced area (A) slightly to the north of the filament.

We find that the brightenings in these areas have some common characteristics and some differences. Between the common characteristics we mention that the individual spikes which define a structure were almost simultaneous in the adjacent pixels but delays of up to 1 min are apparent over distances of about 6000-7000 km. From these data we deduce a value of about 100-300 km s^{-1} for a "phase" velocity representing the propagation of a spike within a spatial structure.

However, the group of spikes seems to have reached maximum later as it moved farther from the BP. This gives a "group" velocity substantially lower than the "phase" velocity, and we find systematic differences between the enhanced area (A) and both filament sections. Also the relative amplitude of the two groups of brightenings and the velocity signature were different in area (A) and in both filament sections.

The amplitudes of the first groups of brightenings which occurred along the E section of the filament were larger than the amplitudes in the second group. The brightenings occurred as early as 12:40 UT (i.e., 3 min after the peak at the BP) at a distance of about 15,000 km to the south. But the maximum emission (of 600 counts $\equiv 1.5 \times 10^4$ erg cm^{-2} s^{-1} $ster^{-1}$) was only reached at 12:45 UT. We estimate a "group" velocity of 30 km s^{-1} along the filament. Also, we find that the individual spatial structures of the spikes extended for up to about 7000 km. The "phase" velocity seems to have been closer to our lower limit of 100 km s^{-1}, but this figure is highly uncertain because of the limited temporal resolution. Similar behavior is found for the second group of spikes whose maximum occurred around 13:02 UT at a distance of about 15,000 km from the BP.

The brightenings of enhanced area A showed the first group of spikes delayed and relatively small in comparison to the corresponding E section of the filament. This first group of spikes reached maximum around 12:48 UT at about 19,000 km from the BP. The second group of spikes was larger and reached about 900 counts (2×10^4 erg cm^{-2} s^{-1} $ster^{-1}$) at around 13:01 UT in a pixel 19,000 km from the BP. We estimate a "group" velocity of about 100 km s^{-1}, which is higher than that in the corresponding E filament section. Also the individual spatial structures seem longer and reached about 13,000 km.

The brightenings of the SW section of the filament showed the first group of spikes practically absent except in the portion close to the BP and in a structure close to its southern end. The first spike occurred in this last location at about 12:47 UT with a peak intensity close to 700 counts (1.7×10^4 erg cm^{-2} s^{-1} $ster^{-1}$). We note that this energy (of more than 10^{23} erg) can hardly have been transported from the BP, because no signs of such

transport were seen in several intermediate pixels between this structure and the BP.

The second group of brightenings appeared in most of the SW section of the filament and reached a peak of about 1000 counts (2.5×10^4 erg cm^{-2} s^{-1} $ster^{-1}$) in the extreme SW part of the filament at about 13:00 UT. The 1-2 min time delay of the spike to travel 13,000 km to the N gives a disturbance propagation velocity of 100-200 km s^{-1}. The structure of the brightness in the SW section of the filament indicates that phenomena similar to that in the E section, occurred here. But the propagation of the second group of brightenings in the SW section of the filament was toward the BP, while in the E section the brightenings propagated away from the BP.

d. The Velocity disturbances

We mentioned that our data cannot quantitatively measure velocities in events like the one we studied which showed complex spatial structures and rapid fluctuations. This is mainly because of the limited temporal, spatial, and spectral resolution of these data. Because of the limited spectral information we cannot distinguish between uniformly-shifted profiles and multicomponent profiles (which are often observed (see Fontenla et al., 1989) in this kind of event). Also, the limited resolution does not allow us to separate emissions originating in different spatial structures. However, from our data we give a measure of what kind of predominant motions were present in the event by using the previously mentioned calibration technique.

In Fig. 8 we show the velocity signal from the pixels corresponding to the bright point. It is apparent in this figure that substantial motions appeared related to the brightenings. The C IV line profile of the BP was dominated by red-shifted emission during both groups of brightenings, and the

wings of the line were enhanced at these times, particularly at the first brightening around 12:37 UT.

Figure 9 shows that velocity data from the filament locations behave in a more complicated manner. In the enhanced A area the brightenings were redshifted during the second group of spikes. This redshift reached maximum at about 13:03 UT and changed rapidly. However at the times corresponding to the first group of spikes, small, slowly-varying blue shifts were observed and also moderate to strong redshifts appeared at some pixels at times as early as 12:45 UT.

The behavior is very different in the E section of the filament where, in the easternmost portion, blue shifts appeared during the first group of spikes. This blue shift reached maximum around 12:45 UT at a pixel about 13,000 km away from the BP, but in the pixels closer to the BP, redshifts appeared during this first group of spikes. This suggests a pattern of C IV emitting material circulating toward the BP in opposition to the Hα material (see above).

The SW section of the filament showed a similar behavior during the first group of spikes; i.e., the parts closer to the BP showed redshifts and the parts at the extreme SW showed blue shifts. During the second group of spikes the redshifts dominated through most of this section of the filament, except at the midsection which showed moderate blue shifts.

This behavior of the velocity clearly shows that the process we studied is not just an upflow or downflow of the material, but rather it consists of a complex displacement of spatial structures and probably also flows of material within these structures.

5. Conclusions

We have observed the propagation of an energetic and dynamic disturbance along a filament within an active region. The filament ran approximately along an inversion line of the longitudinal magnetic field, but the field on both sides was relatively weak except at a point where a small flare or bright point occurred. This bright point developed at a point within the mid part of the filament where the gradient of the longitudinal magnetic field across the filament was very large. The Debrecen observations point out that the occurrence of such microflares is a frequent phenomenon in an active region and indicate that bright points are the signature of small explosive magnetic energy releases. Two disturbances seem to have originated at the SW end of the filament which merged with a facular area (see sketch in Fig. 10). These disturbances traveled to the N and E at speeds of 100-300 km s^{-1}, which we identify as consistent with the Alfvén speed. The perturbations of the filament consisted of sudden brightenings of spatial structures having maximum typical sizes between 7000 and 13,000 km. Complex velocity signatures were associated with these brightenings. To the east of the BP the filament bent toward the SE and the disturbance propagated up to its end, and an enhanced C IV area, not seen in Hα, was also disturbed. The disturbances in the E portion of the filament and in the enhanced C IV area seem to have had different characteristics, and the propagation velocity in the latter was somewhat larger.

The C IV brightenings of structures within the filament do not seem to reflect the horizontal propagation of energy through the filament, but rather, propagating disturbances seem to have triggered processes resulting in local release of stored energy that lead to brightening of the individual spatial structures which composed the filament. The spatial structures portrayed a

complicated pattern of interaction in which some were triggered and others were not, and where complex motions of the plasma occurred.

References

Beckers, J. M.: 1964, Thesis, Utrecht University

Démoulin, P., Einaudi, G.: 1989, in Proc. Mallorca Workshop on Dynamics and Structure of Solar Prominences (eds. J. L. Ballester and E. R. Priest), p. 93

Dezso, L., Gerlei, O., Kovacs, A.: 1988, Debrecen Photoheliographic Results, in Publ. Debrecen Obs. Heliographic Series No.1, 11

Fontenla, J. M., Poland, A. I. : 1989, Solar Phys. **123**, 143

Fontenla, J. M., Tandberg-Hanssen, E., Reichmann, E. J., Filipowski, S.: 1989, Astrophys. J. **346**, 435

Hermans, L., Martin, S. F.: 1986, in Coronal and Prominence Plasmas (ed. A. I. Poland), NASA CP-2442, p. 369

Hood, A. W., Priest, E. R.: 1980, Solar Phys. **66**, 113

Kuin, N. P., Martens, P.: 1986, in Coronal and Priminence Plasmas (ed. A. I. Poland), NASA CP-2442, 241

Kuijpers, J.: 1989, Proc. Chapman Conference on the Physics of Magnetic Flux Ropes, Bermuda, or in Plamsa in the Solar Atmosphere (eds. M. A. Dubois and D. Gresillon)

Martres, M. J., Soru-Escaut, I.: 1977, Solar Phys. **53**, 225

Mein, P.: 1977, Solar Phys. **54**, 45

Mouradian, Z., Soru-Escaut, I.: 199, Astron. Astrophys. **210**, 410

Mouradian, Z., Martres, M. J., Soru-Escaut, I.: 1981, Proc. Japan-France Seminar on Solar Phys. (eds. F. Moriyama and J. C. Henoux), p. 195

Poland, A. I., Mariska, J. T.: 1986, Solar Phys. **84**, 63

Porter, J. G., Tommre, J., Gebbie, K. B.: 1984, Astrophys. J. **283**, 879

Raadu, M. A., Schmieder, B., Mein, N., Gesztelyi, L.: 1988, Astron. Astrophys. **197**, 289

Raadu, M. A., Malherbe, J. M., Schmieder, B., Mein, P.: 1987, Solar Phys. **109**, 59

Rayrole, J.: 1981, Proc.Japan-France Seminar on Solar Physics (eds. F. Moriyama and J. C. Henoux) p. 258

Rompolt, B.: 1990, Hvar Meeting (eds. V. Ruzdjak and E. Tandberg-Hanssen) Publication of Hvar Observatory, 14, 1

Schmieder, B., Raadu, M. A., Malherbe, J. M.: 1985, Astron. Astrophys. **142**, 249

Schmieder, B.: 1989, in Dynamics and Structure of Quiescent Solar Prominences (ed. E. R. Priest), Kluwer Academic Publishers, 15

Schmieder, B.: 1990, in Lecture Notes in Physics (eds. V. Ruzdjak and E. Tandberg-Hanssen), **363**, 85

Schmieder, B., Poland, A. I., Thompson, W., Démoulin, P.: 1988, Astron. Astrophys. **197**, 281

Schmieder, B., Dere, K., Raadu, M. A., Démoulin, P.: 1989, Astron. Astrophys. **213**, 402

Schmieder, B., Van Driel Gesztelyi, L., Henoux, J. C., Simnett, G.: 1990, Astron. Astrophys., in press

Simon, G., Mein, N., Mein, P., Gesztelyi, L.: 1984, Solar Phys. **93**, 325

van Ballegooijen, A. A., Martens, P. C. H.: 1989, Astrophys. J. **343**, 971

Vrsnak, B., Ruzdjak, V., Brajsa, R., Dzubur, A.: 1988, Solar Phys. **118**, 45

Widing, K. C., Feldman, V., Bhatia, A. K.: 1986, Astrophys. J. **308**, 982

Woodgate, B. E. et al.: 1980, Solar Phys. **65**, 73

Figure Captions

- **Figure 1**: Debrecen observations (Hα quintets and white light) of two bright point events in the active region 2717 on Oct 9, 1980 at 07:48:27 (BE) and at 0812:31 (BP) before the UVSP oberving time. The letters NP in the white light image point out the two new appearing pores, signature of new emerging flux.
- **Figure 2**: MSDP observations, i.e., intensity and velocity map sequences, of a subflare or bright point (BP) and the subsequent partial DB of a filament on 9 October 1980. The field of view is 61 x 150 arc sec. In the intensity maps, white regions correspond to bright regions, in velocity maps they correspond to blue shifts. BE is a bright faculae. L points out a fine loop-like structure in the filament with persistent up (3 km s^{-1}) and down (-4 km s^{-1}) flows.
- **Figure 3**: Meudon Magnetogram obtained at 09:13:35 UT, field of view 276 x 338 arc sec. The dashed line indicates the position of the filament, BP the bright point.
- **Figure 4 a-b**: Intensity map sequence of C IV flare, (a) high intensity levels (b) saturated, for low intensity levels. A frame (1 x 1 arc min^2) was obtained every 31.4 s.
- **Figure 5**: The location of the bright point and the filament in the UVSP small raster field of view (1 x 1 arc sec^2).
- **Figure 6**: C IV composites; I(t) in various pixels corresponding to the bright point (BP).
- **Figure 7**: C IV composites; I(t) in filament pixels, (a) in the E section (No-

tice the presence of two successive maxima), (b) in the SW section referring to the Fig.5.

- **Figure 8:** C IV composites; V(t) in the bright point (BP).
- **Figure 9:** C IV composites; V(t) in filament pixels corresponding to the pixels in Fig. 7, (a) in the E section, (b) in the SW section.
- **Figure 10:** Sketch of the active region. The distubance propagates along the filament (double arrows). The straight line indicates the Hα filament location, the hatched lines correspond to C IV plages, the letters BP indicate the position of a bright point visible in Hα and C IV lines, BE a bright point visible in Hα , L a Hα loop.

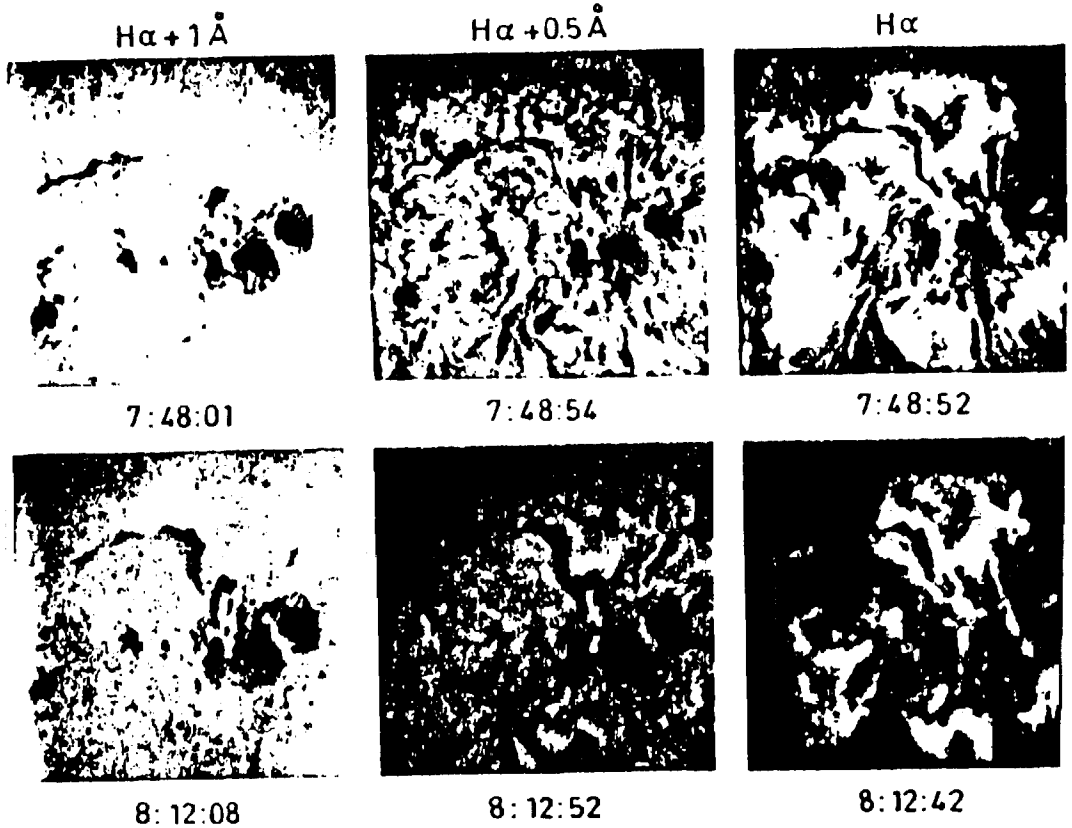

Fig. 1a

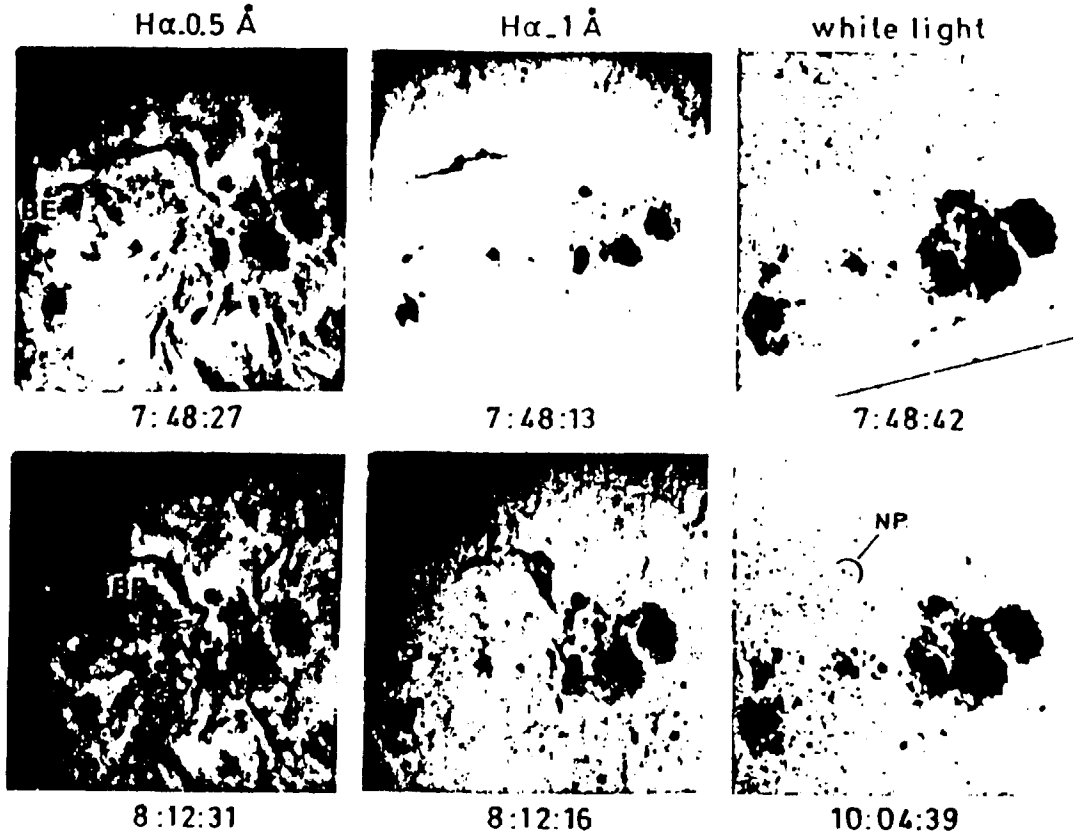
Hα.0.5 Å
Hα_1 Å
white light
BF
7:48:27
7:48:13
7:48:42
BP
NP
8:12:31
8:12:16
10:04:39

Fig. 1b

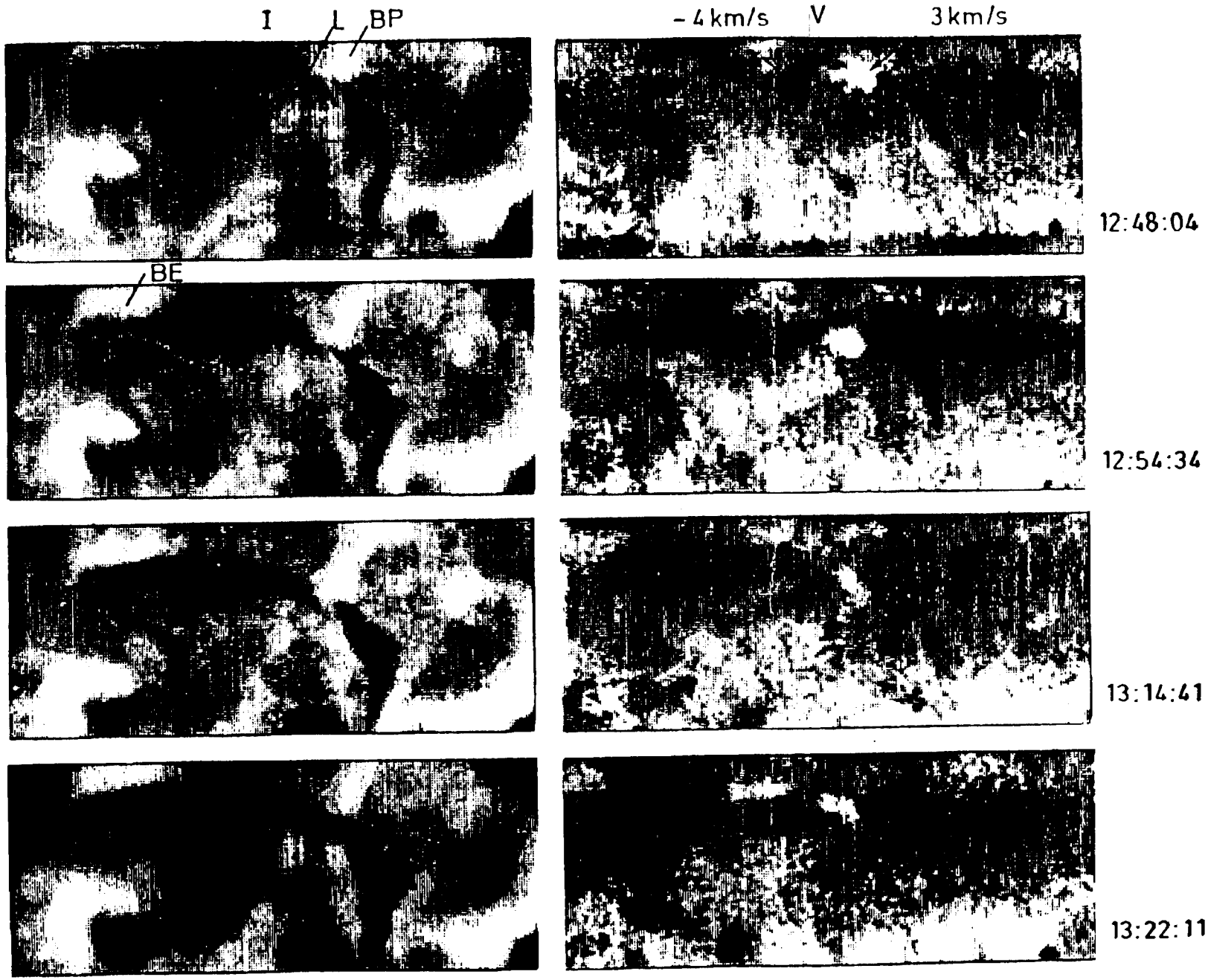

Fig. 2

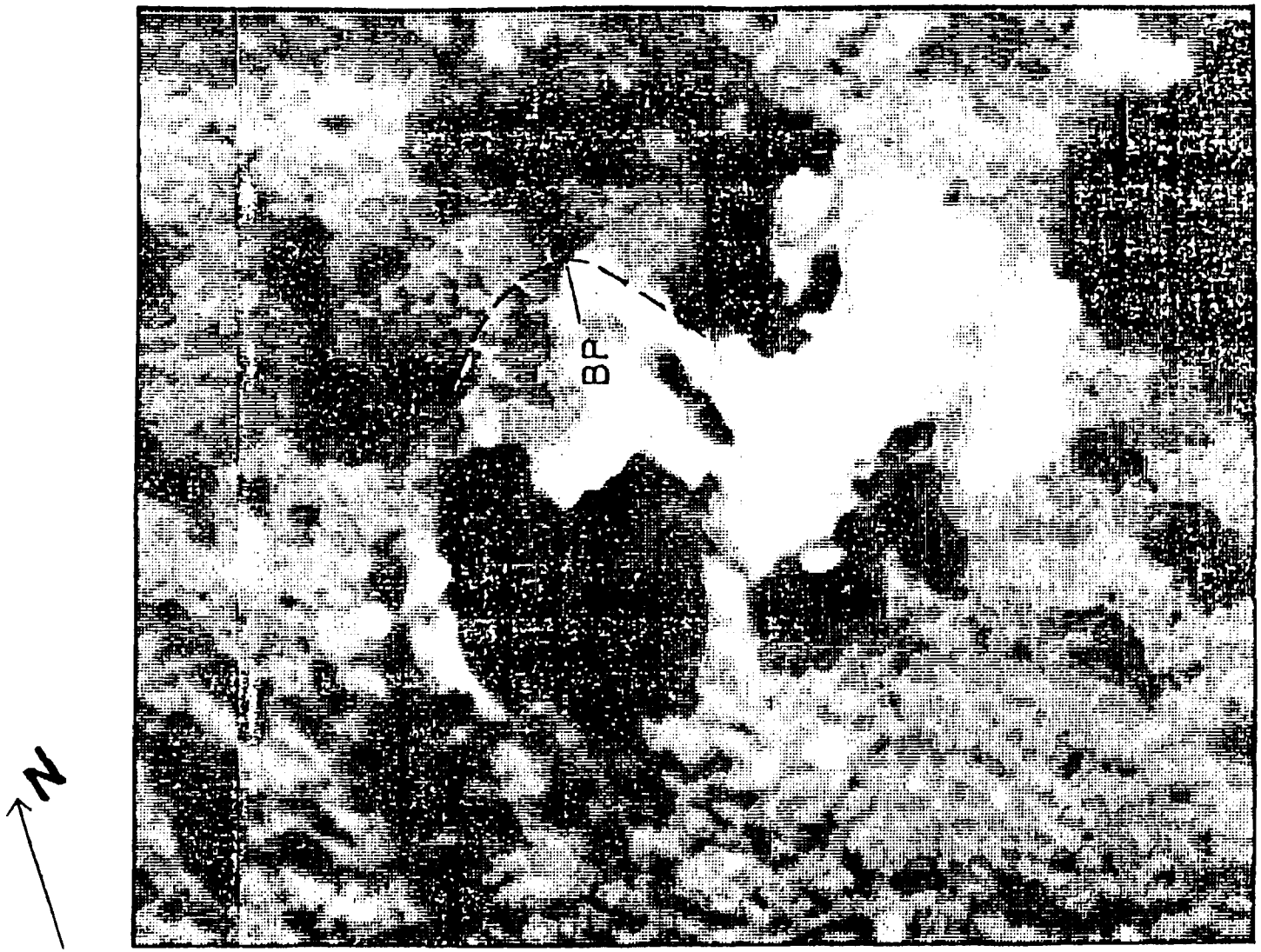

Fig. 3

Fig. 4

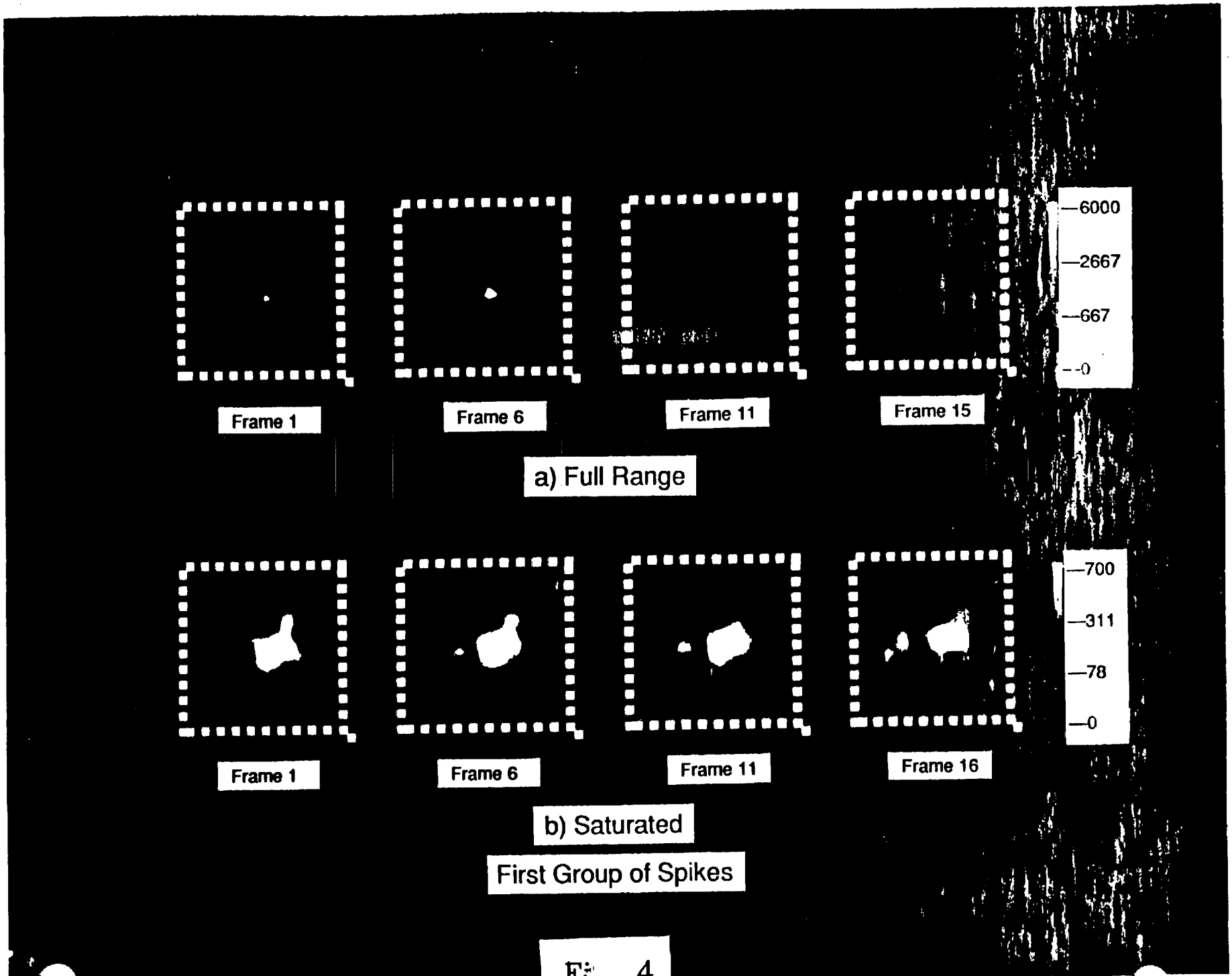
Frame 1
Frame 6
Frame 11
Frame 15
6000
2667
667
0
a) Full Range
Frame 1
Frame 6
Frame 11
Frame 16
700
311
78
0
b) Saturated
First Group of Spikes

Fi 4

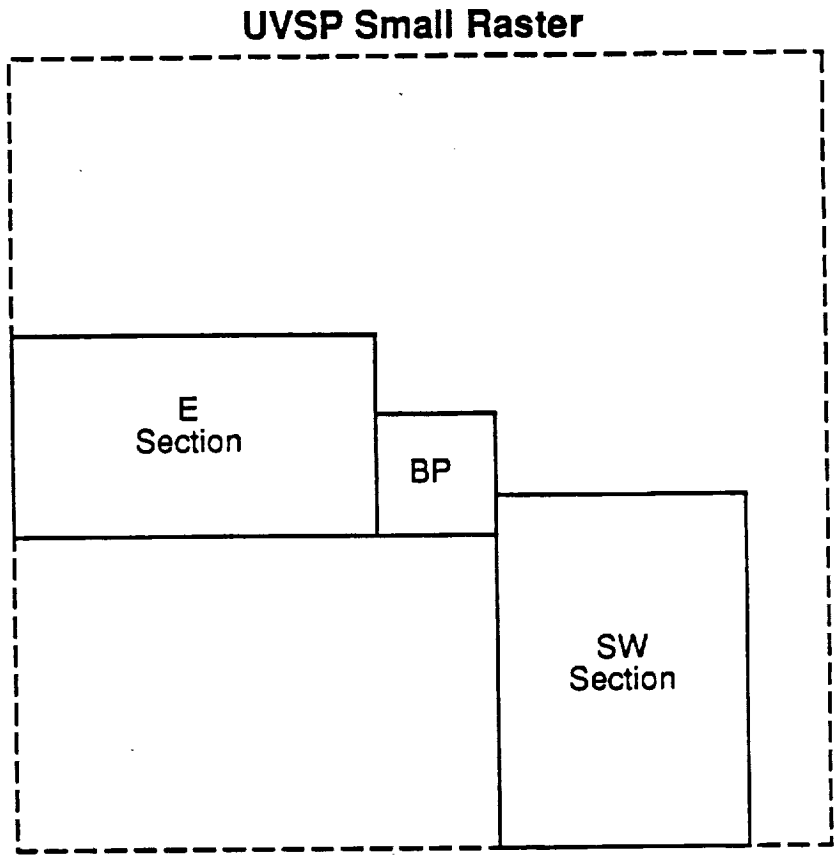

Figure 5

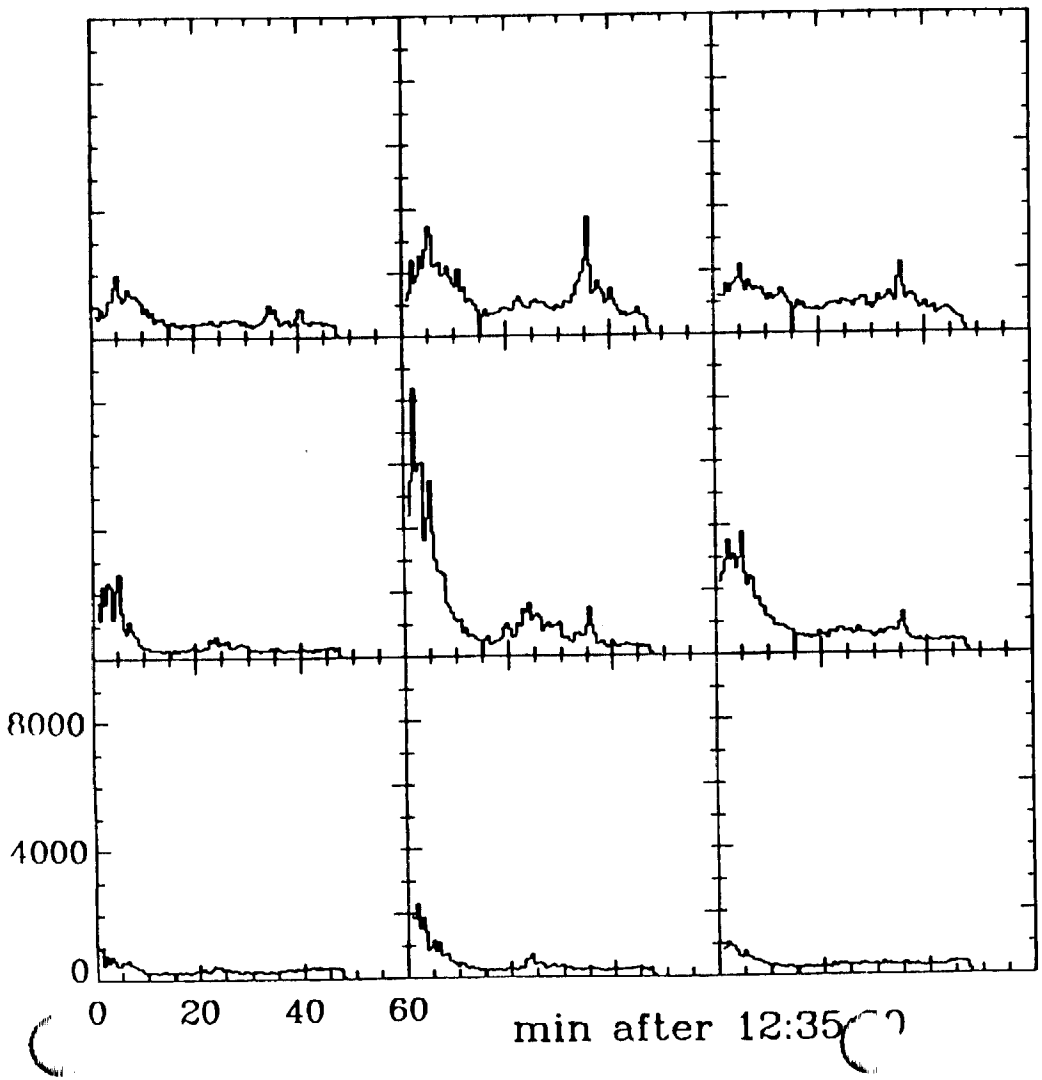

Fig. 6

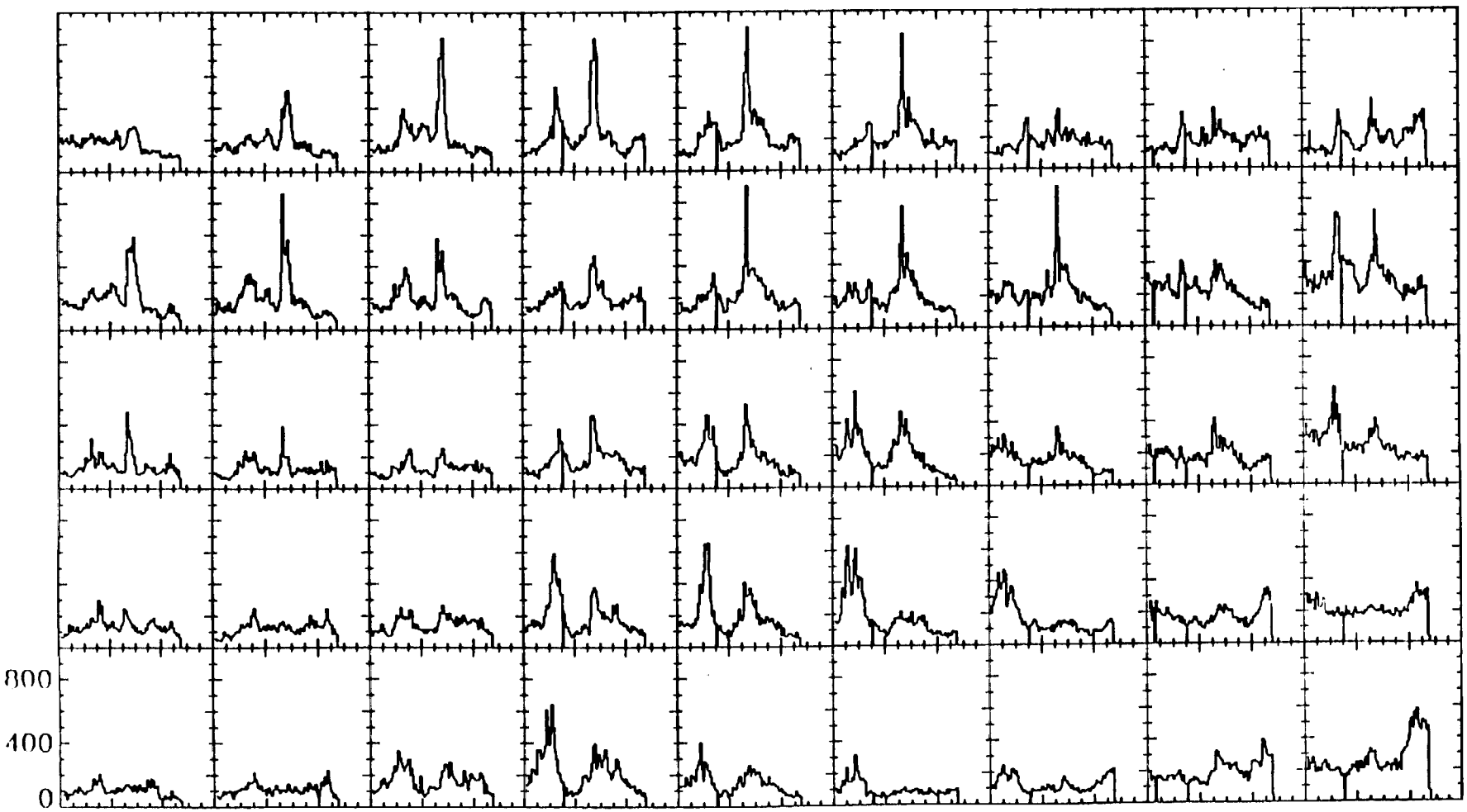

Fig. 7a

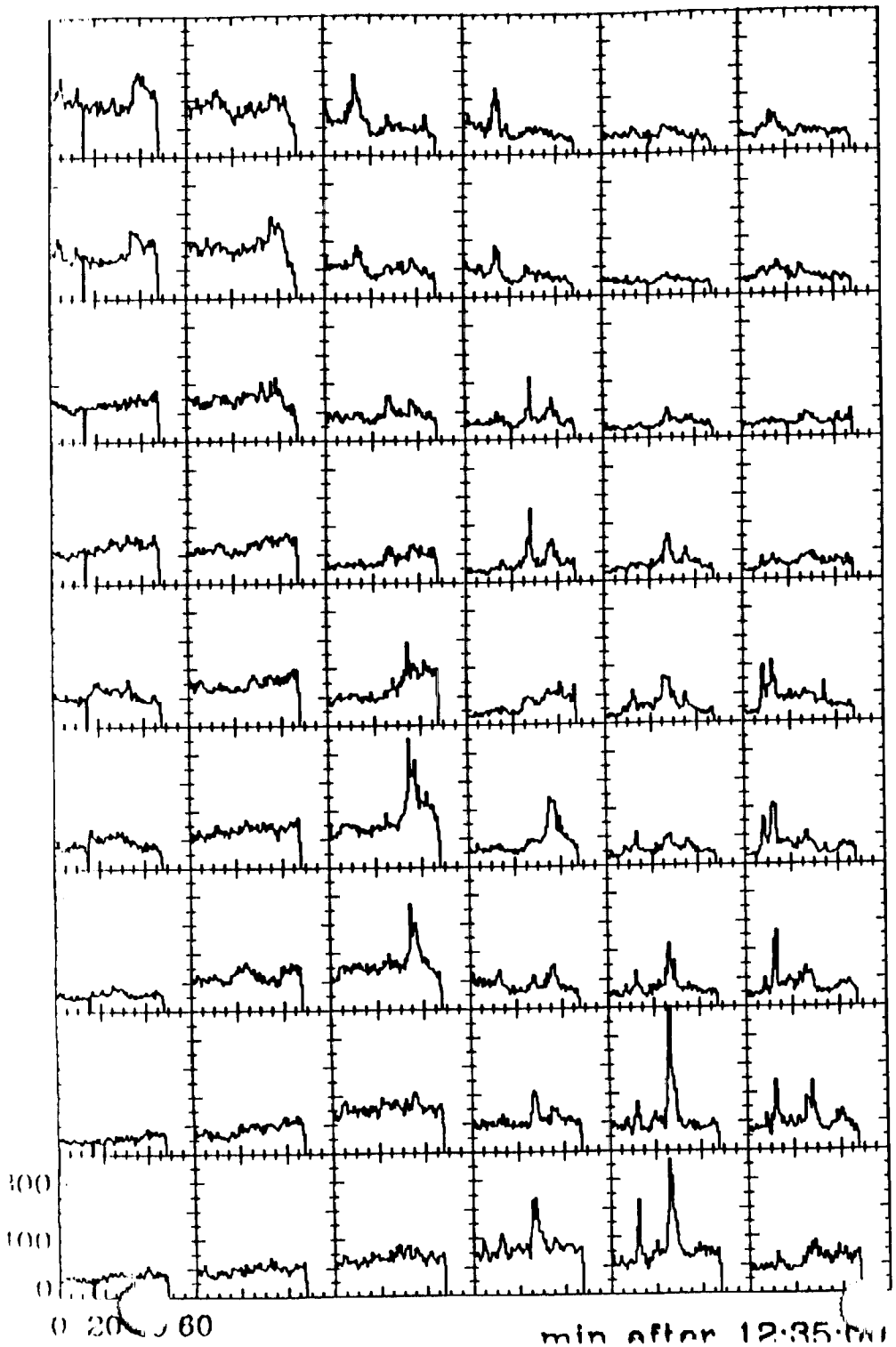

Fig. 7b

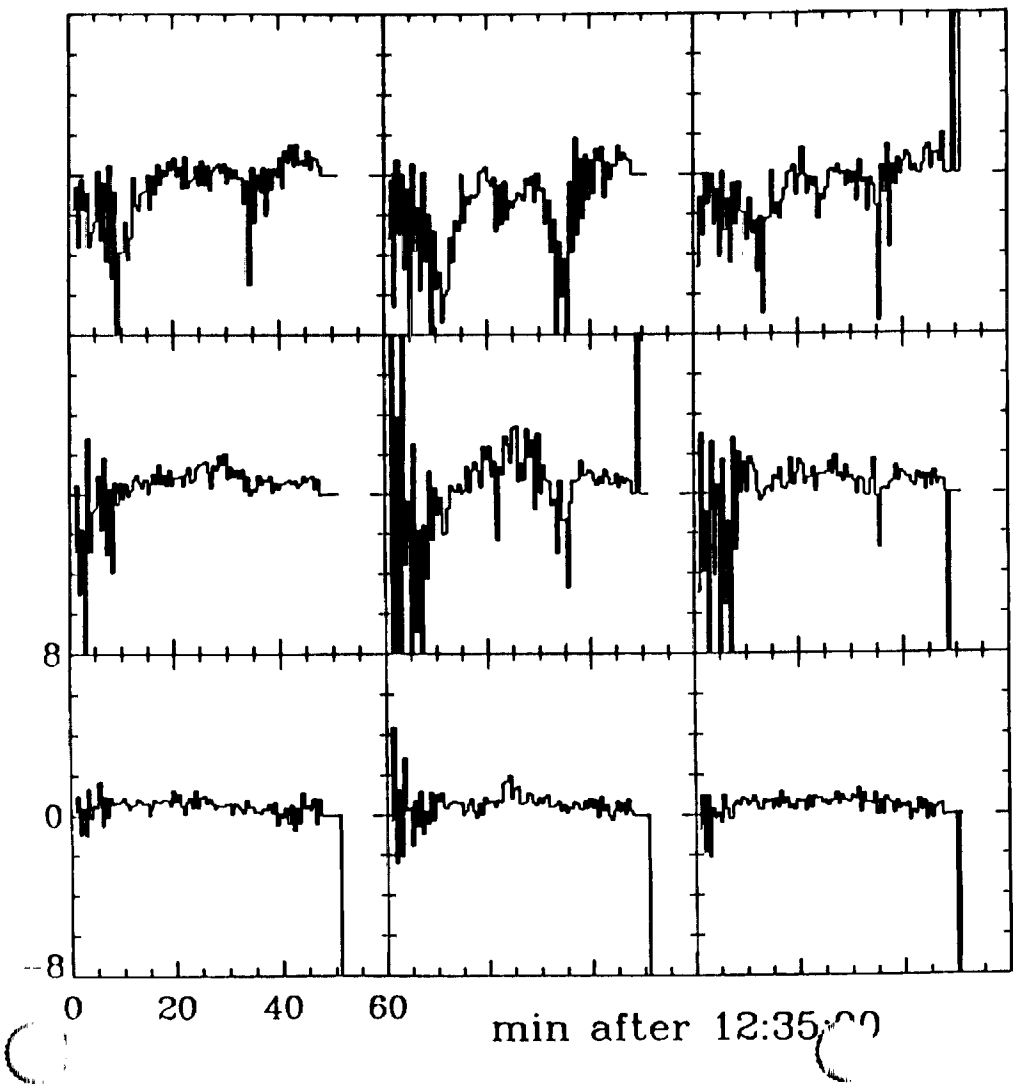

Fig. 8

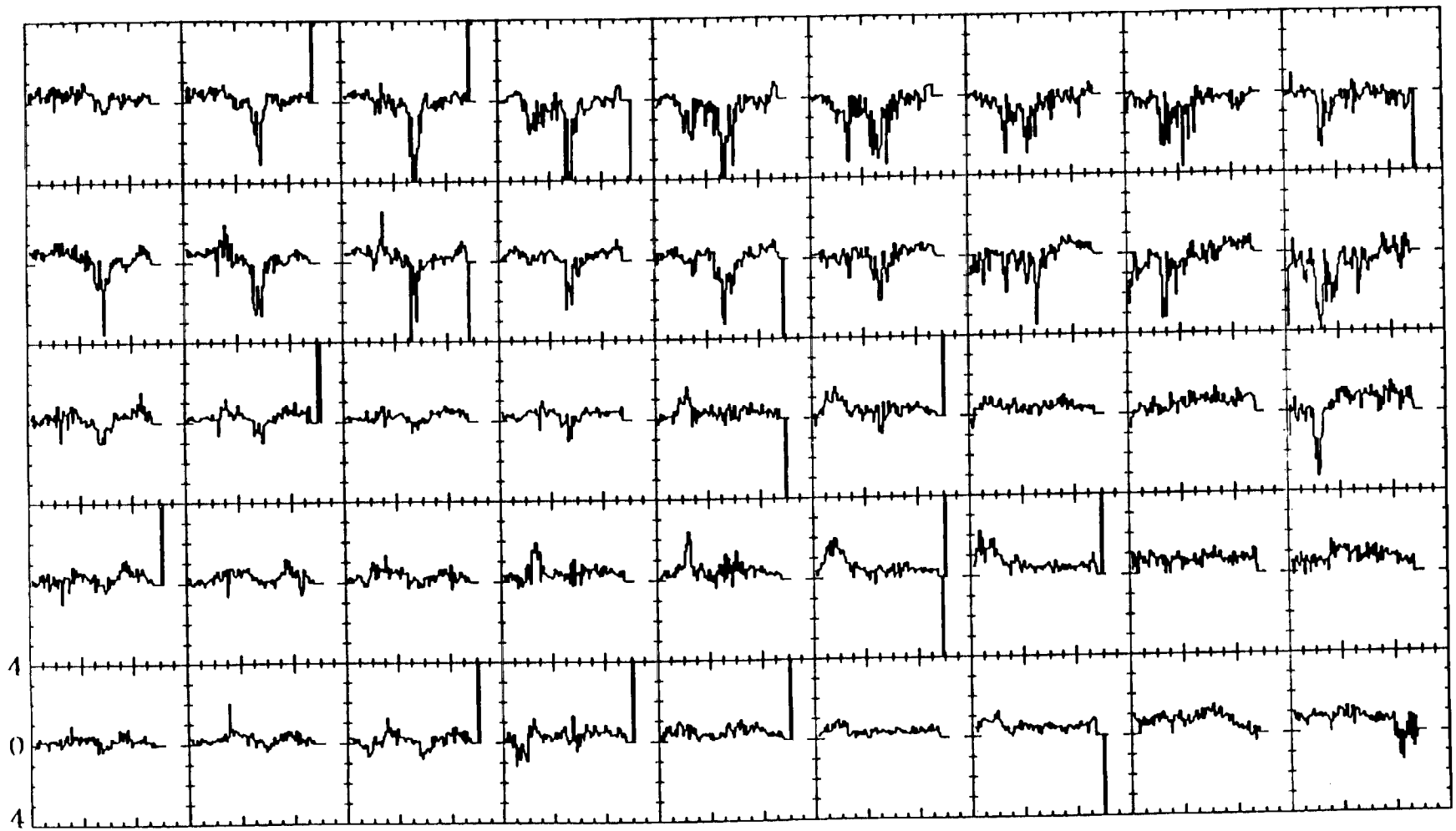

Fig. 9a

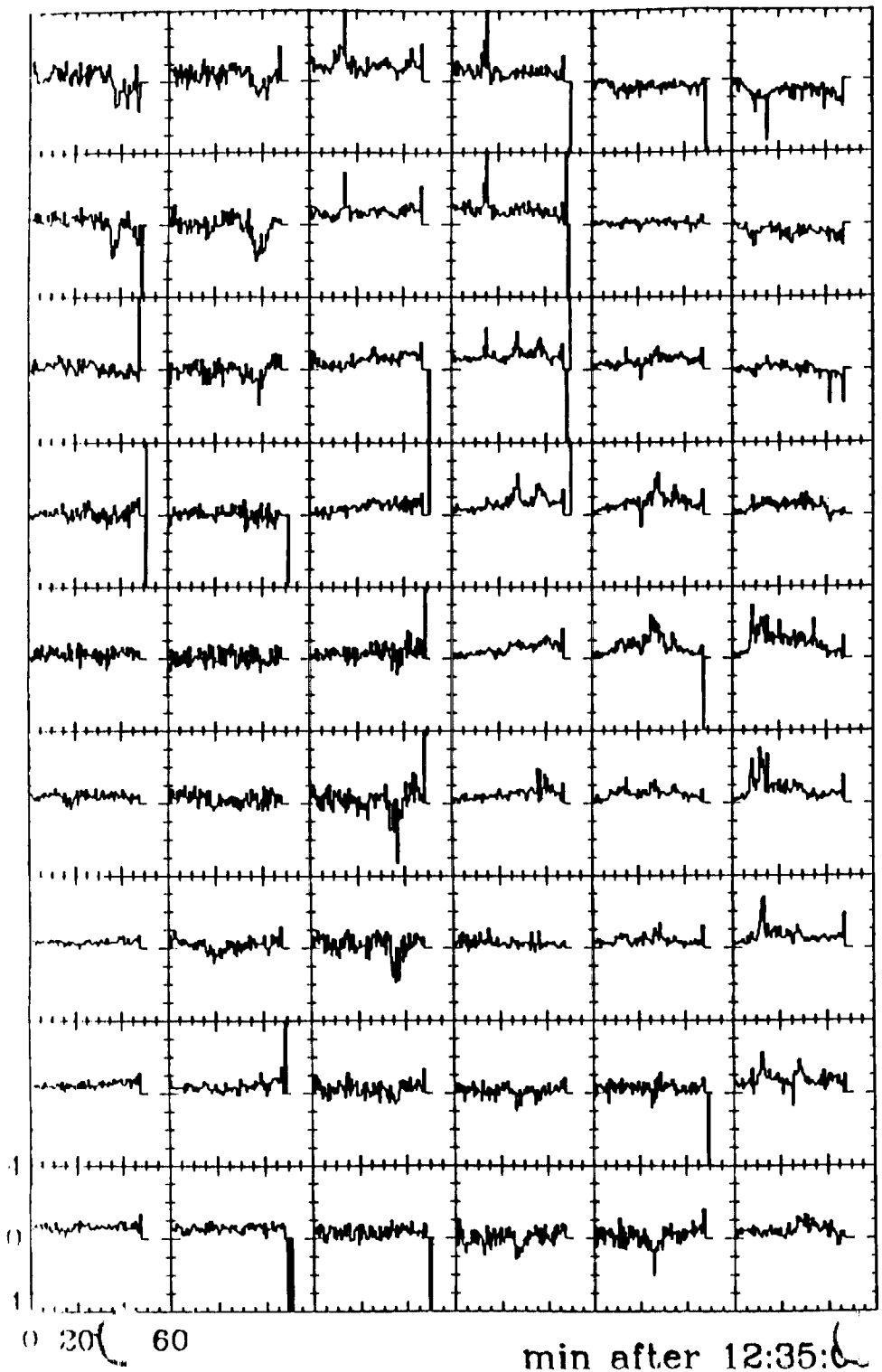

Fig. 9b

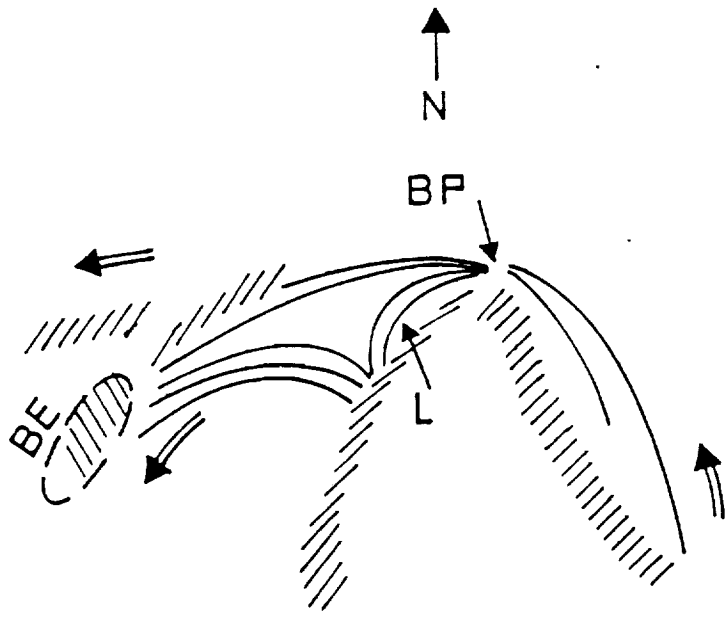

Fig. 10

FLARING ARCHES

III. The subflare of June 27, 1980, and its related extended arch

Juan M. Fontenla*,

The University of Alabama in Huntsville, U.S.A.

Zdenek Svestka

Laboratory for Space Research Utrecht, SRON, The Netherlands

Frantisek Farnik

Astronomical Institute of the Czechoslovak Academy of Sciences, Ondrejov, Czechoslovakia

and

Frances Y. Tang

Solar Astronomy, CALTECH, Pasadena, CA 91125, U.S.A.

received: July 17, 1990

To appear in Solar Phys.

* Member of Carrera del Investigador, CONICET, Argentina.

Abstract.

We show detailed observations in X-rays, UV lines, and Hα of an extended arch, about 300,000 km long, which developed as a consequence of a compact subflare. This subflare occurred in an "included" magnetic polarity of relatively low magnetic field strength (compared to that of the sunspots). The apparition of this big arch was preceeded by that of a smaller arch, about 30,000 km long, which masked the polarity inversion line filament in the early phase of the subflare. The big arch which developed later, around the time of the main X-ray and UV main spike of the subflare, connected the included polarity and the main leading sunspot of the region, and became fully developed in a few minutes. The fact that both arches were simultaneously observed in all spectral domains as well as their fine structure in Hα can only be explained by considering the arch as composed of several unresolved portions of material having widely different temperatures. The Hα observations can be interpreted as showing the appearance of this cool material as a result of condensation, but a more appealing interpretation is that there was almost simultaneous ejection of superhot (10^7K), hot (10^6 K), mild (10^5 K) and cool (10^4 K) material from the subflare site along previously existing magnetic tubes of much lower density. The termination of the subflare was marked by a rather hard X-ray and UV spike which appeared to originate in a different structure than that of the main spike. The material in the arch gradually cooled and drained down after the end of the subflare.

1. Introduction

In the present paper we report observations of an extended arch structure which developed as a consequence of a compact subflare observed in Hα, UV lines, and X-rays. These combined observations display some intriguing aspects of the development of the extended arch and the sequence of emissions in different wavelength domains. Particularly, the sequence of emissions does not support the simple picture of sudden coronal heating,

evaporation and condensation for the material in the arch. But, it rather suggests that a mixture of material at widely different temperatures is injected into the extended arch from the compact subflare which takes place due to magnetic field reconnection close to the primary footpoint of the arch.

It is well known that various particular features are observed in the low corona as a consequence of solar flares. These features can be observed in different spectral domains and must be interpreted in the context of the flare dynamics. The most common structure observed in the low corona in relation to flares are the post-flare loops. These are observed in Hα during the decay phases of two-ribbon flares. Post-flare loops are usually interpreted as the cooling remnants of newly reconnected magnetic arches filled with material. The hot material is considered to be originated by evaporation of chromospheric layers. During the late stages of the flare the material condenses (then becoming visible in Hα) and falls under gravitational forces. In post-flare loops, both of the loop footpoints are anchored in the chromospheric flare ribbons. Another feature related with eruptive flares is the perturbation of the polarity inversion line filament. This filament is seen before the flare as an Hα absorption feature overlying the magnetic neutral line. The filament is often perturbed prior to the flare and undergoes eruption or sudden disappearance. Active region filaments are rooted close to the polarity inversion line and are formed in regions of magnetic shear (Hirayama, 1985).

The "flaring arch" is a different type of flare feature (Svestka and Martin, 1988, Paper I). The primary footpoint is located within a chromospheric flare or subflare and the remote secondary footpoint is basically passive. Energy seems to be released at the primary footpoint and its effects propagate along the arch toward the secondary footpoint which responds to such input. A scenario for these arches suggests the propagation of electron beams, thermal fronts, and shock waves toward the secondary footpoint (Svestka et al., 1989, Paper II)

The present paper deals with a flaring arch which has a similitude to the events described in Papers I and II, but shows some differences regarding the secondary footpoint response and probably also the way the energy propagates along the arch. Here we present simultaneous X-ray, UV, and Hα data with good temporal resolution which allows us to examine the timing between the different emissions along the arch. The arch originated in a confined or compact subflare (of dimensions $\sim 10^4$ km), and was far bigger (with length $\sim 10^5$ km) than the subflare. The observations allow us to obtain a picture of the arch consisting of numerous narrow threads which in the early stages evolved rapidly in time. After some time, the arch as a whole was formed containing material within the full observed range of temperatures. We will also show that phases of very fast development of the arch, in Hα, UV and X-rays, seem to be related to phases of sudden energizing of the compact subflare. The Hα and soft X-ray emissions of the subflare were relatively weak compared to other flares, but, as usual at flaring arches (cf. Paper I), the event displayed rather hard emission detected in the range 27.4-54.8 keV. We will also show that there was a clear indication of the termination of the strong energy release process responsible for the subflare. The end of the energy release marked the beginning of the relaxation phase in which the arch dissipated from the top.

2. The Active Region

The event we consider occurred in the active region AR2522 (NOAA, Boulder) on June 27, 1980, between about 23:05 and 23:45 UT. At this time the active region was located close to the west limb of the Sun at about latitude south 30°. The angle between the local radius and the line of sight was about 65°. This projection angle corresponds to a projection factor of 1/2.4 between the distances along the solar surface and those measured in the plane of the sky (perpendicular to the limb).

The magnetic structure of this active region appeared relatively simple. There was some change between the appearance of the region at the east limb and June 22, but after

it remained practically unchanged during the remainder of its transit. Figure 1 shows the magnetic structure of the region on June 23 (when the active region was close to the central meridian). The magnetograms from Kitt Peak Observatory and from Marshall Space Flight Center on June 27 (at 18:26 and 19:00 UT respectively) displayed no basic changes in the magnetic structure of the region. However, these magnetograms were affected by the usual distortions due to the large projection effects because of the proximity to the limb. For this reason we consider Figure 1 as more descriptive of the magnetic configuration of the active region, even though it is not simultaneous with our event.

The magnetic structure is shown in Figure 1. It consisted of a large leading sunspot (negative polarity) located well inside an extended similar polarity area, and at a considerable distance to the east ($\sim$ 140000 km), appeared the trailing sunspot group with several small sunspots. The main polarity inversion line was close to the trailing polarity sunspot group (at about 20000 km west) and far from the main sunspot. The Kitt Peak data and the MSFC data show that some relatively compact area of positive polarity was located within the large negative polarity area. This "included" polarity area was observed at about 90000 km east of the main sunspot on June 23 and corresponds to the subflare site. The evolution in the previous days indicates that it was the included polarity was a remnant of positive polarity field after most of the area evolved from positive to negative polarity. This corresponds to the emergence of a new group of secondary leading polarity sunspots to the west of the included polarity, and to the migration of the trailing sunspot group from the southeast toward the east of the main sunspot.

Panel a in Figure 2 shows the location of the leading polarity sunspots shortly after our event in offband Hα on June 28 at 00:02 UT. The approximate location of the subflare site (coincident with the arch primary footpoint) is marked as B in the figure. Panel b in the figure shows the active region before the subflare as seen in the Hα line center. D indicates the polarity inversion line filament which encircles the included polarity. Panel c in this figure shows the start of the subflare at 23:18:16 UT. The location of a different

and fainter subflare is indicated by L, note that this event does not seem related with the events we study.

3. The Observations

The data studied is from joint observations performed by the HXIS and UVSP instruments on board Solar Maximum Mission satellite. The HXIS instrument has been described by Van Beek et al. (1980), and the UVSP instrument by Woodgate et al. (1980). Complementary observations by the HXRBS instrument are also used to characterize the hardest phase of the subflare.

During our event the UVSP instrument used a combination of slits which provides 10×10 arc sec pixels. Rasters were taken using three detectors corresponding to the Fe XII (1349Å), Fe XXI (1354Å), and O V (1371Å) lines.

However, we must warn the reader about the data corresponding to Fe XXI; it is severely contaminated by other line and continuum emission because of the wide spectral range (3 Å) covered by the slit used. Other lines present in this range include some from O I and C I, but other instrument data (e.g. Cohen, 1981) shows that the Fe XXI line, although practically absent in the quiet Sun and active region spectra, shows very large intensities in the flare spectra reaching integrated intensities much larger than those of the low temperature lines and even greater than the already enhanced O V line. Consequently, the low-level intensities observed in some pixels are probably due to the cooler lines and the continuum, but certainly the large intensities observed at the subflare site and at least part of the enhancement along the arch are displaying the Fe XXI line emission. This Fe XXI emission indicates substantial amount of material with $T_e \sim 10^7$ K.

In the other UV lines the spectral width covered was much narrower (0.3 Å for Fe XII and 0.5 Å for O V) and no other lines seem to be able to contaminate the observations. The Fe XII line is very weak in the quiet Sun but is prominent in active regions (and of

course in flares). This line corresponds to temperatures of $\sim 10^6$ K. The OV line is a typical transition region line corresponding to $\sim 10^5$ K.

The UVSP detectors arrangement, then, is well suited to display material over a wide range of temperatures. The Hα data permits to extend the temperature coverage to even lower temperatures of about 10^4 K, and the HXIS data gives more clear (uncontaminated) information corresponding to temperatures of about 10^7 K and above (if thermal emission is assumed).

The UVSP data on our event includes two sets of observations. The first set consists of a sequence of 9 rasters covering a 240 × 240 arc sec field of view (the last raster of this sequence was interrupted and is incomplete). The time evolution during this first data set was not well observed because of the relatively long time ($\simeq$ 82 s) consumed by the rastering. The second data set consists in a sequence of 60 smaller field-of-view (120 × 120 arc sec) rasters. This data allows for more detailed study of time evolution since these rasters were taken about every 21 s. However, we remind the reader of the non-simultaneity of the different pixels sampling. The secondary footpoint of the arch was just out or at the edge of the field of view of the second data set, but inside the field of view of the big rasters. Due to the low spatial resolution of the UVSP instrument under this operating mode, the counts levels were high and low noise level was achieved.

The HXIS data includes good temporal data from both the fine field of view (FOV) with 8 × 8 arc sec pixels and the coarse FOV with 32 × 32 arc sec pixels. Because of the large extension of the arch we study, the secondary footpoint of the arch lies just at the edge of the fine FOV. The lack of complete coverage of the secondary footpoint in the fine FOV does not have major effect in our study.

The Hα data was obtained at Big Bear Solar Observatory and consists of good quality line-center filtergrams covering a 180 × 240 arc sec field of view with pictures every 5 to 20 s.

4. Generalities of the Event

We center our study on the big arch related to a small and short-lived Hα subflare. Our study considers the relationship between the evolution of this extended arch and its parent compact subflare. The subflare was reported by the Big Bear Observatory classified as SN, and it was accompanied by an eruptive event. However, as the data shows, this eruptive event does not seem to correspond to a detectable eruption of the magnetic field. The shape of the large arch observed at the end of the event (see below) shows that it straddles over the polarity inversion line (PIL) at a large angle with one of its footpoints very far from the PIL. Thus the eruption we are studying is basically different from those which involve the activation of highly stressed previously quiescent filaments rooted close to the PIL which erupt into the interplanetary medium. Rather than an eruption of the magnetic field, the present eruptive event seems to be an ejection of material along preexisting field lines, and the material does not disrupt into the higher corona but returns to the chromosphere. Thus it resembles more a bright surge than an erupting filament.

Tables I and II give the chronology of the observed events for later reference.

A coincident impulsive X-ray event was recorded by GOES starting at 23:22 UT, reaching the peak at 23:26 UT and ending at 23:38 UT; the event has been classified as C2 and appeared in both, the 1-8 Å and the 0.5-4 Å bands. It seemed to be composed of two spikes (the first of larger intensity). This event was the same as observed by HXIS and we mention the GOES data in order to give a reference for the size of the present event with respect to other X-ray bursts.

A "gradual rise and fall" radio burst was observed at this time by the Toyokawa Observatory at 3.75 GHz. The event started at 23:10 UT, peaked at 23:26 UT and ended at 24:10 UT; its peak intensity reached 3×10^{-22} W m^{-2} Hz^{-1} with a mean of about one half of this value.

Schematically, the event began with a small compact flare around the northern part of the PIL which encircles the included positive polarity mentioned before. This PIL segment is marked by a chain of dark Hα filaments (see Figure 2b) which during the flare seems to be hidden by overlying emission at times, but then reappears after the fading of the overlying emission. The bright area to the north of the filament is narrow (not wider than 3 or 4 arc sec, i.e. ~6000 km on the solar surface), and the brightening to the south of the filament is more extended and seems to cover the whole included polarity (again about 10" in projected diameter, corresponding to about 20000 km on the solar surface). We want to stress that because of the compactness of the subflare and the low spatial resolution of both the X-ray and the UV data, we cannot study the subflare in great detail.

After the subflare started, a small arch develops initially and later a big arch extends reaching about 100000 km height. Figure 3 depicts the basic structure of both arches, and shows that the early development of the big arch is somewhat confused by the previously existing small arch. This pattern of two interacting arches has been found in the X-ray observations of many flares by Machado et al. (1988a) and Machado et al. (1988b).

The general characteristics of the big arch can be studied with more certainty after it extends beyond the height of the small arch. It is clear in the Hα data that this is not a homogeneous loop, but a conglomerate of threads which appear rooted in several different locations (primary footpoints) within the flare site and seem to converge to a more compact secondary footpoint in or very close to the big spot penumbra. The developed arch extends over about 70" projected distance to the west (corresponding to about 120000 km distance between footpoints). The cross section of the arch seems to decrease as it approaches the big spot (and thus probably higher magnetic fields). Of course, we are unable to estimate any variation in the cross sections of individual loops.

5. The Early Phase of the Subflare and the Small Arch

The start of the sequence of events was marked by the brightening in Hα of the flaring area at the northern boundary of the included polarity. Then, an elongation develops to the southwest forming what we call the "small arch". This small arch has the appearance of having both of its footpoints very close to the PIL, and thus is very different from the large arch which developed later (see Figure 3).

The precise start time of the subflare is difficult to determine without an accurate photometry, but we give in Table I the approximate time of 23:10:20 UT for the first Hα showing a clear brightening. As it was said before, both sides of the PIL filament start brightening simultaneously, but the north side is confined to a narrow strip while the southern is more diffuse and extended.

We show in Figure 2c the development in the Hα line at 23:22:22 UT. Note that the PIL filament became practically masked and that the flare practically reached its maximum area at this time. After this time the area of the flare did not increase substantially but remained almost constant until the flare brightening disappeared. We believe the masking of the PIL filament was due to the appearance of Hα-emitting loops overlying the filament. This possibility is also supported by the fact that after the subflare the filament reappeared basically unchanged. Accordingly, we believe that some low-lying emitting loops began to appear as early as 23:20:41 UT. But, at this time the height was such that given the observation angle the loops appear projected over the subflare site. At later times, the height of this loop system increased until it developed in the "small arch" previously described, which projected in the plane of the sky, extended away from the flare site (keep in mind the subflare is close to the limb).

Figure 4 shows the relative positions of the HXIS FOV (a) and the UVSP small rasters (b), with respect to the Hα observations.

An early intensity increase at the subflare site was observed practically at the beginning of the UV observations (23:13:27 UT) in Fe XXI and O V. However, its slope was

very shallow and uncertain until 23:17:09 UT when a substantial increase of slope was observed in both lines. The first clear indication of increasing intensity appeared in Fe XII at 23:19:53 UT. The apparent delay in the start of the subflare in this line was probably just due to the lower contrast of the subflare respect to the background in this line. This contrast can be measured by the ratio, between the background intensity and the peak measured intensity, which is about 22 for Fe XXI, 5.2 for Fe XII, and 16 for O V.

The start of the subflare in X-rays can be traced to 23:20:40 UT in the lowest energy band, and it is somewhat delayed in the upper energy bands (as in most flares). We believe that this delay was only apparent and due to lower counts at higher energies which permit the detection of an increasing intensity only after it has reached a relatively high threshold. The intensity increase had a steady small slope in the present early phase of the subflare.

A striking observation was the fast UV brightening of the pixel which would correspond to the secondary footpoint of the big arch, between 23:16:49 and 23:25:27 UT (during the sequence of big rasters). Though this brightening was best observed in the OV data, it was also seen in Fe XXI and even in Fe XII. Because of the lack of spatial resolution we cannot ascertain whether this brightening corresponded exactly to the secondary footpoint or not, but it rather seems to be related to the Hα brightening of the loops marked "L" in Figure 2c at around 23:17 UT. The Hα data shows that this feature did not seem to be closely related to the event we study. At this time, no intensity increase above the instrument sensitivity threshold was observed in HXIS fine FOV close to the secondary footpoint.

Thus, when comparing the big arch with those studied in papers I and II, we find that no secondary footpoint brightening can be seen, in any wavelength, associated with our event. This behavior can be perhaps explained by the apparent convergence of the magnetic field lines at the secondary footpoint. If, as was suggested in Paper I, the Hα brightening is due to accelerated electrons impinging in chromospheric layers, the convergence of the

magnetic field lines should mirror back the bulk of the accelerated particles and prevent them from reaching the high density layers.

After 23:20:41 UT the Hα brightening of the northern part of the PIL extended to the west, and some faint emission appeared in the small arch. At 23:23:11 UT a bright elongation developed very fast towards the southwest filling the small arch. The rate of elongation was about 400 km s^{-1} between 23:23:41 and 23:23:47 UT. This would correspond to a vertical elongation velocity of about 500 km s^{-1}. However, this value of elongation velocity may not correspond to mass velocity. An alternative interpretation is that material is injected into the loops which compose the arch at high temperature (invisible in Hα), and condensates faster in the lower lying loops. The progression of the Hα emission toward large altitudes would, then, correspond to the progression in the cooling of the loops, and this would give an apparent motion. Figure 5 show some frames during this evolution. The small arch was fully developed by 23:23:47 UT, and remained with no important changes for about 1 minute until the start of the next dynamic phase.

The UV lines of O V, Fe XII and Fe XXI display a remarkable sudden increase in the slope of the brightening at about 23:22:36 UT in the pixels corresponding to the subflare site. At 23:22:29 UT the emission in OV started to increase and the Fe XXI emission rose in the pixel corresponding to the top of the small arch (the pixel center was about 15 arc sec to the southwest from the subflare pixels.) This indicates that the UV emission from the small arch did not follow, but slightly preceded, the Hα emission; unfortunately, the lack of a photometric analysis of the Hα images and the low time resolution of the UV prevent us from assessing the time differences accurately. The UV observations in the pixel closer to the subflare site showed a mixed behavior since it probably included both the small arch and a part of the subflare. The remaining pixels showed no evidence of emission associated to the subflare during this early stage.

Clear evidence of X-ray emission at the pixel corresponding to the small arch top was observed at about 23:21:30 UT. We stress that the start times we give here are not very accurate because they depend on sensitivity threshold, noise and background brightness; we give these times only for reference and they should be considered as upper limits to the onset times. In Figure 6 panels a,b, and c we show plots of counts versus time for the pixels corresponding to the subflare site and the small arch, and these plots illustrate the difficulty in determining absolute times from the data. The plots are for the three lowest HXIS energy bands (3.5-5.5 keV, 5.5-8.0 keV, and 8.0-11.5 keV) in which our event was detected.

The small arch had a projected size of 18000 km in Hα. This size is also consistent with the UV and X-rays, and since we only see the feature in projection we cannot give its absolute dimensions and a unique interpretation. However, we can give a possible interpretation as follows. This extension of the subflare may be a complicated fine-structured small arch system which was rooted on both sides of the PIL (see Figure 3). The arch was composed by threads at different temperatures ranging from 10^4 to at least 10^7 K. If the arch system was vertical, its height should have been about 28000 km. This arch system is similar to a system of post-flare loops whose footpoints are located on each side of the PIL which encircles the included polarity. The timing between the different emissions may correspond to a fast cooling (in less than about 1 minute) of hot ablated material. This cooling time can be easily achieved by combined conductive cooling at high temperatures ($\sim 10^7$ K) and optically thin radiative cooling at the intermediate temperatures ($\sim 10^6 - 10^5$ K) if the density is $n_e \sim 10^{10}$ cm^{-3}. But a similar cooling time can also be achieved by purely radiative cooling if the density is $n_e \sim 10^{12}$ cm^{-3}. The fact that the Hα appeared in emission indicates that high densities ($n_e \sim 10^{12}$ cm^{-3}) are indeed present during the cool phase of this small arch (see Svestka et al. 1987). It is not clear, however, whether the density can reach such high values during the hot phase, because such values would imply a large gas pressure ($\sim 10^3$ dyn cm^{-2}). Moreover, the presence of such high

density at the intermediate temperatures ($\sim 10^5$ K) poses the problem of an extremely short cooling time ($\sim 10^{-2}$ s). In order to explain the observations in the case of high densities (very short cooling time), the temperature of the warm plasma must be sustained by sustained heating. Or, if one assumes that the density is low, delayed injection into the arch of the cool dense material is required.

After the Hα material has appeared at the top of the small arch, an early relaxation phase occurred for several seconds, in which dark streaks originate at the top and propagate downward. This behavior can be explained by the progressive falling down of the material, which turns from the initial Hα emission into absorption as the density decreases.

6. The Main Phase of the Subflare

We describe in some detail the main spike of the subflare because it marks the beginning of the development of the big arch and hence it is apparently related to the origin of the arch material.

The largest sudden increase in the X-ray emission at the subflare occurred at 23:25:10 UT (see Figure 6). This emission was mainly concentrated in two FOV pixels which correspond to the northern part of the included polarity, but some emission was also observed in the two pixels to the south, and small emissions are observed in surrounding pixels and in the arch pixels (see below). This behavior was different from the earlier slow brightening in which the pixels to the south had comparable intensity, and hence it reveals that different spatial structures were responsible for the initial slow and the fast main spike brightening. Another difference was the spectral hardness in X-rays, which can be measured by the ratios of the counts in band 1 and 2 of HXIS. This was about 2.0 in the slow brightening and 1.6 for the main spike (in the brightest pixel). These hardness would correspond, if homogeneous source thermal emission is assumed (c.f. Mewe, Gronenschild and van den Oord, 1985), to 1.3 $\times 10^7$ and 1.45 $\times 10^7$ K respectively. We also mention that

the maximum at the main spike was registered at 23:25:49 UT after which the intensity decayed rapidly (in about 110 sec). However, there are indications that, at least in some pixels, this main spike was actually composed of two events separated by about 40 sec.

The UV data does not show clearly the start of the main spike since the large field of view rasters were interrupted at its beginning, just at 23:25:13 UT, in order to switch to the flare mode with smaller field of view and better time resolution. It is however clear that at the time of the interruption a rapid strong intensity increase occurred mainly in OV and some in Fe XXI lines at pixels corresponding to the small arch (to the southwest of the subflare site). The UV rasters resumed (in the flare mode) just after this time, but since rastering was involved, the next sampling of the flare pixels was at 23:25:25 UT. In Figure 7 we show plots of the UV intensity *vs.* time for the pixels of the flare site and the small arch. These plots show that the maximum intensity in all lines at the flare site peaked basically at the same time and simultaneously with the X-rays maximum of the main spike. The plots also show that several secondary spikes of emission were observed after the main spike. The data shows that the Fe XII intensity did not display the fast variations observed in the O V line, but instead the Fe XII emission seems to constitute a smoothing of the features observed in O V. The observed behavior can be understood in terms of the smoothing effect in some emissions due to finite ionization/recombination and excitation rates pointed out by Golub et al. (1989). Hence, the smoothing effect was not a thermodynamic effect but was just due to the slow response of the atomic species to the rapidly changing thermodynamic conditions. The Fe XXI emission showed an intermediate behavior between OV and Fe XII lines, but one must remember that the measurement of Fe XXI was severely contaminated.

Figure 7 can be compared with Figure 6 taking into account the different time scales and pixel sizes. There is a good coincidence between all the features in O V and those in X-rays, as was pointed out in other flares by Cheng et al. (1988).

Figure 7 displays the last emission spike ending at 23:35:27 UT in O V, followed by an exponential-like decay. A simultaneous last emission spike appears in X-rays (Figure 6) in the band 8-11.5 keV. The softer X-ray emission seems to end at 23:36:05 UT with a gradual decay which resembles that of the UV lines. All observations point to the end of the energy release process at the flare site between 23:35:30 and 23:36:00 UT. This is also basically confirmed by the Hα data in which no new emission is observed after this time.

7. The Development of the Big Arch

The start of the development of the "big arch" in Hα can be traced to the main X-ray and UV spike at 23:25:10 UT. This development began with a renewed brightening at locations close to the subflare site. The material of the big arch was initially superimposed on the southernmost remainders of the small arch and hence it can not be clearly identified. However, at 23:25:12 UT the new emission surpassed the locations of the small arch and became clearly differentiated. This new emission showed a different geometry with respect to the small arch (see Figure 3). The small arch displayed threads in the form of closed loops with both footpoints close to the PIL and curved tops. But, the big arch was seen as portions of material (blobs) and thread-like segments of loops which evolved rapidly changing from one frame to the next ($\sim$ 10 s). The material of the big arch was distributed over a path which initially covered a fraction of the big arch structure and progressively covered the whole arch structure. A possible alternative to our interpretation is that the initial closed loops of the small arch suddenly broke open into a larger structure, but we believe that the two arches are really different objects. In our interpretation, part of the small arch became occulted (in Hα) by new, optically thick, emitting plasma located in the line of sight closer to the observer. The Hα emission along the big arch appeared to progress at a rate of about 200 km s^{-1}, and its specific brightness decreased as it grew. Figure 8 shows a few frames displaying the evolution of the big arch. Notice that in the last of these frames some dark streaks of absorption have appeared all along the arch.

Figure 9 shows the decay of the arch as it continued progressing toward the secondary footpoint turning completely to absorption. The change to absorption occurred in the form of streaks which first appeared at the arch top and subsequently extended toward the subflare site. At about 23:35:02 UT the whole arch is dark and the PIL filament has reappeared indicating that the low-lying loops of the small arch have already disappeared. At this time the arch has reached the secondary footpoint at about 45000 km projected distance from the subflare site, corresponding to about 110000 km in actual distance, which makes the arch $\sim$ 300000 km long. Also around this time the images display most clearly the structure of narrow filaments which composed the arch; their measured thickness was close to the resolution of the Hα photographs and hence their actual thickness was at or below 1". The last frame shows that at 23:49:46 UT most of the arch has vanished, at this time only a portion close to the secondary footpoint remained visible. In our interpretation the higher visibility of this portion was due to the close alignment between this segment of the arch and the line of sight. Then at 23:50:46 UT this leg started becoming transparent and the entire arch disappeared by 23:52:36 UT.

The UV light curves for the pixels of the arch are given in Figure 10. It is obvious in this figure that there was a delay in the emission when going from the subflare site to the west. However, it is hard to give precise figures on the timing because of the changing shapes of the emission at different pixels, those to the west being progressively smoother. The pixel closer to the subflare site, and partially the next one as well, showed a relatively high level of counts at the beginning of the small raster sequence, due to a contribution of the small arch emission. A steep intensity increase in O V apparently related to the main spike occurs at 23:25:43, 23:25:59, 23:27:31, and 23:28:58 UT for the pixels with centers at about 10, 20, 30, and 40" (see Figure 4b) distance from that at the flare site. Figure 10 also shows that the Fe XXI emission had smoother behavior than the O V (e.g., characteristic decay time of 6 min compared to 1 minute in O V). Also the Fe XXI features (i.e. rise, maximum and decay) seem to have preceded those of O V by about 2-3 minutes. The Fe

XII data suggests that the behavior in this line was even smoother than that of OV and Fe XXI, but the large background and noise levels make uncertain the timing of the emission. Another interesting fact displayed by Figure 10 is that the decay rate was minimum at the pixel near the arch top and increases toward the secondary footpoint. This may be interpreted as an indication of lower density at the arch top which would have the slowest radiative cooling rate. However, it can also be explained in a homogeneous density model by the maximum distance from the apex to the cool footpoints which gives the slowest conductive cooling of the material.

The X-rays from the big arch had much lower intensity than the subflare site (about 8 times less or smaller in the band 3.5-5.5 keV). In Figure 11 we show the X-ray light curves for the big arch pixels in the HXIS FOV. It is not possible to discern absolutely between the emission of the big arch and that of the small arch in the pixels located at smaller distance than 20" from the flare site. However, the emission from the small arch started earlier and seems to be already decaying by the time of the main spike. In addition, the emission from the big arch seems to be slightly displaced to the south of that of the small arch. Early X-ray emission was observed all along the big arch structure prior to the main spike. This emission extended up to the boundary of the HXIS FOV and thus practically reached the secondary footpoint. In spite of the noise present in the data it is clear that an emission spike occurred at the time of the subflare main spike in the pixels of the big arch close to both footpoints.

Also some secondary spikes seem to have occurred more or less in correspondence with the spikes at the subflare site with practically no delay. But, it is striking that in the pixels near to the arch top the emission started before the main spike, e.g. the brightening started at 23:23:39, 23:24:11 and 23:24:44 UT in the pixels located at 44, 52, and 60" (see Figure 4a) from the subflare site. The difference between the pronounced spikes at the subflare site and the shallower pattern of the fast rise and slow decay at the arch pixels

makes it clear that the latter emission was not just an instrumental effect (a ghost). The high noise makes it impractical to compare the counts in different X-ray bands.

There are two facular areas, to the west of the included polarity, which are sites of some activity in Hα, UV and X-rays. The UV and X-ray emission levels in these areas are small compared with that of the subflare. However, since they extend underneath the big arch the activity in these plage areas may contaminate our measurements for some pixels of the big arch (namely those at 20 and at 40" distance from the subflare site, see Figure 4). Analyzing in detail the Hα data we find that several small brightening occur in these plages and some enhancement is visible on the facular area closer to the flare site. However, the plages are almost perpendicular to the big arch and the brightening occur are mostly to the north of the arch. We believe that these facular areas only contribute to enhanced background at some pixels and do not affect our conclusions.

8. Discussion and Conclusions

The event we study starts with a compact subflare taking place in an "included" magnetic polarity of an otherwise magnetically simple active region. The subflare is not related to flux emergence because no new field is involved.

The magnetic remote connection between the included polarity and the main sunspot of the region (leading spot) became evident during and after the subflare as a big arch developed along it. This flaring arch, about 300000 km long, was seen within a wide range of radiation energies, from optical to X-ray wavelengths, spanning a range of temperatures between 10^4 and 10^7 K (cf. Martin and Svestka 1988). The flaring arch lasted beyond the end of the subflare showing that the structure of the magnetic connection was not basically affected by the subflare. The narrow threads and blobs in the arch observed in Hα demonstrate that the magnetic tubes did not expand or merge, but remain substantially the same at sizes below the achieved resolution of few arc sec, as they cross the corona.

The existence of interacting arch structures in flares has been found in X-ray observations (Machado et al. 1988a, 1988b). Our data also shows that there was also a group of small loops (small arch, $\sim$ 30000 km long) connecting both sides of the PIL.

The small Hα loops which compose the small arch are similar to post-flare loops and probably developed from flare-loops as result of condensation of the hot ablated material. This is also consistent with the UV and X-ray observations. However, the big arch constituted a well differentiated phenomenon with a different origin. We interpret its behavior as displaying the ejection of material along some magnetic tubes which are adjacent to those directly involved in the reconnection process. Probably, a sudden exchange of energy between the small flaring loops (which form the small arch) and the more extended loops (which form the big arch skeleton) powers the ejection of material along the extended structure. This scenario has some similarity to that proposed by Machado et al. (1988), in which a passive loop is impacted by an active loop, but it is different in that here apparently the injection of energy in the passive (the big arch) loops takes place in upper chromospheric rather than in coronal layers. It is for this reason that some portions of cool dense material, above the region where the energy exchange takes place, become ejected by the strong overpressure which develops in the energy exchange region. Notice the similarity of our scenario to that discussed by Harrison et al. (1988) for surges and related X-ray emission.

The cool dense "plug" of material may heat up and expand as it travels upwards accelerating up to the sound speed of the driving heated material. In other lower-density threads the heating dominates the process and the ejected material has high initial temperature, although its emission is weak due to its low density. The ejection velocity is larger for these hot low-density threads because of their small mass. Similar characteristics of other flaring arches have been found in Papers I and II.

We propose that transfer of energy across the field lines could occur in the chromospheric layers by MHD waves propagating from a reconnection site located within these chromospheric layers. If a layer in the upper chromosphere with a pressure about 10 dyn cm^{-2} undergoes sudden heating up to 10^7 K due to the compression in wave front, its pressure may reach values as high as 10^4 dyn cm^{-2}. The plasma beta considerations show that this value of the overpressure can drive substantial MHD shocks across the magnetic field for field strengths as high as 500-1000 G (plasma beta 1-0.25). The pressure disturbance will be rapidly dissipated by both radiation and by generating upflows of material.

In this scenario, we can designate the ejection, that fills the magnetic structure of the big arch with plasma, as a true "chromospheric explosion". This scenario poses some interesting problems to the energetics of the subflare itself, since a large fraction of the released energy may be transferred by the process we suggest into coronal structures of low specific brightness (emission per unit of volume and time) but large volume and which decay slowly. This energy may then provide a way of dissipating the small-flare energy into large-scale coronal heating, and it implies that the radiative emission from the cores of at least some of the very small flares is an underestimate of the total energy released in such events. The scenario presented here is consistent with the one proposed by Fontenla et al. (1989) for smaller UV events.

Acknowledgements

J. Fontenla acknowledges support from NASA's Office of Space Science and Applications through the Solar Physics Branch of the Space Physics Division, grant NAG8-171. The development and construction of the HXIS was made possible by support from the Netherlands Ministry for Education and Science, and the Science and Engineering Research Council of the United Kingdom.

REFERENCES

Cheng, C., Vanderveen, K., Orwig, L.E., and Tandberg-Hanssen, E.: 1988, *Astrophys. J.*, **330**, 480.

Cohen, L.: 1981, *An Atlas of Solar Spectra Between 1175 and 1950 Angstroms Recorded on Skylab with the NRL's Apollo Telescope Mount Experiment*, NASA Reference Publication 1069, Greenbelt, MD.

de Jager, C., and Svestka, Z.: 1985, *Solar Phys.*, **100**, 435.

Fontenla, J.M, Tandberg-Hanssen, E., Reichmann, E.J., and Filipowski, S.: 1989, *Astrophys. J.*, **344**, 1034.

Golub, L., Hartquist, T.W., and Quillen, A.C.: 1989, Solar Phys., **122**, 245.

Harrison, R.A., Rompolt, B., and Garczynska, I.: 1988, *Solar Phys.*, **116**, 61.

Hirayama, T.: 1985, *Solar Phys.*, **100**, 415.

Machado, M.E., Moore, R.L., Hernandez, A.M., Rovira, M.G., Hagyard, M.J., and Smith, J.B. Jr.: 1988a, *Astrophys. J.*, **326**, 425.

Machado, M.E., et al. : 1988b, *Astrophys. J.*, **326**, 451.

Martin, S.F., and Svestka, Z.: 1988, *Solar Phys.*, **116**, 91 (Paper I).

Mewe, R., Gronenschild, E.H.B.M., and van den Oord, G.H.J.: 1985, *Astron. Astrophys. Suppl.*, **62**, 197.

Svestka, Z., Fontenla, J.M., Machado, M.E., Martin, S.F., Neidig, D. F., and Poletto, G.: 1987, *Solar Phys.*, **108**, 237.

Svestka, Z., Farnik, F., Fontenla, J.M., and Martin, S.F.: 1989, *Solar Phys.*, **123**, 317 (Paper II).

Van Beek, H.F., Hoyng, P., Lafleur, B., and Simnett, G.M.: 1980, *Solar Phys.*, **65**, 39.

Woodgate, B.E., Tandberg-Hanssen, E.A., Bruner, E.C., and 11 co-authors: 1980, *Solar Phys.*, **65**,73.

Table I

Chronology of observed events in the early phase

Time (UT)	Data	Feature	Event
23:10:20	Hα	Flare site	Brightening begins.
23:17:09	Fe XXI	Flare site	Brightening slope increases.
	O V	Flare site	Brightening slope increases.
23:18:51	Hα	Flare site	Brightening masks neutral line filament.
23:19:53	Fe XII	Flare site	Brightening begins.
23:20:40	X-rays	Flare site	Brightening begins.
23:21:30	X-rays	Small arch	Top brightens.
23:22:29	Fe XXI	Small arch	Top brightens.
	O V	Small arch	Top begins brightening.
23:23:11	Hα	Small arch	Fast growth starts.
23:23:47	Hα	Small arch	Reaches maximum size and brightness.
23:23:51	Fe XII	Small arch	Top brightens.

Table II

Chronology of observed events during the big arch development

Time (UT)	Data	Feature	Event
23:23:39	X-rays	Big arch	Emission starts close to the apex.
23:24:28	X-rays	Big arch	Steep rise close to the 2nd footpointbase.
23:24:41	Hα	Big arch	Dynamic emission starts at the base.
23:25:12	Hα	Big arch	Emission surpasses the small arch.
23:26:15	O V	Big arch	Start of emission close to the apex.
23:26:21	X-rays	Big arch	Peek of the emission close to the apex.
23:26:51	Hα	Big arch	Maximum growth speed, dark streaks start.
23:27:40	O V	Big arch	Start of emission close to the 2nd footpoint.
23:27:40	X-rays	Big arch	Peek of emission close to the 2nd footpoint.
23:29:17	O V	Big arch	Maximum emission close to the apex.
23:29:32	Hα	Big arch	Emission reaches the apex, dark streaks reach primary footpoint.
23:32:22	Hα	Flare site	New emission patches appear to the south.
23:34:23	O V	Flare site	Secondary peak.
23:34:23	Fe XXI	Flare site	Secondary peak.
23:34:28	X-rays	Flare site	Secondary spike (hardest spike).
23:35:22	Hα	Big arch	Reaches the secondary footpoint.
23:36:32	Hα	Big arch	Fully developed, mostly thick absorption.
23:47:43	Hα	Big arch	Part starts becoming transparent.
23:47:43	Hα	Flare site	The brightening has decayed completely, the neutral line filament reappears.
23:49:46	Hα	Big arch	The primary leg has dissapeared.
23:53:46	Hα	Big arch	Has completely dissapeared.

Figure 1. The structure of the longitudinal magnetic field. The data shown was obtained on June 24 when the region was far from the limb. Other data secured on June 27 is affected by large projection distortions because the proximity of the region to the limb. However, this later data shows that the magnetic structure on June 27 is essentially the same as the shown in this figure. Solar north is upward. The features are: A, main sunspot ($\sim$ 2800 G); B, included polarity ($\sim$ 700 G); C, secondary leading polarity sunspot group ($\sim$ 1500 G); O, trailing sunspot group ($\sim$ 1800 G).

Figure 2. (a) the offband Hα image obtained shortly after our event. It displays the locations and sizes of the sunspots and traces of filament material. Celestial north is upward. The features are: A, main sunspot; B, subflare site; C, secondary leading polarity sunspot group. The trailing sunspot group is out of the field of view. Notice that this first panel is slightly offset respect the following. (b) Hα line center image of the active region before our event started. It displays several facular areas, and particularly the one associated to the included polarity, which is half encircled by the neutral line filament. We indicate the neutral line filament (D). (c) the start of the subflare at 23:18:16 UT. Note a much smaller flaring at a location (L) distinct from the secondary footpoint of the big arch (see below).

Figure 3. Schematic diagram of the locations of the small and the big arch. The direction to the observer is indicated to show the overlapping between both arches.

Figure 4. Schematic diagram showing the locations of the main features of our event and the HXIS fine field of view (panel a) and UVSP small rasters (panel b). The pixels relevant to the flare site and the big arch in the X-rays and UV data are indicated by shading. The feature A is the main leading sunspot, and the feature B is the subflare site. The drawings are superimposed on Hα pictures obtained at 23:28:31 UT (a), and at 23:32:22 UT (b).

Figure 5. Hα images showing the development of the small arch. The data corresponds to: a) 23:23:17, b) 23:23:41 and c) 23:24:46 UT. The small arch is indicated in the second

panel. The last two frames show the small arch fully developed and practically unchanged. Notice some small offset and not very good seeing conditions of the last frame.

Figure 6. Plots of the temporal evolution of the X-rays intensities in the pixels of the subflare and the small arch (heavily shaded in Figure 4a). Both axis scales are the same for all pixels plots. These plots correspond to the fine FOV and are accumulated over 7.5 s. The plots correspond to: a) 3.5-5.5 keV, b) 5.5-8.0 keV, and c) 8-11.5 keV bands.

Figure 7. Plots of the temporal evolution of the intensities of the UV lines in the pixels corresponding to the subflare and the small arch (heavily shaded in Figure 4b). Both axis scales are the same for all pixels plots. These plots correspond to the fast sequence of small rasters. The plots correspond to the a) OV, b) Fe XXI, and c) Fe XII lines.

Figure 8. Hα images showing the development of the big arch. The change from emission to absorption is displayed by the last two images. The data corresponds to: a) 23:25:35, b) 23:26:01 and c) 23:26:51 UT.

Figure 9. Hα images showing the decay of the big arch. The whole arch is in absorption and it reaches the secondary footpoint. The top becomes transparent in the last image shown. The data corresponds to: a) 23:28:31, b) 23:32:22 and c) 23:49:46 UT. The big arch and the location of its secondary footpoint are indicated in the second panel.

Figure 10. Temporal evolution of the intensities of the UV lines in the pixels of the big arch (lightly shaded in Figure 4b). Both axis scales are the same for all pixels plots. The rightmost plots correspond to the pixels close to the secondary footpoint. The plots correspond to the a) O V, b) Fe XXI, and c) Fe XII lines.

Figure 11. Temporal evolution of the intensities of the X-rays in the pixels of the big arch (lightly shaded in Figure 4a). Both axis scales are the same for all pixels plots. The rightmost plots correspond to the pixels close to the secondary footpoint. The plots correspond to an accumulation over 7.5 s and over two bands spanning 3.5-8.0 keV.

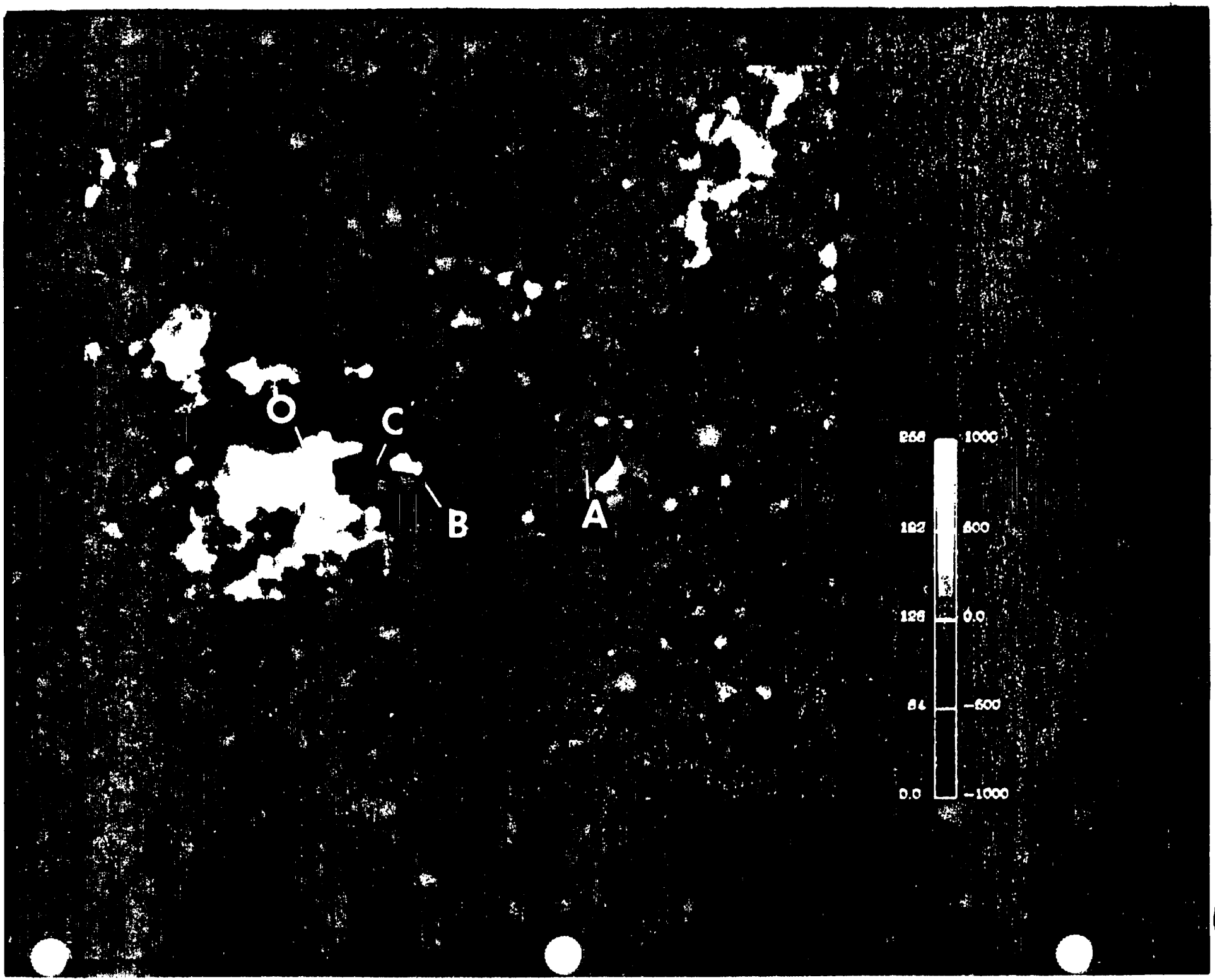
O
C
B
A
256
192
128
64
0.0
1000
500
0.0
-500
-1000

Fig

D

Exh 2

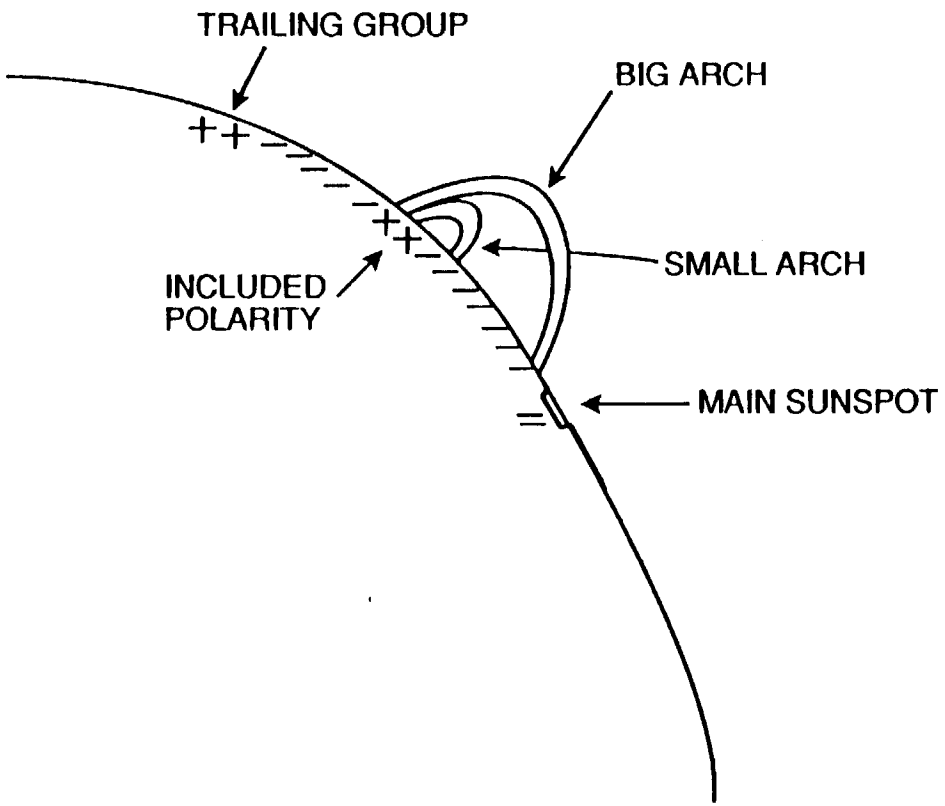

Fig. 3

11175-0-291

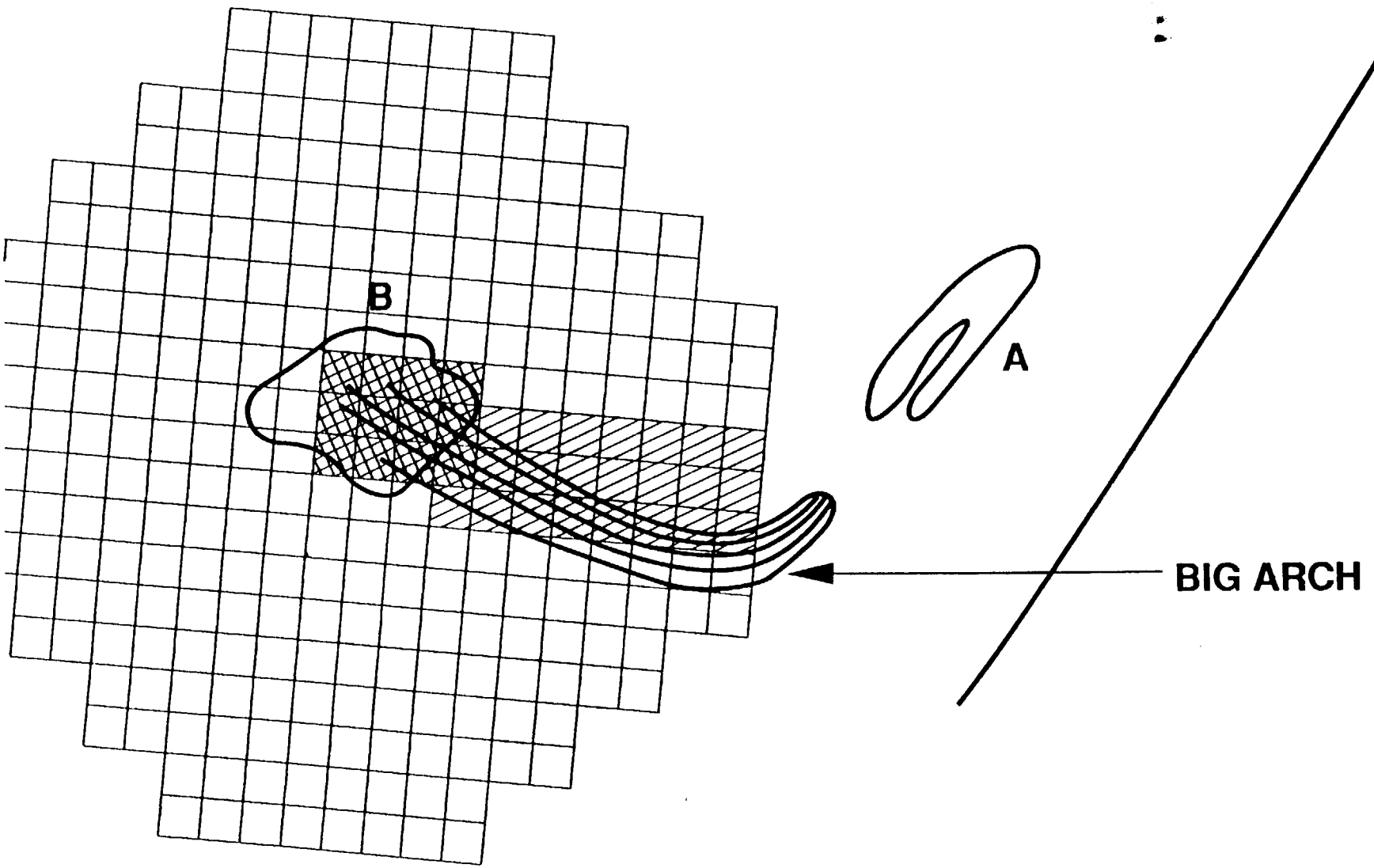

5-10095-0-235

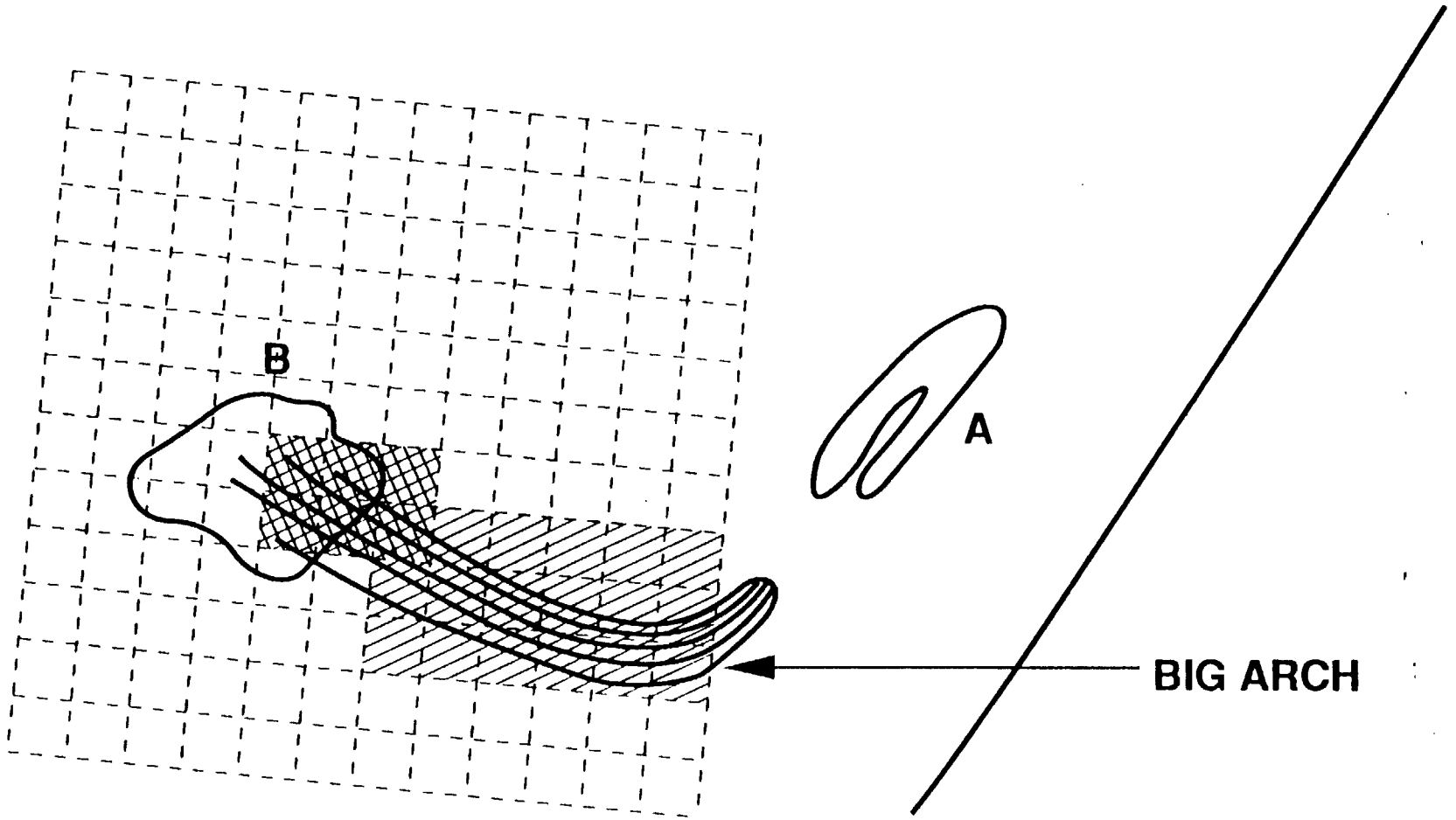

5-10096-0-235

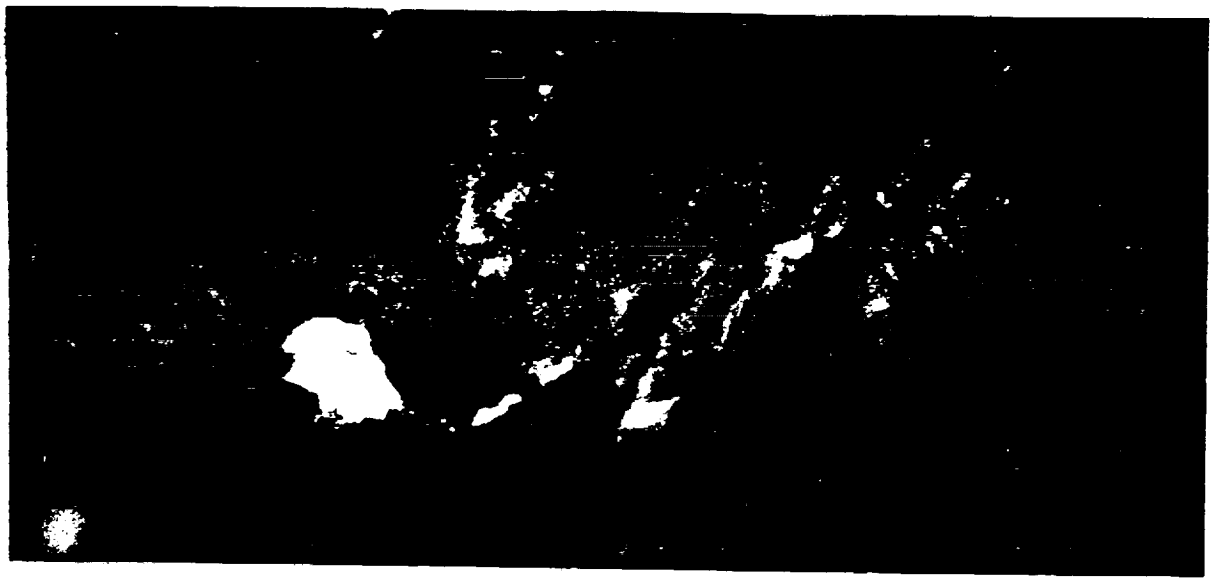

a

b

c

Fig. 3

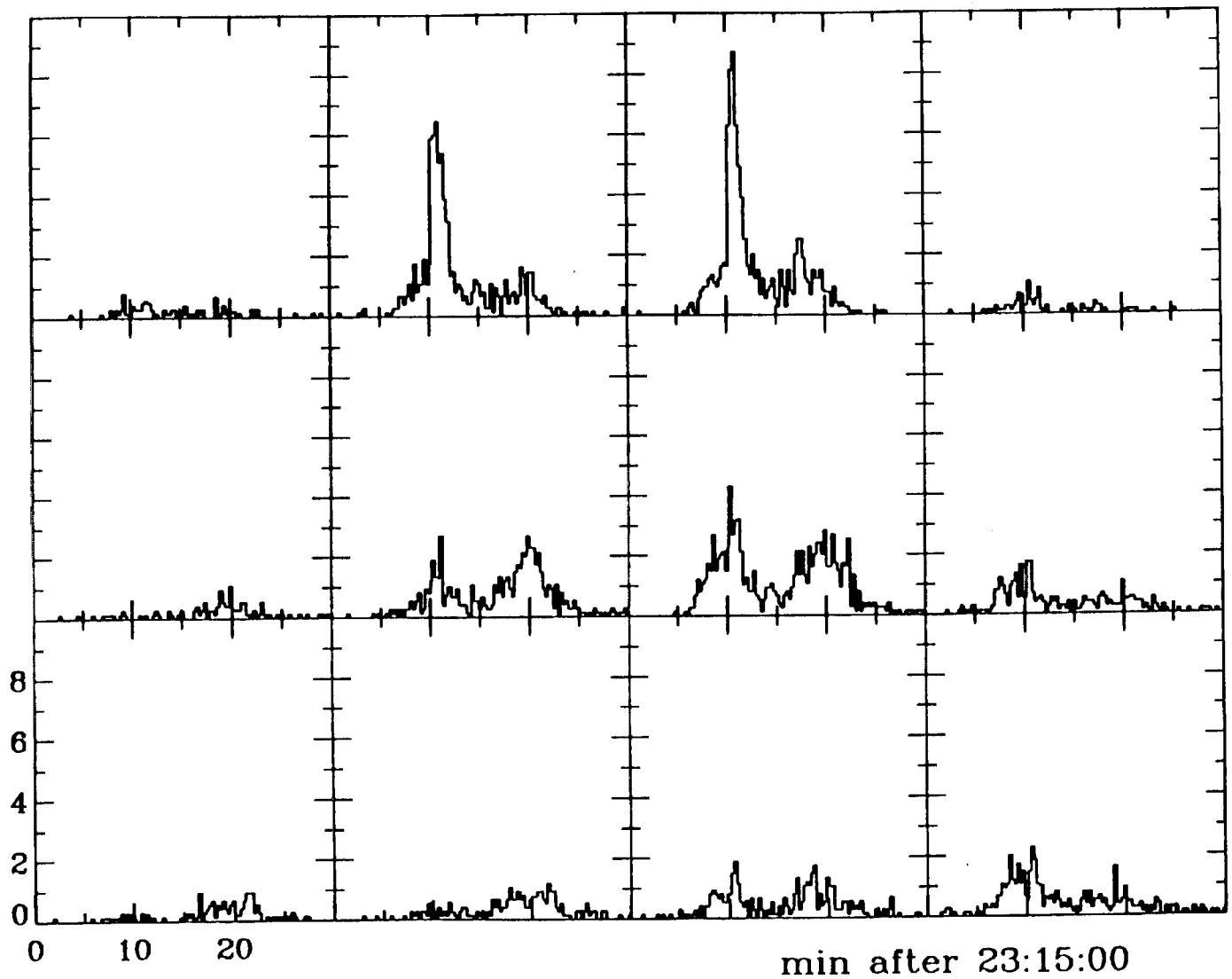

Fig 6a

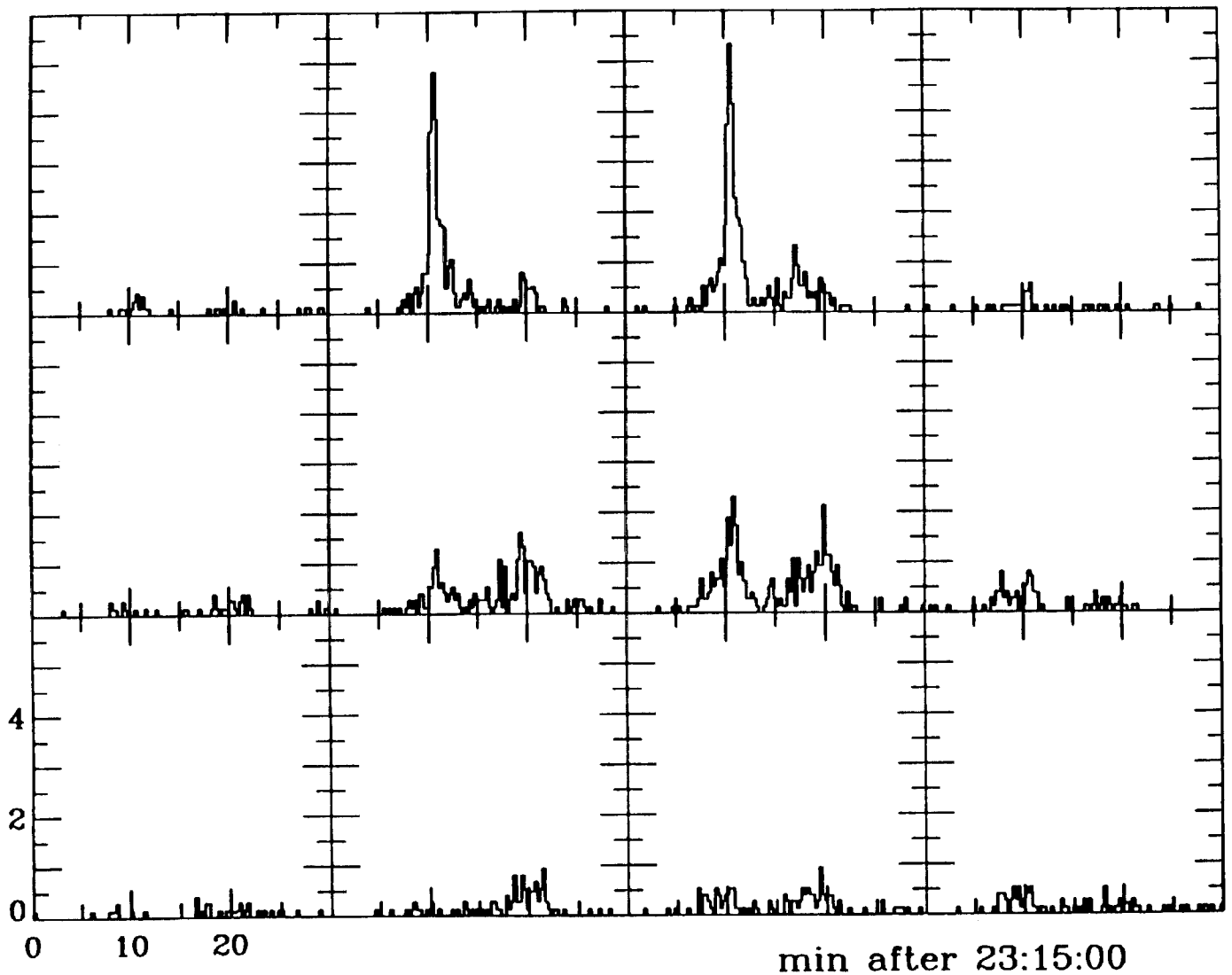

Fig 6

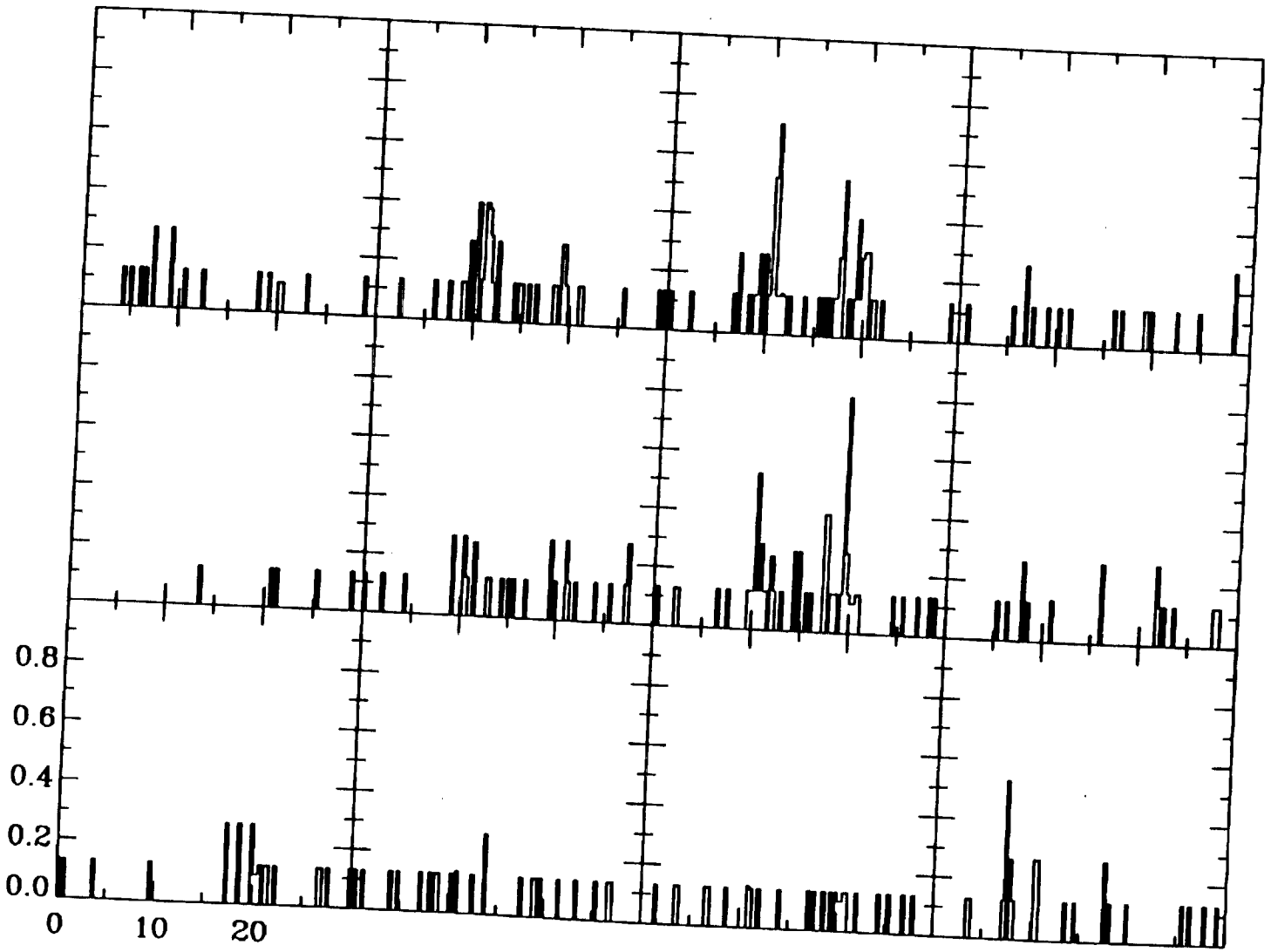
0.8
0.6
0.4
0.2
0.0
0
10
20
min after 23:15:00

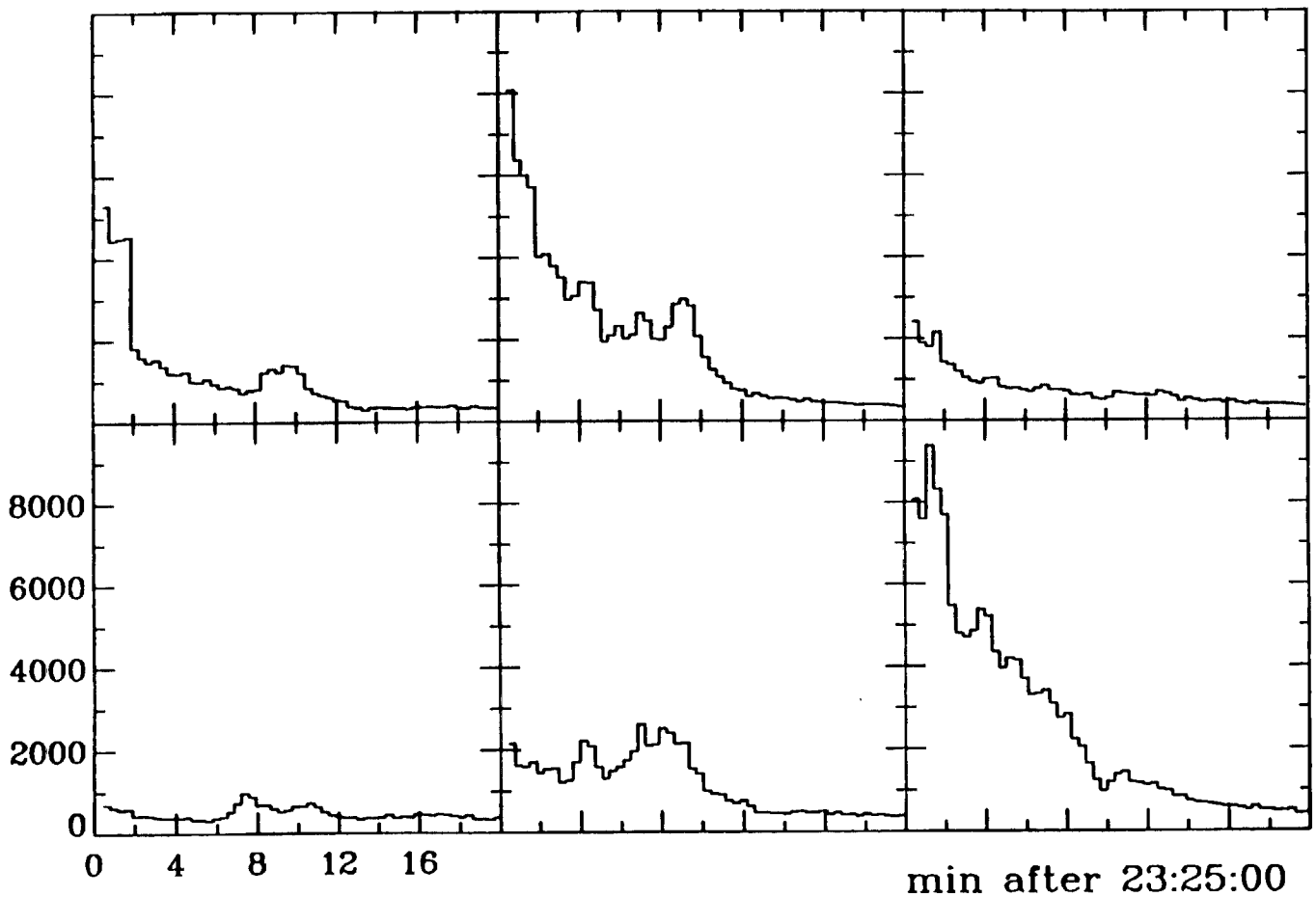

Fig 7a

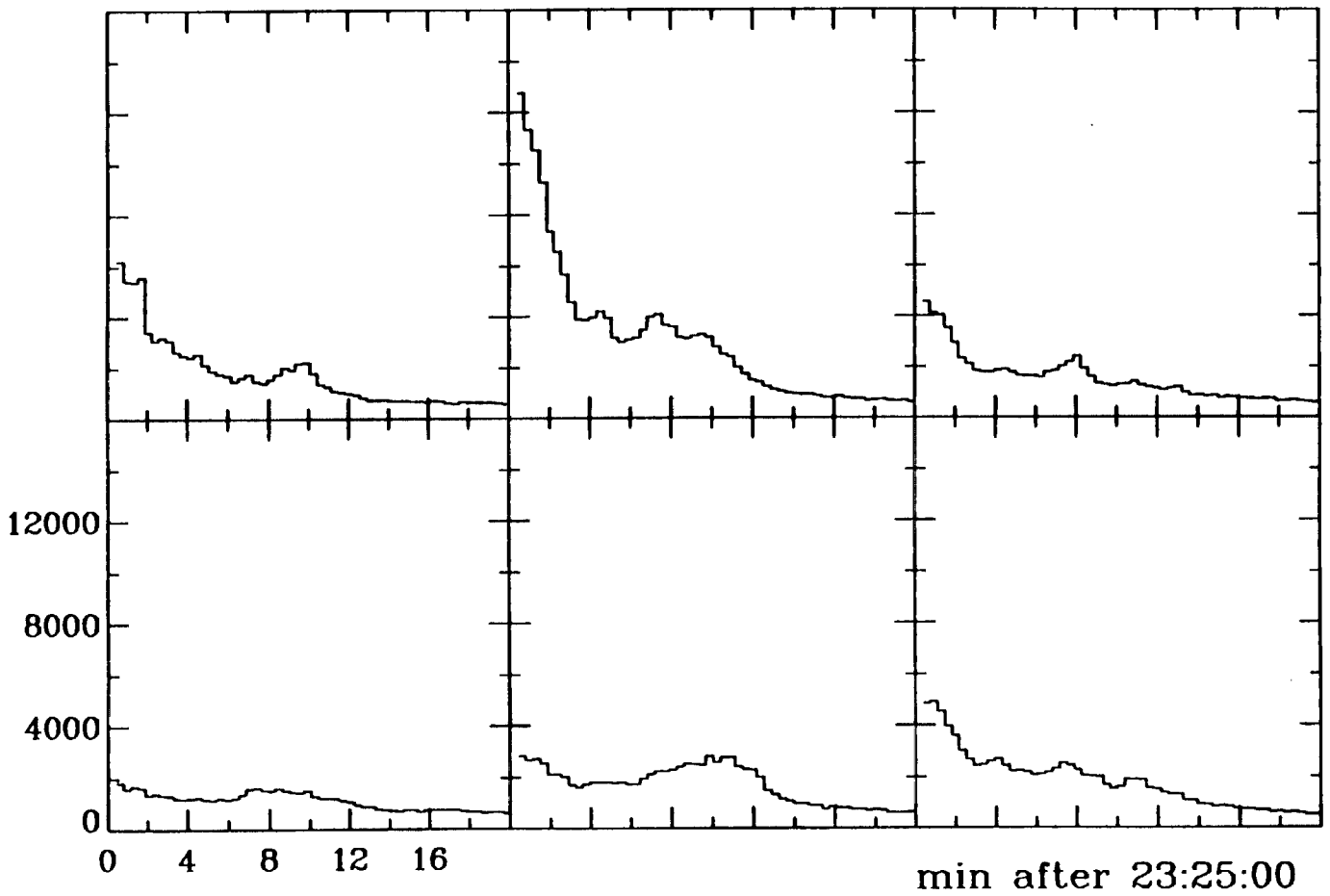

Fig 76

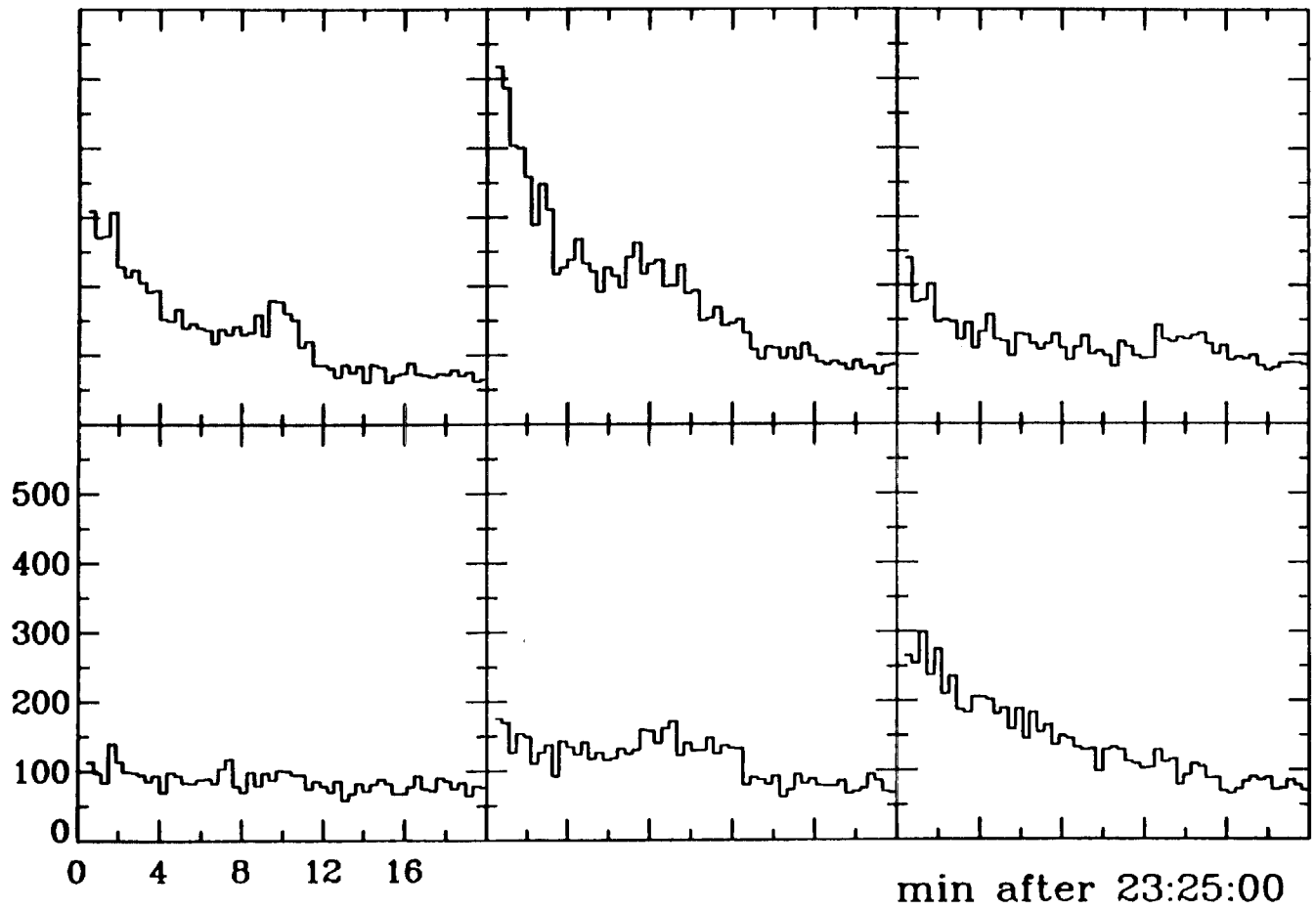
500
400
300
200
100
0
0
4
8
12
16
min after 23:25:00

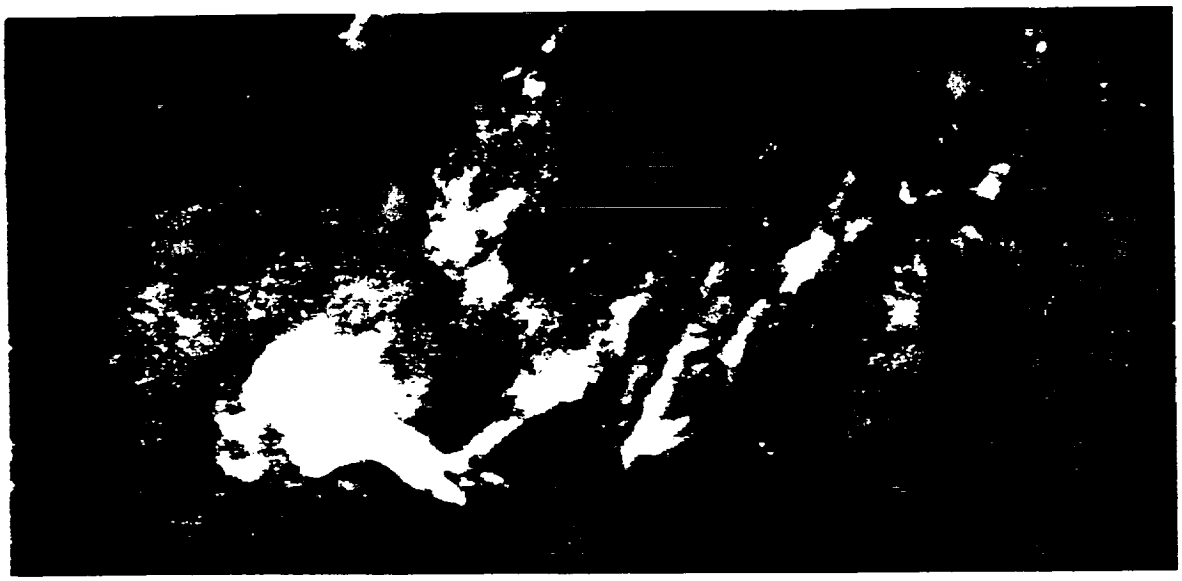

a

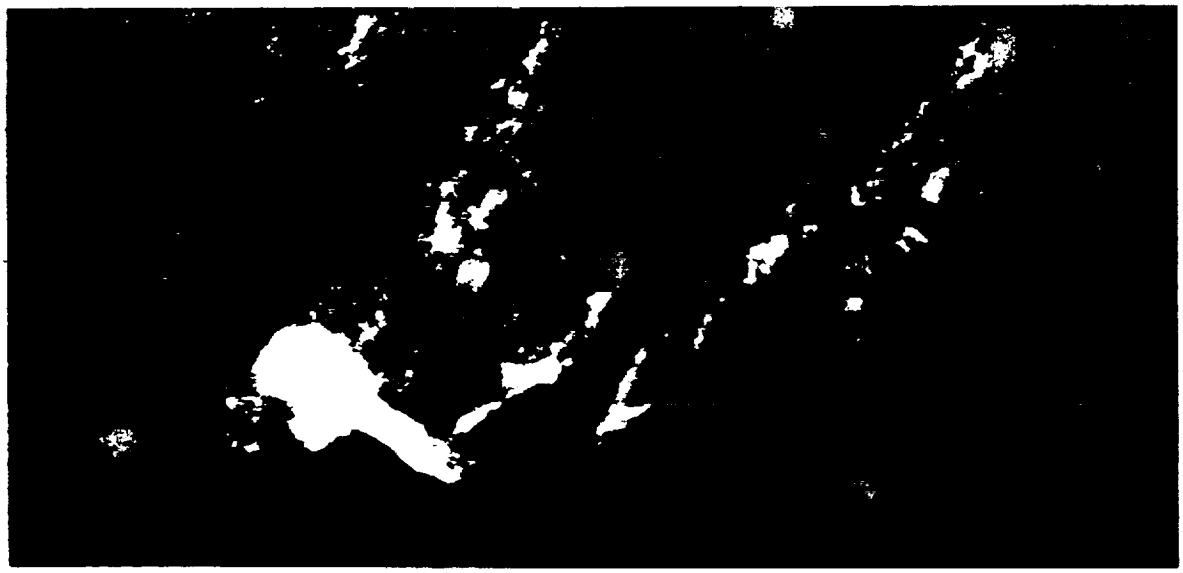

b

c

Fig. 3

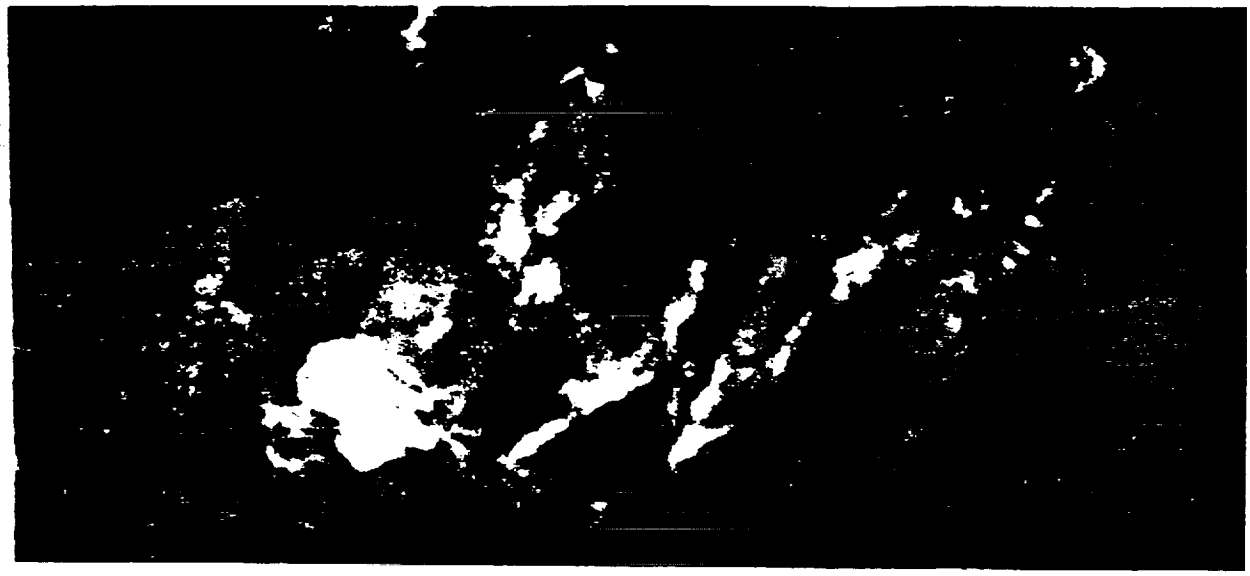

a

b

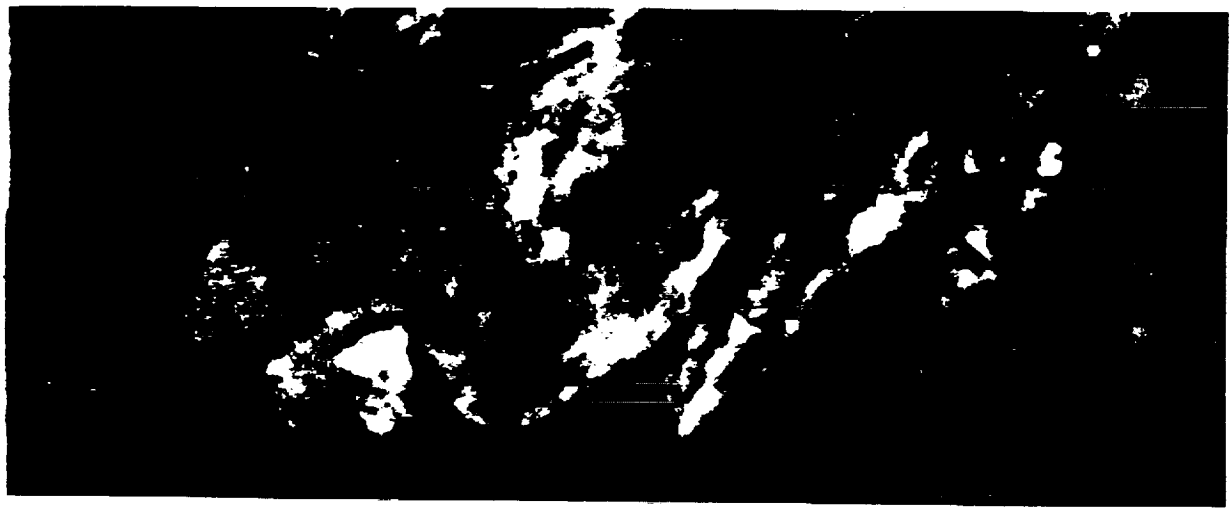

c

Fig. 9

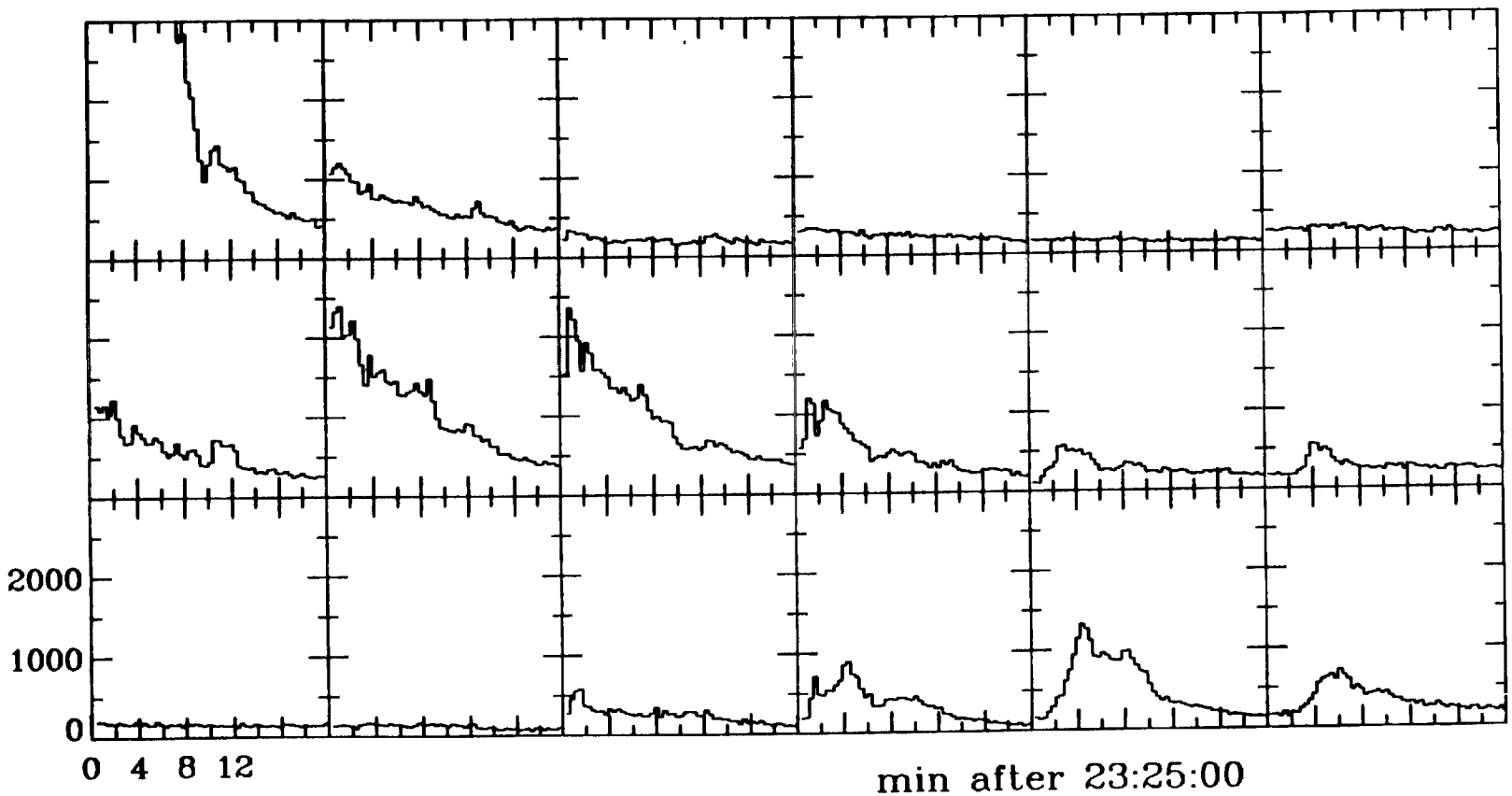

Fig 10a

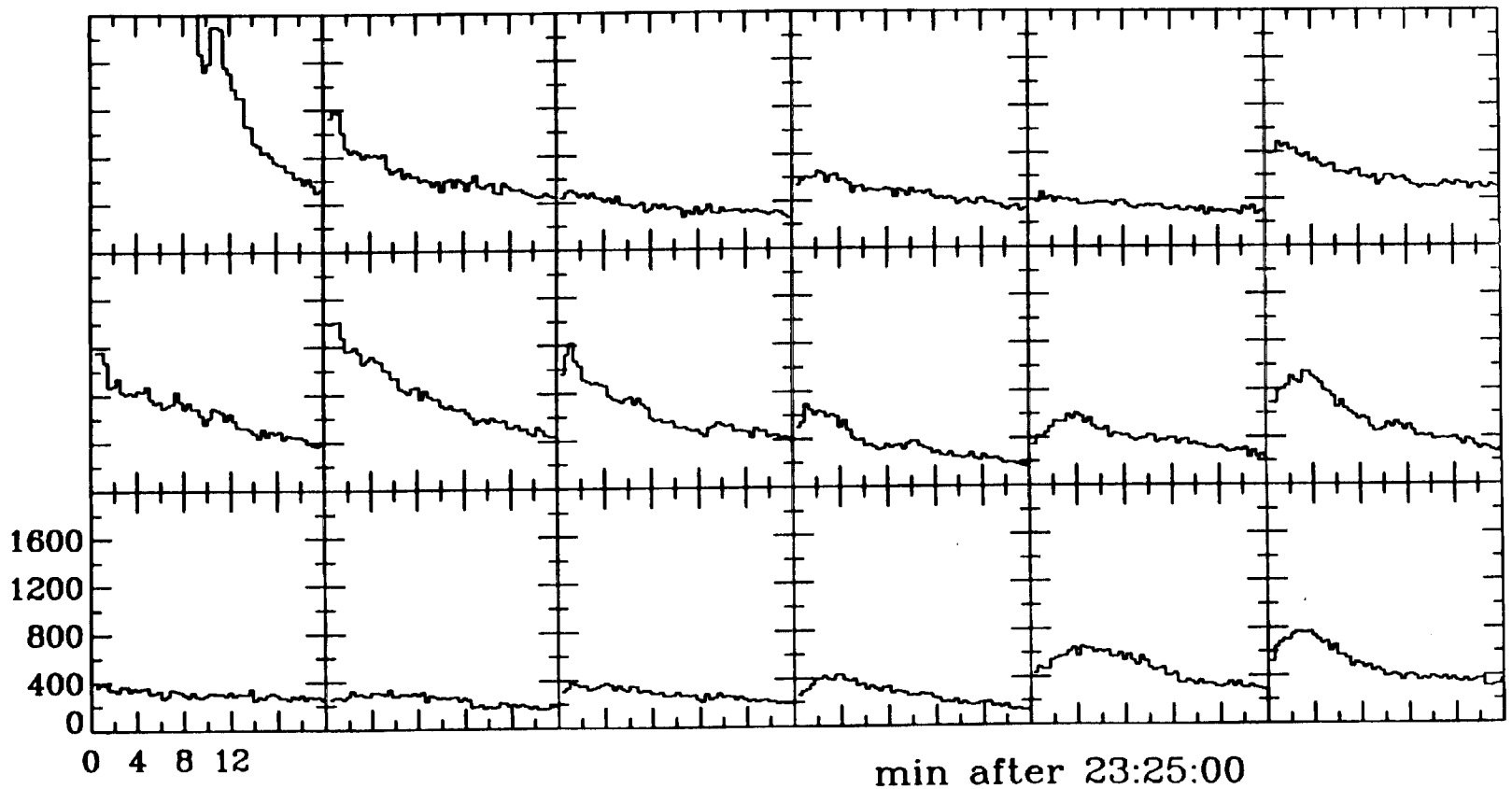

Fig 10

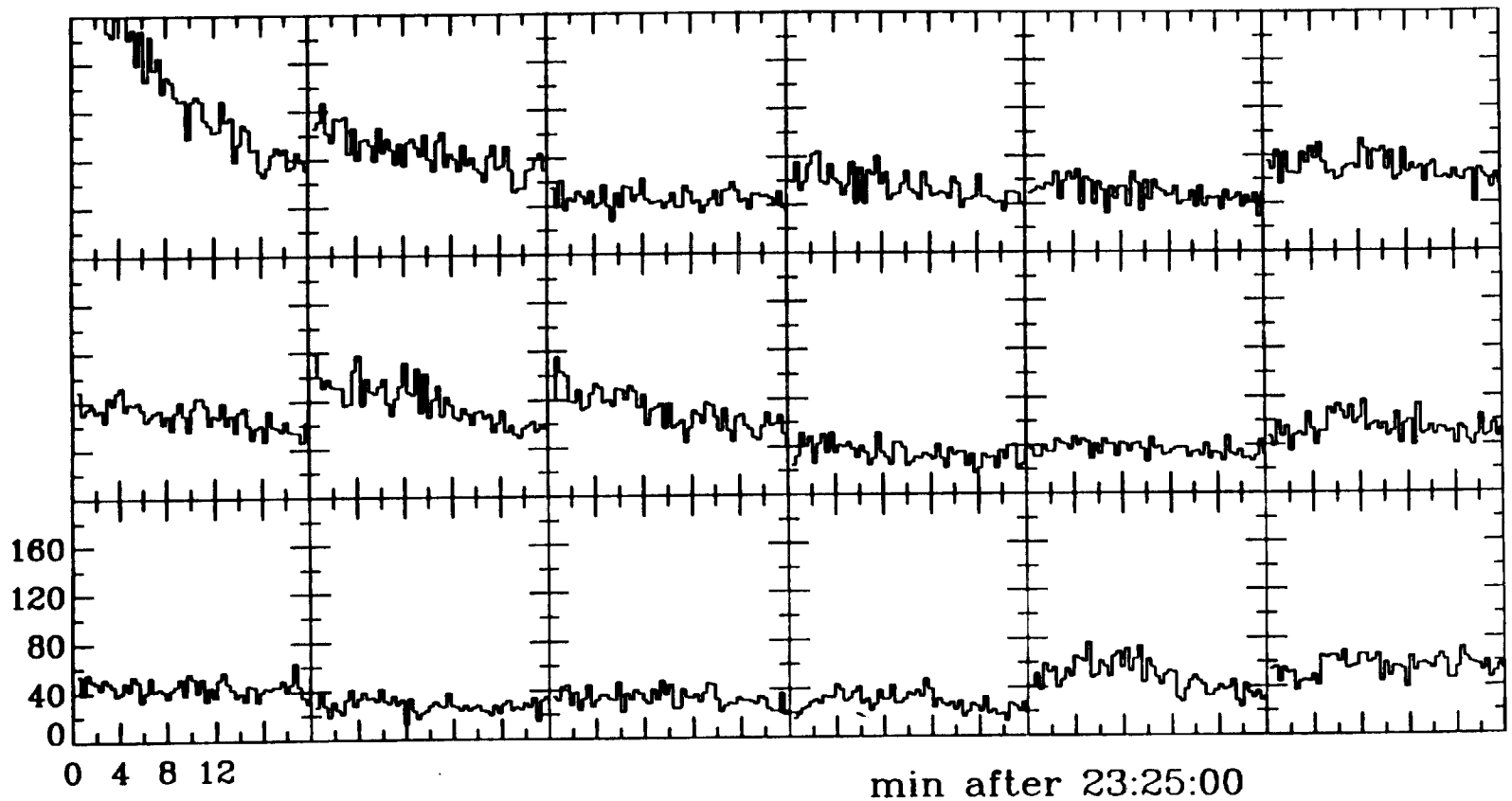

Fig 10c

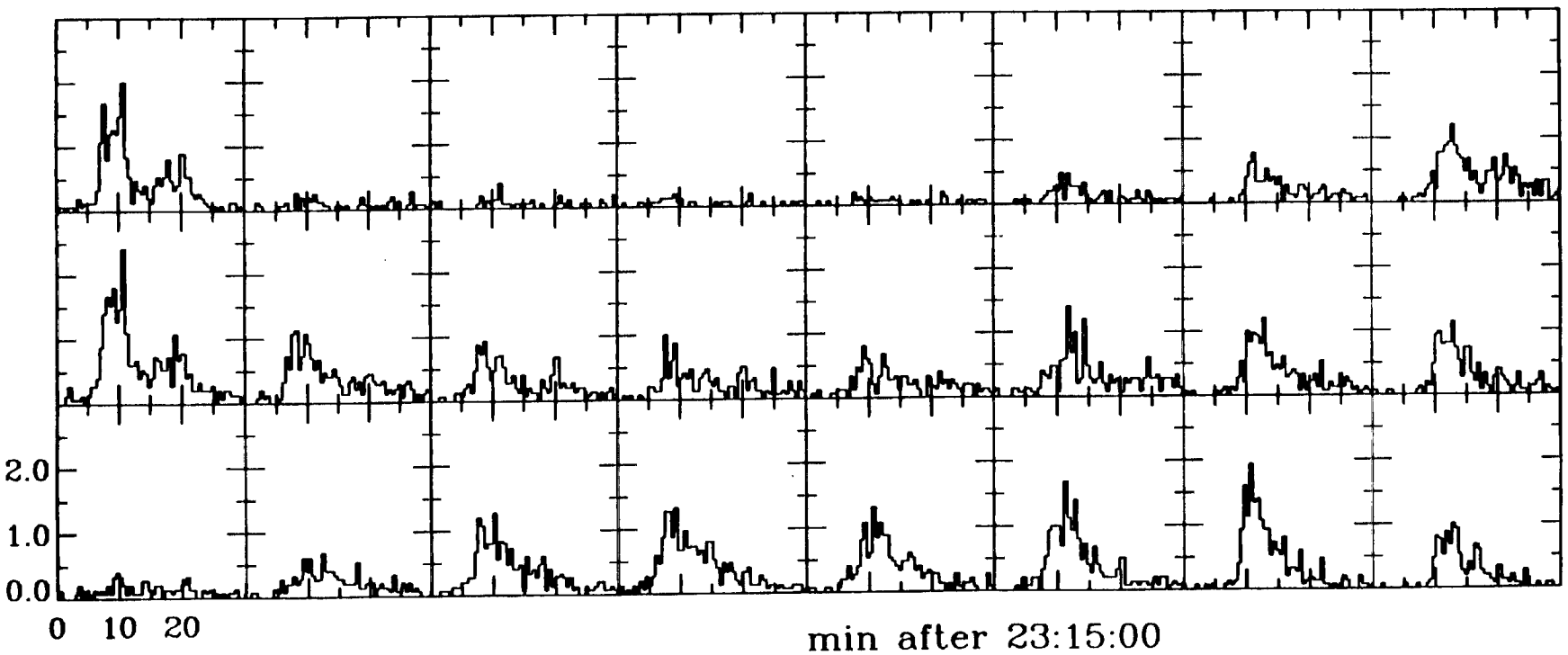

Fig 11

ENERGY BALANCE IN THE SOLAR TRANSITION REGION

II. Effects of Pressure and Energy Input on Hydrostatic Models

J.M. Fontenla[1]

CSPAR/ The University of Alabama in Huntsville

E.H. Avrett and R. Loeser

Harvard-Smithsonian Center for Astrophysics

60 Garden Street

Cambridge, MA 02138

to appear in Ap. J.

Submited: 1990 Nov 14;

Received:

Revision:

[1] present address: Space Science Laboratory ES52, NASA Marshall Space Flight Center, Huntsville, AL 35812

Abstract

In this paper we address the question of how energy is radiated by hydrogen lines and continua in hydrostatic energy-balance models of the transition region between the solar chromosphere and corona. Our models assume that mechanical or magnetic energy is dissipated in the hot corona and is then transported toward the chromosphere down the steep temperature gradient of the transition region. This model can be applied to the lower portions of magnetic flux tubes in which the temperature varies from chromospheric to coronal values, and to either open field or loop models. The basic difference between our calculations and those of other authors is that our theoretical hydrostatic energy-balance models properly take into account the diffusion of hydrogen atoms and ions. Diffusion, which was introduced in a previous paper, arises naturally due to the concentration and temperature gradients and is characterized by the ambipolar diffusion velocity. The diffusion effects are used in both the statistical equilibrium and energy balance equations and, as shown earlier, give order of magnitude agreement between calculations and the observations of the hydrogen Lyman continuum and Lyman lines in the average quiet Sun. The present paper describes various models constructed for the transition regions that correspond to different features of the solar atmosphere. Our calculations give the magnitude and distribution of energy radiated by the lower transition region after being transported down from the corona. We find that our models not only explain the average quiet Sun but also the entire range of variability of the Lyman alpha lines. We describe the relations between the downward energy flux, the pressure of the transition region, and the different hydrogen emissions. We show how the usual optically thin radiative loss curve can be modified to give agreement with our detailed calculations, and the extent to which this method can be used for estimating the actual radiative losses. Also, we show how the usual emission measure method can be modified to treat the Lyman alpha line emission, and we discuss the limitations of the emission measure approach.

Subject headings: diffusion - plasmas - radiative transfer - Sun: atmosphere - Sun: transition region.

1. Introduction

Since the discovery of coronal and chromospheric emission lines due to elements in high and in low ionization stages, respectively, it is known that there is a strong temperature variation in the outer layers of the solar atmosphere. The temperature rises steeply from chromospheric values (6000-8000 K) up to coronal values (1-2 $\times 10^6$ K) in a narrow layer called the transition region (see reviews by Athay 1981, 1988; Withbroe 1981; Mariska 1986). UV and EUV observations from space have shown that the transition region produces strong line emission at such wavelengths. Most of the emission lines of trace elements (i.e., elements other than H or He) are believed to be produced in an optically thin layer, and these emissions produce a characteristic bright rim at the outer edge of the solar disk. This rim is not clearly observed in the lines which are produced in optically thick layers, e.g. the H and He resonance lines.

The initial attempts to derive the temperature structure of the transition region consisted of semiempirical modeling (e.g. Potasch 1964; Dupree 1972). These models related the observed line intensities to the "emission measure" EM which can be expressed in the standard form

$$EM = n_e n_H (dlnT/dz)^{-1}. \quad (1)$$

These calculations involve several assumptions, e.g., optically thin layers, exclusively collisional excitation and ionization, and ionization degree locally given by the ionization and recombination rates (in recent calculations, including dielectronic processes). The curves of EM *vs.* height that result from this semiempirical modeling display a characteristic V-shape in all solar features. The temperature of the minimum emission measure ($T_a \simeq 160,000$ K) allows us to characterize the upper transition region by $T > T_a$ and the lower transition region by $T < T_a$. Most of the emission from the transition region originates at $T < T_a$ and is due to lines of elements in neutral or in low ionization stages. The most important single lines are the first resonance lines of H (Lyα, 1216 Å) and He II (304 Å), which emit, respectively, about 20 %

and 3 % of the total radiative emission from the transition region (i.e., $\simeq 2 \times 10^5$ and $\simeq 3 \times 10^4$ erg cm^{-2} s^{-1} flux at the solar surface). Other strong observed lines corresponding to higher temperatures (close to T_a) are the well-observed C IV resonance lines (1548 and 1550 Å) which, however, only account for about 1 % of the total emission (i.e. $\simeq 10^4$ erg cm^{-2} s^{-1}).

The upper transition region emission measure for the average quiet Sun is consistent with a constant heat flux due to classical electron conductivity (Spitzer 1962, Braginskii 1965) of about 10^6 erg cm^{-2} s^{-1}. This value roughly corresponds to the total radiative emission by the transition region and is about one order of magnitude larger than the total coronal radiative emission.

The transition region UV and EUV emission varies considerably from one point to another on the quiet solar disk, and increases strongly in active regions where it also displays transient behavior characterized as microflaring. The line intensity from different solar features may differ by orders of magnitude. However, the shape of the emission measure curves obtained from the semiempirical fits remains qualitatively similar. In the present paper we compare the Lyman emissions in these different features with our calculations and show how the models can explain the observations.

The thermal coupling between the low transition region and the corona is of great importance to both regions because the transition region may not only receive most of its radiated energy from the corona but may also be a sufficient energy sink to dominate the coronal energy balance. This thermal coupling could only be reduced by a transverse magnetic field, or by a very large amount of some type of plasma turbulence. However, the thermal coupling along the magnetic field would not be inhibited by the field, and the levels of plasma turbulence necessary to substantially decrease the relevant collision mean free paths are very difficult to sustain except possibly in solar flares.

The early estimates of the optically thin radiative losses by Cox and Tucker 1969 (hereafter CT) and the improved calculations by Raymond 1978 (see Rosner et al. 1978) and by Gaetz

and Salpeter 1983 using methods similar to those used for the emission measure analysis, concluded that the radiative losses can be expressed as

$$q_R = \Phi(T) n_e n_H, \tag{2}$$

where Φ (in erg cm^3 s^{-1}) is a function of T only which peaks slightly above T_a. Here n_e is the electron density and n_H is the total hydrogen density (atoms plus protons). When this expression for q_R is used in model calculations based on hydrostatic equilibrium, q_R is found to have a maximum at a temperature of about 18,000 K due to Lyα line emission. Such large radiative losses at low temperatures, given the $T^{5/2}$ dependence of the Spitzer thermal conductivity, led to a major difficulty for the early energy balance models.

The difficulty with the early models is that although the conductive heat flux in the upper transition region is large enough ($\sim 10^6$ erg cm^{-2} s^{-1} at T_a) to explain the emission from the whole transition region, this conductive heat flux (according to the early interpretation of the emission measure curves) decreases to a value of order 10^2 at $T \simeq 30{,}000$ K. As a result, the conductive heat flux in the low transition region cannot account for the large radiative losses in this region. Also the radiative losses in the upper transition region are too small to be consistent with the large decrease in the conductive heat flux throughout this region.

As mentioned earlier, Lyα provides the largest single amount of line emission in the solar transition region. It carries a significant fraction of the total emission from the entire transition region, and the line is not optically thin. McClymont and Canfield 1983, using a probabilistic approach, have attempted to improve the estimates of the radiative losses by considering optical thickness effects. These probabilistic calculations do not accurately describe the photon diffusion process which takes place in the layers where the Lyα optical thickness is substantially larger than unity. The probabilistic approach also cannot adequately describe the "backwarming" which occurs due to radiation produced in one layer of the model that is absorbed in another layer. However, Canfield et al. 1983 introduced a further improvement of

this approach which accounts for some of these effects provided that suitable coefficients are calculated by accurate methods.

Lyα observations have been extensively studied by several authors using high resolution data from OSO-8 (e.g. Lemaire et al. 1981), and from the UVSP instrument aboard SMM (Fontenla, Reichmann, and Tandberg-Hanssen 1988). In recent years, however, only the paper by Vernazza, Avrett, and Loeser 1981 (hereafter VAL) and our Paper I (Fontenla, Avrett, and Loeser 1990) have addressed the detailed modeling of such emission.

The VAL paper presents a set of models for the full range of quiet-Sun EUV observations from dark cell areas to very bright network regions. These models assume hydrostatic equilibrium and are defined basically by the temperature *vs.* height distributions which are chosen to match the observed line and continuum intensities. These models were not intended to satisfy any prescribed energy balance constraint. The VAL model calculations also were based on the assumption of *local* statistical equilibrium. We found in Paper I that important nonlocal effects in the lower transition region are caused by ambipolar diffusion: in a partially ionized gas with large temperature and ionization gradients, atoms diffuse into the hotter, more ionized region while ions diffuse into the cooler, less ionized region. The VAL models include a temperature plateau just above 20,000 K to provide enough material at this temperature to produce the observed Lyα radiation, assuming local statistical equilibrium. Such a semiempirically-determined region having a small temperature gradient is difficult to understand theoretically since thermal conduction is ruled out, and a highly localized energy deposition mechanism would be required to deposit $\simeq 0.1$ erg cm^{-3} s^{-1} in a layer about 20 km thick to give the observed quiet-Sun Lyα emission of $\simeq 2 \times 10^5$ erg cm^{-2} s^{-1}. This energy deposition corresponds to a rate per unit mass of $\simeq 2 \times 10^{12}$ erg g^{-1} s^{-1} and implies a characteristic radiative thermal relaxation time of less than 1 s. This last value is the smallest in the entire upper solar atmosphere and can only be compared to that in the photospheric layers in which the bulk of the solar radiation originates (see Fontenla, Emslie, and Moore 1990). The problem becomes even more severe for bright areas of the network or for active regions.

Our energy balance models properly include hydrogen diffusion, expressed as ambipolar diffusion, i.e., the diffusion of atoms relative to protons. Diffusion occurs naturally in the steep temperature gradient of the transition region because of both the temperature gradient and the temperature-induced concentration gradient of the ions and neutral atoms. The phenomenon of particle diffusion is easily understood and is closely related to thermal conduction. Our energy balance models that include diffusion (and no plateau) give similar Lyα emission to that of the VAL semiempirical models (which have a plateau) because diffusion extends the region of Lyα line formation to higher temperatures. This extension to higher temperatures strongly enhances the collisional excitation rate and makes possible the emission of Lyα photons in a thin layer which covers a much wider temperature range than before.

In Paper I we developed the method and theory on which our present calculations are based and showed that including hydrogen diffusion in both the statistical equilibrium and the energy balance equations yields reasonable hydrogen emission from the lower transition region. This emission is comparable to (although somewhat smaller than) the observed value in the average quiet Sun. These calculations show that if one properly considers hydrogen diffusion one can explain roughly the observed intensities of the Lyman lines without having to resort to *ad hoc* localized energy dissipation mechanisms.

In the present paper, we explore how an increase in the energy input from the corona leads to a higher transition region pressure, assuming hydrostatic equilibrium. We construct models which roughly correspond to the following different solar features: faint cell-center areas, average intensity areas, bright network regions, and plage areas. We leave for a subsequent paper the detailed adjustment of the models to match the observed line and continuum profiles as closely as possible. Instead, in the present paper we study how the changes in the energy input affect the physical processes, the general properties of the models, and the magnitudes of the different hydrogen emissions.

In Paper I we emphasized the method of calculation rather than the physical properties of the resulting models. Also in Paper I we assumed a model atom consisting of only four

bound levels and continuum. In the present paper we improve the calculations by using an eight-level model atom, and we intercompare the properties of four atmospheric models. We also include in our present calculations a detailed treatment of helium, including diffusion, but we defer to a later paper the details of the helium populations and emissions. Our models correspond to the main features observed in the Sun and we compare the Lyman line and continuum intensities computed from our models with observed data. We also show the line asymmetries that result from the diffusion process alone, since in our present hydrostatic models no mass flow is considered. Our objective here is threefold: first, we analyze the physical characteristics of the models and relate them to the available observations; second, we discuss the physical constraints that determine our hydrostatic energy-balance models; third, we obtain some relations between the different physical parameters and the emitted intensities.

With regard to the properties of the models, it is of interest to compare the calculated emission not only with the observations, but also with that derived from "emission measure" calculations for the same temperature structure. Also we show the extent to which optically thin hydrogen radiative cooling functions (e.g., from CT) agree with the actual losses that we compute in detail, and we study the changes that can be made in such functions in order to improve this agreement. We also study how the Lyman lines and Lyman continuum are formed in order to understand the "backwarming" process that irradiates the chromosphere in some cases.

We determine the energy input necessary to support the radiative losses in our hydrostatic models. This energy input is related to the pressure of the transition region. The relationship between these quantities is of great importance for the calculation of coronal loop models, since it determines whether a stationary energy balance can result for different coronal heating rates, and the maximum temperature that the corona will reach. Our calculations yield a basic boundary condition which is essential for these coronal loop models.

We leave for a subsequent paper the problem of considering models with the additional effect of mass flow velocity in the statistical equilibrium and energy balance calculations. This

problem is a very important one since we expect substantial changes to be produced where mass velocities are present. In fact, the observations indicate that such mass motions often occur, and they correspond sometimes to blueshifts while at other times to redshifts. The fast rate of radiative cooling in the lower transition region (with a time scale of about 1 s) indicates that, although a purely stationary model with mass motion is not realistic, quasi-stationary conditions are likely to occur in many cases. Such quasi-stationary conditions would practically satisfy the steady state constraints throughout the transition region, but the physical conditions outside the range of our calculations gradually change so that our boundary conditions would evolve in time. The condition for quasi-stationary models is that the rate of variation of the boundary conditions must be small enough to allow reaching a state close to the energy and excitation/ionization balance in the region we compute. We estimate that the characteristic times for reaching the excitation/ionization balance are similar to the radiative cooling times; then quasi-stationary conditions prevail for changes occurring on time scales of several minutes. However, even in this quasi-stationary regime, it is not simple to find the detailed structure of the lower transition region in cases with mass flows.

2. The Modeling and the Boundary Conditions

Our models of the transition region are basically determined by the choice of boundary conditions. In Paper I we showed that it is sufficient to specify only the density, temperature, and temperature gradient at the lower boundary of the transition region. In the present section we discuss the boundary conditions in further detail because of their crucial importance.

First, note that the transport coefficients we use are not arbitrary or emipirically determined but are fixed by the basic atomic processes and are represented by analytical fits to available data as explained in Paper I. The heat conduction coefficient λ was computed taking into account all the significant species (electrons, protons, and hydrogen atoms) and the collisions between them. In practice, the value of λ is dominated by the electrons except in the

chromosphere where the electron density drops well below the density of neutral atoms. The ambipolar diffusion velocity is given by

$$V_A = D_X \frac{dlnX}{dz} + D_T \frac{dlnT}{dz}, \tag{3}$$

where $X = n_p/n_a$ is the degree of ionization, and D_X and D_T are the diffusion coefficients

$$D_X = 90.7 \frac{T^{1.76}}{p_x} \tag{4}$$

and

$$D_T = 64.1 \frac{T^{1.76}}{p_x} \left[\frac{X + 2.57 - (4000)/(TX^{0.5})}{X + (0.02)/X} \right] \tag{5}$$

where $p_x = (n_a + 2n_p)kT$.

Using the theory explained in Paper I, the total particle heat flux for the hydrostatic models is given by

$$F_H = -\lambda \frac{dlnT}{dz} - V_a \sum_l E_l n_l, \tag{6}$$

where λ is the thermal conduction coefficient, E_l is the energy difference between level l and the continuum, and n_l is the level population. The diffusion velocity V_a for atoms is given by

$$V_a = \frac{n_p}{n_H} V_A, \tag{7}$$

where $n_H = n_a + n_p$ is the total hydrogen density.

The only semiempirically-derived parameters in our calculations are the turbulent velocity and the mechanical energy dissipation. These parameters are, however, of minor importance for our present models. The turbulent velocity that we adopt is shown in Figure 1 as a function of total hydrogen density. This curve represents observed nonthermal broadening velocities derived from line widths. We use this function in all the models in the present paper for computing the frequency and height dependence of the line opacity; also we include these values in the hydrostatic equilibrium equation to obtain a turbulent pressure contribution as described by VAL. The mechanical energy dissipation we consider is small compared to the

radiative losses throughout most of the low transition region, and has a significant effect only near the lower boundary of our computed transition region. The mechanical dissipation we consider is a constant times the total hydrogen density

$$q_M = C_q n_H, \tag{8}$$

as explained in Paper I. The constant C_q was set to zero for two of our models (A and C). The value of this constant for the other models (F and P) was chosen to ensure a smooth change in the slope of the temperature increase. All the chosen values of C_q are shown in Table 1.

Our energy equation balances the radiative losses with the total particle heat flux and the mechanical energy dissipation, and is expressed in the integral form

$$F_H(z) + F_R(z) - F_M(z) = F_H(Z_0), \tag{9}$$

where

$$F_R(z) = \int_{Z_0}^{z} q_R dz \tag{10}$$

and

$$F_M(z) = \int_{Z_0}^{z} q_M dz, \tag{11}$$

and where the height Z_0 is the lower boundary point of our energy balance calculation. This height corresponds to the top of the chromosphere.

We consider all the heights below Z_0 in the chromosphere and photosphere for the solution of the radiative transfer and statistical equilibrium equations, but below the height Z_0 we adopt a given temperature structure. We could determine the temperature distribution below Z_0 such that $q_R = q_M$ where q_M is a given mechanical heating function that leads to a chromospheric temperature distribution consistent with observations (see Anderson and Athay 1989). However, in this paper we take the simpler approach of adopting the VAL chromospheric temperature distribution below Z_0. It is implicit in our calculations that the amount of local mechanical heating is small in the transition region above Z_0 compared with the particle heat flux carrying energy from the corona.

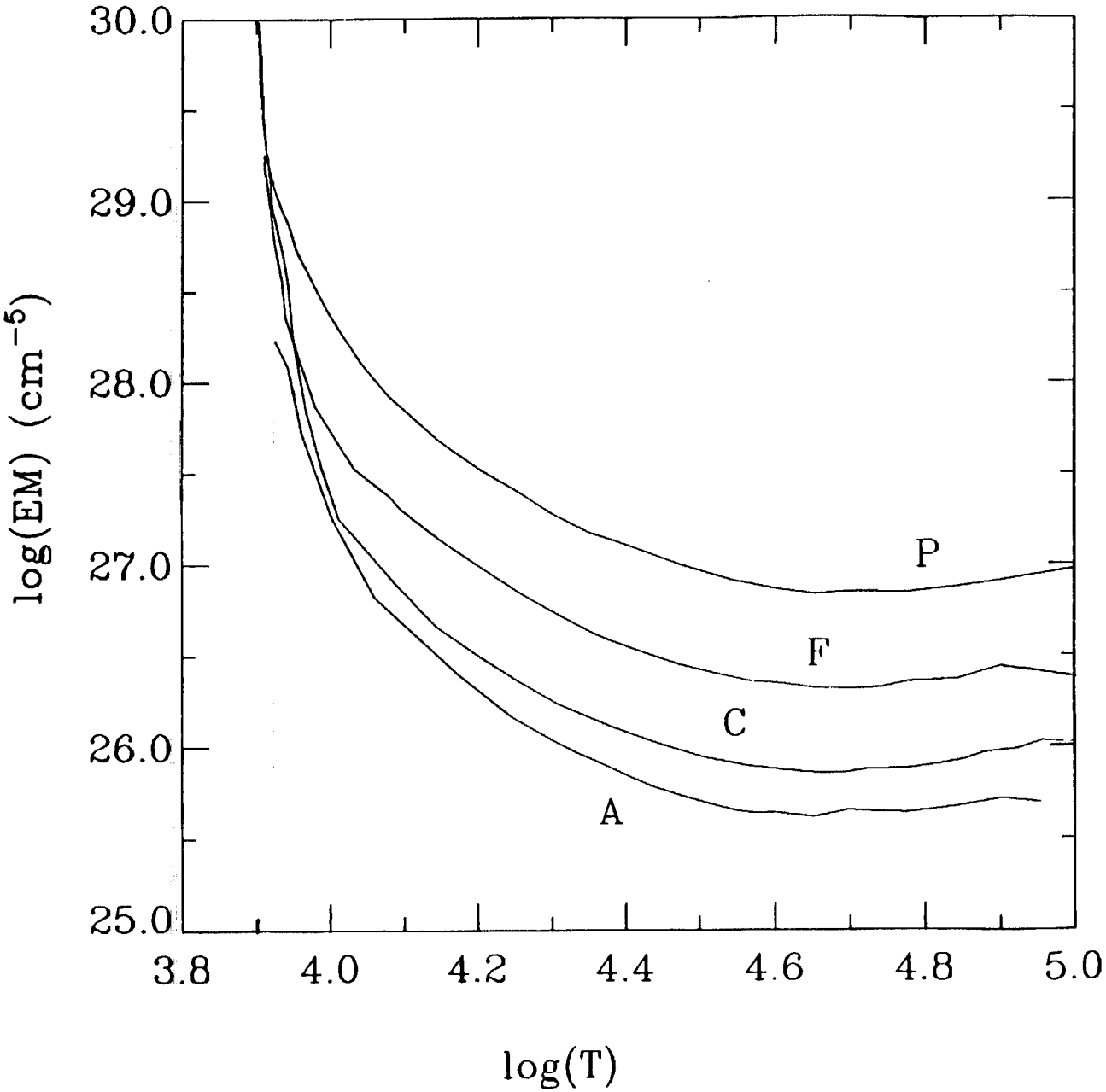
30.0
29.0
28.0
27.0
26.0
25.0
log(EM) (cm^{-5})
3.8
4.0
4.2
4.4
4.6
4.8
5.0
log(T)
P
F
C
A

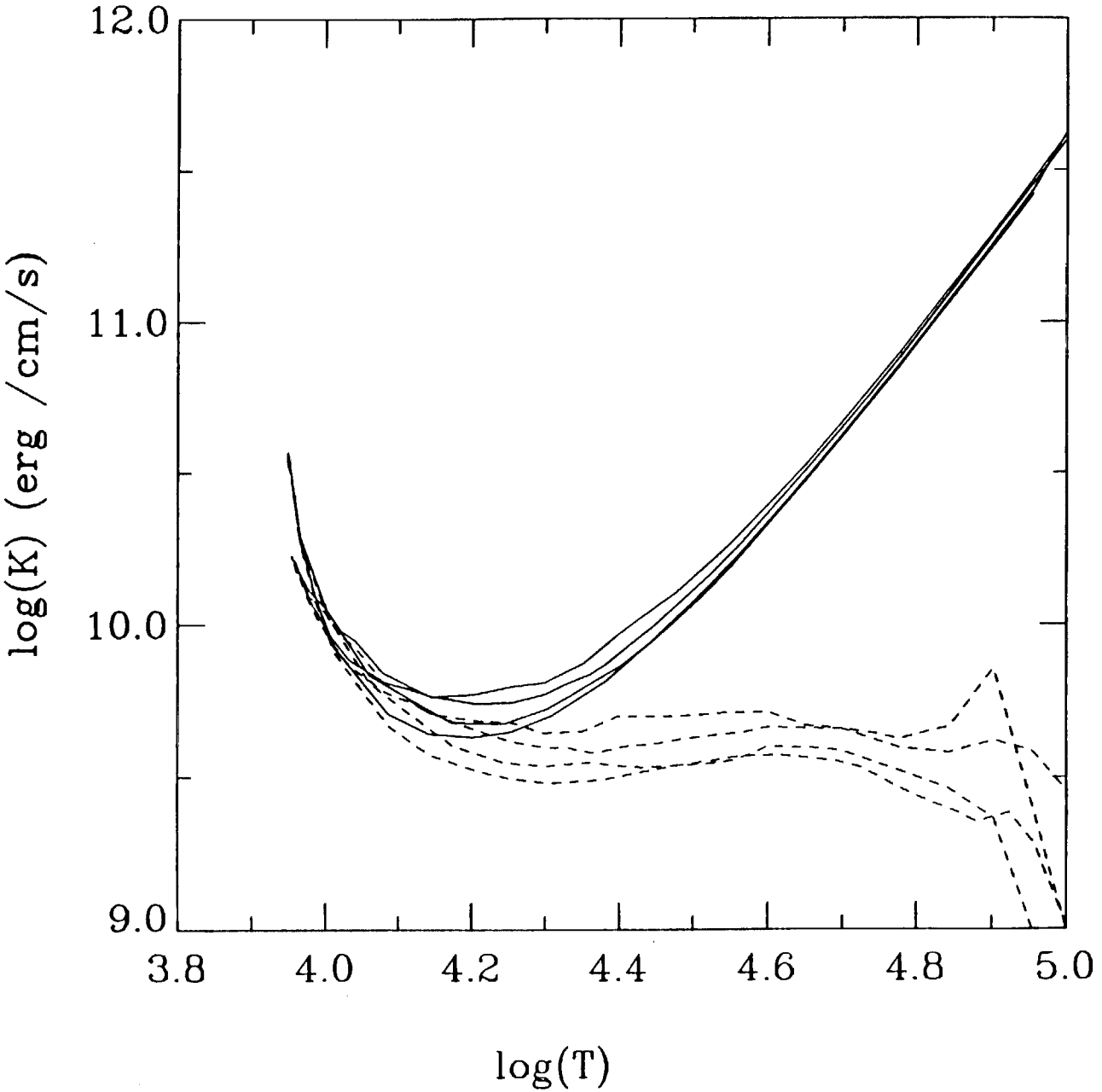
12.0
11.0
10.0
9.0
3.8
4.0
4.2
4.4
4.6
4.8
5.0
log(K) (erg /cm/s)
log(T)

Fig. 8

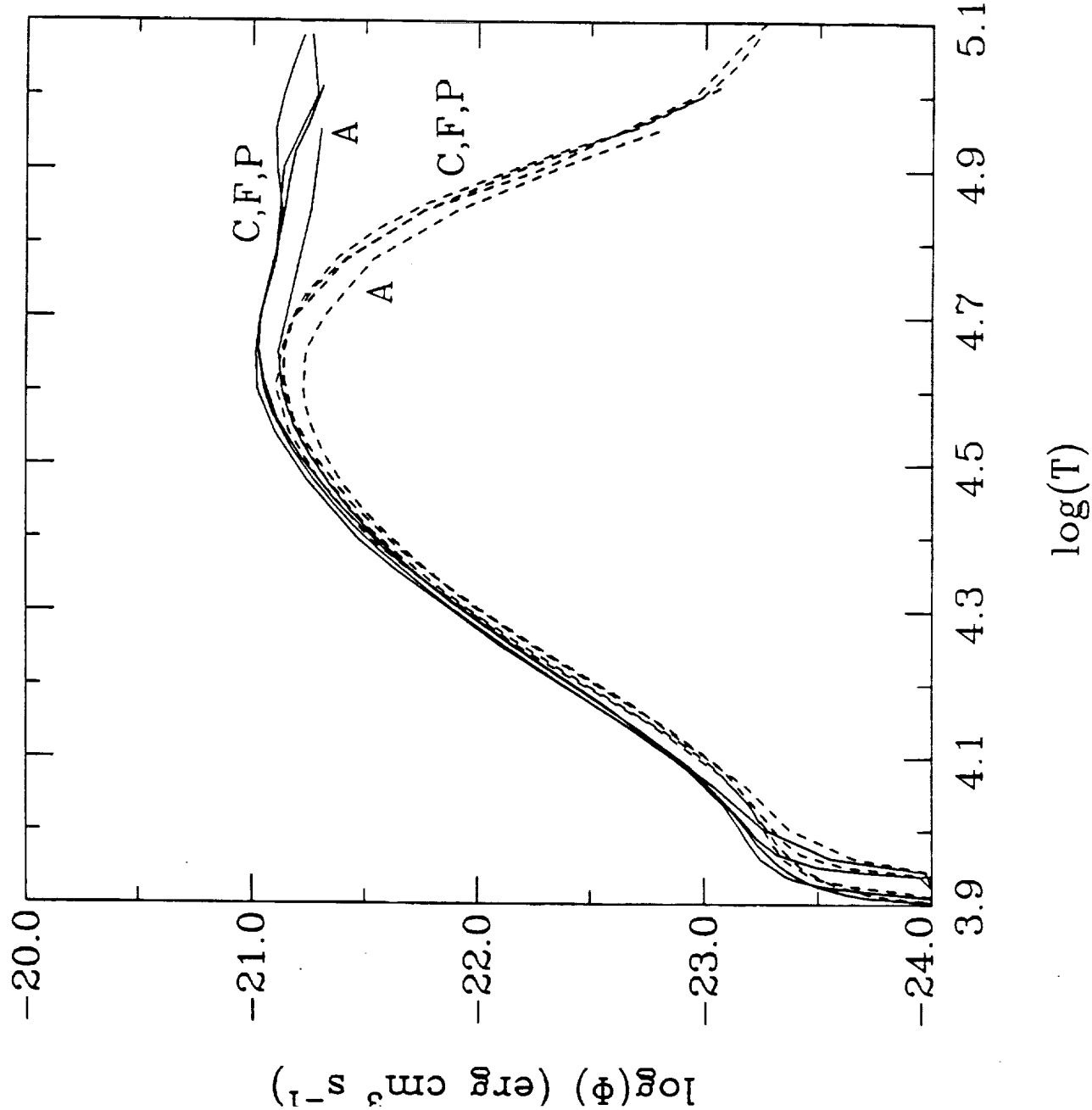
C,F,P
A
C,F,P
A
−20.0
−21.0
−22.0
−23.0
−24.0
3.9
4.1
4.3
4.5
4.7
4.9
5.1
log(T)
log(Φ) (erg cm^3 s^{-1})

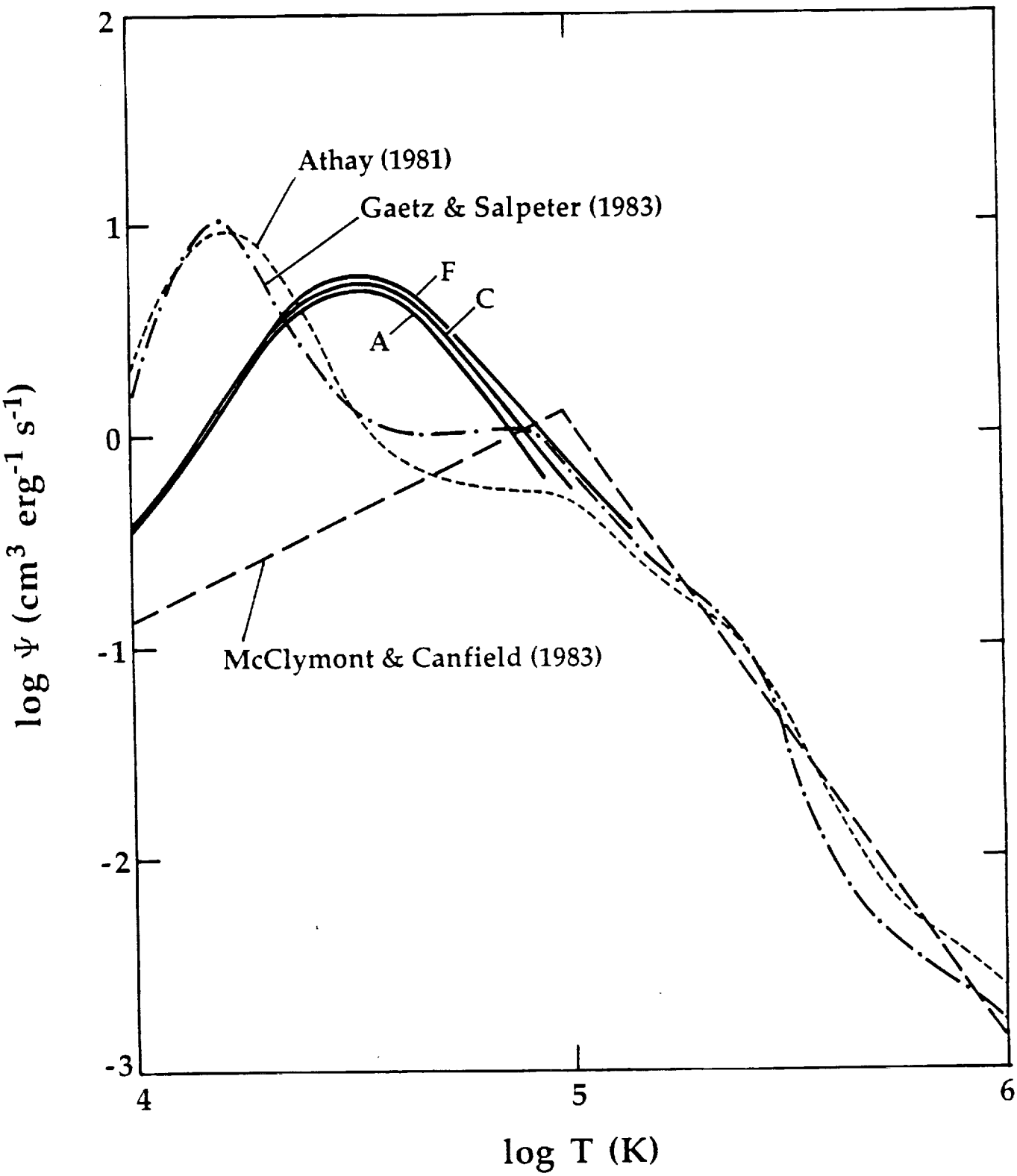
Athay (1981)
Gaetz & Salpeter (1983)
F
C
A
McClymont & Canfield (1983)
2
1
0
-1
-2
-3
4
5
6
log Ψ (cm³ erg⁻¹ s⁻¹)
log T (K)

Fig. 10

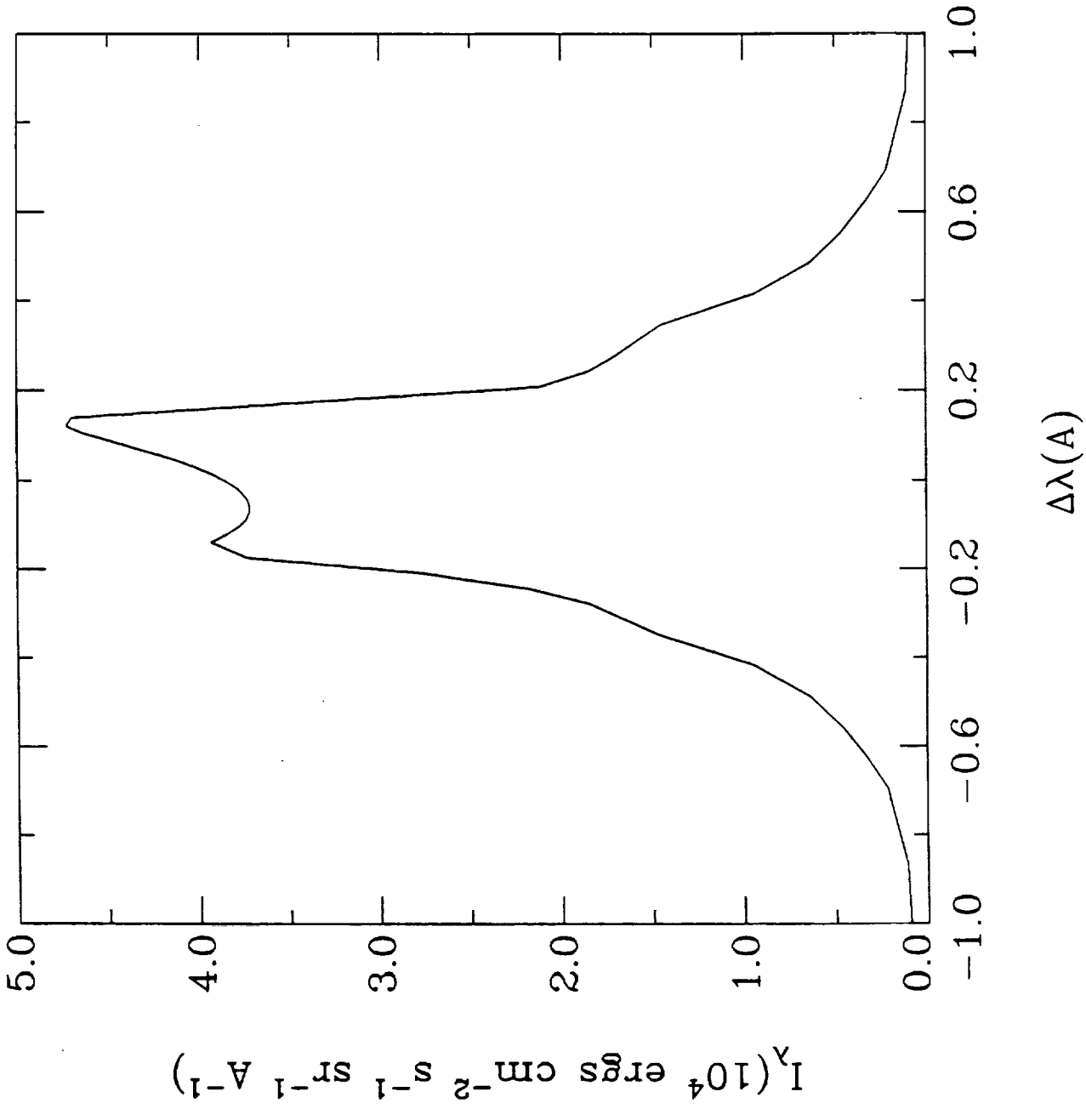

Fig. 11

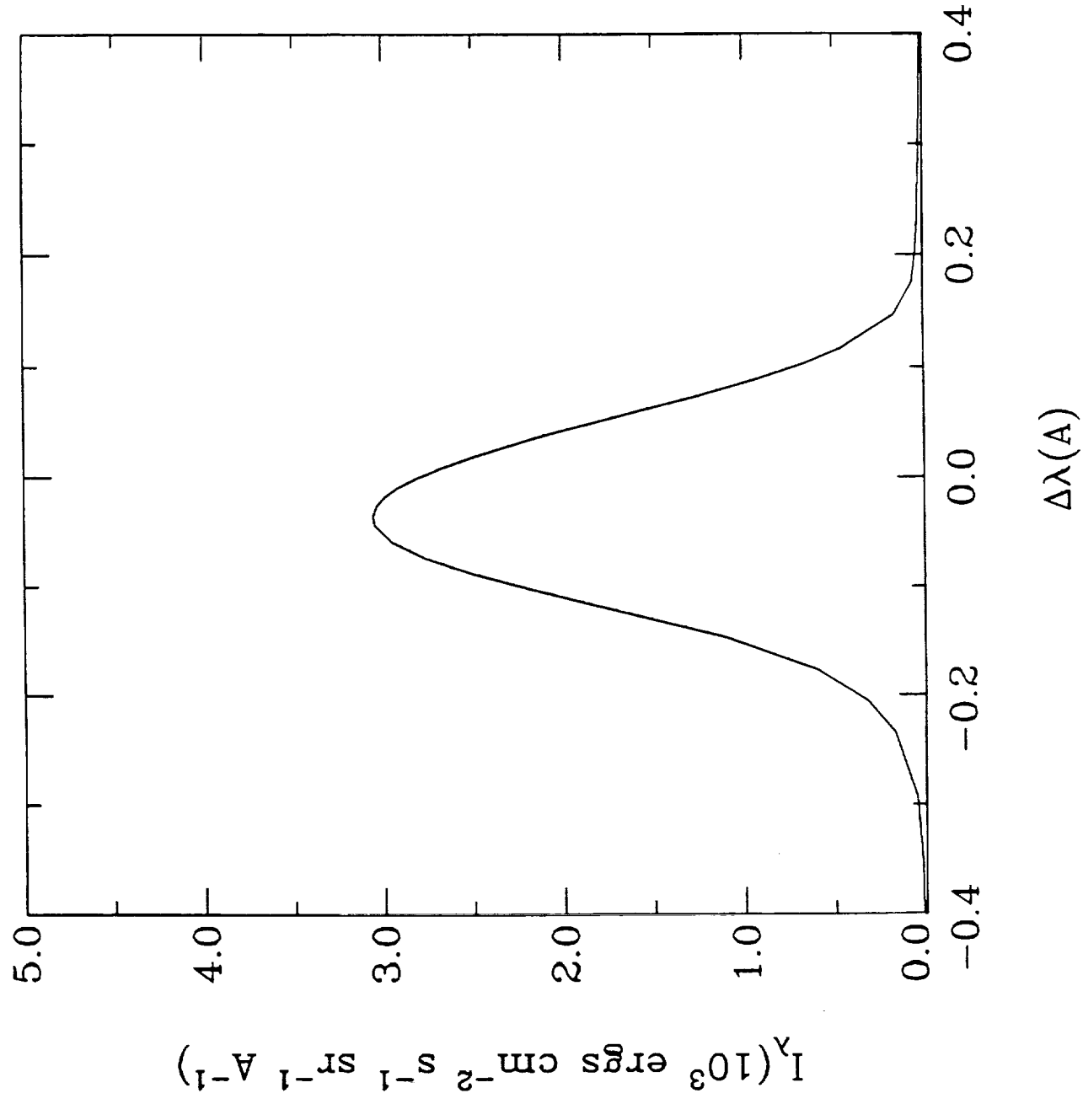

Some problems arise, however, in the lowest layers of the transition region calculations because there is no sharp separation between the two energy balance regimes, viz. where energy downflow or local mechanical heating dominates. This sometimes forces us to modify the energy balance or to manually alter the temperature structure in the layers at temperatures between 8,000 K and 10,000 K. There is relatively little mechanical heating in these layers and their characteristic cooling/heating time is longer than $10^2 - 10^3$ s, far longer than at higher temperatures in the transition region. In the present paper we have not attempted to modify the calculated structure of these upper chromospheric layers because this region has little effect on the results presented here.

The treatment of boundary conditions is one of the main differences between astrophysical and laboratory modeling. In almost all laboratory problems, well-defined geometrical constraints are imposed, such as on the dimensions of the experiment or on the nature of the physical boundaries of the fluid to be modeled. Thus in convective energy transport one sets up rigid walls which are either isolating or highly thermally conducting, and hence imposes either a null heat flux or constant temperature. In modeling the thermal structure of a conducting medium between a heat source and a sink, one deals with a second order equation in which the temperature is held fixed at both boundary locations.

This contrasts with the modeling of the thermal structure of stellar atmospheres where one deals with an intrinsically open system in which the temperature at any given location is not given *a priori*. In the case of the solar atmosphere, however, observational constraints provide a basis for experimenting with different boundary conditions and selecting the models which can describe the observed features. Using this approach, our selection of the lower boundary conditions of the transition region is guided by the observations of chromospheric features. For the purpose of this paper, however, we only look for approximate agreement and we leave detailed fitting for a later paper.

The usual method for computing the equilibrium thermal structure of a stellar atmosphere is to require that the total flux of energy through the atmosphere be constant with depth. In

this procedure one replaces the second order differential equation which describes the energy balance by a first order equation stating that the total energy flux is constant and equal to a prescribed value F_E. Our procedure based on equation (9) is the same, except that we consider only the radiation flux that affects the transition region and we include the conductive and ionization-energy heat flux. Effectively we can let $F_H(Z_0) = F_E$ in equation (9) so that

$$F_E = F_H(z) + F_R(z) - F_M(z). \tag{12}$$

The total particle heat flux can be written in the form

$$F_H = K(z)\frac{dT}{dz} \tag{13}$$

where K is a depth-dependent coefficient which does not have an analytical expression, but depends on the level populations. This equation is integrated from the lower boundary Z_0 at which the temperature is specified, and because of the highly nonlinear character of the problem we perform iterations as explained in Paper I until convergence is achieved.

In our models the energy flux F_R includes only the radiative flux created in the transition region, in the hydrogen lines and continua, in the helium lines and continua, and in other transitions considered by CT. As a consequence of our assumptions the value of F_E is close to zero and is exactly equal to the residual heat flux $F_H(Z_0)$ as noted above. This residual heat flux is small compared to the total heat flux $F_H(Z_1)$ at the upper boundary which is the source of the radiative losses apart from the small contribution of mechanical energy dissipation. However, in our models $F_H(Z_0)$ is not strictly zero because we find that some small temperature and ionization gradients persist at the lower transition region boundary. Since we keep the structure of the chromosphere fixed in this paper, the temperature gradient at the top of the chromosphere is also fixed. We compute $F_H(Z_0)$ from this temperature gradient and from the ionization gradient obtained in the previous iteration. Thus our actual constraint is not the value of F_E but the temperature and its gradient at the top of the chromosphere. For reference we give in Table 1 the resulting values of $F_E = F_H(Z_0)$ for our computed models.

In Table 2 we give the values of the parameters that we obtain at the upper boundary (Z_1) of our computed models.

In the present paper we obtain models for four typical solar features, namely, the network cell center, an average area, the bright network, and a plage. We adopt as a boundary condition for all models a temperature close to 8000 K which occurs at different heights Z_0 in the different models. This choice is arbitrary, but is a representative value for the chromospheric temperature just below the transition region.

The temperature structure of the photospheres and chromospheres of the different models were determined semiempirically from observed continuum and line intensities (see VAL). We use the revised versions of the VAL models A, C, and F given by Avrett 1985 and Maltby et al. 1986. The chromospheric temperature distribution for model P is essentially that of Shine and Linsky 1974 and Lemaire et al. 1981. The most significant differences between our transition region models are not due to the boundary values of the temperature and the temperature gradient at height Z_0, but rather to the pressure at this height and throughout the transition region. Since the chromospheric pressure decreases with height, with a characteristic scale height of about 300 km, the pressure at Z_0 and throughout the transition region is increased when Z_0 is changed to a lower height (provided the photospheric values remain the same).

The reason we do not specify boundary conditions at the top of the transition region, i.e., at Z_1, is that it would be difficult specify *a priori* the value of $F_H(Z_1)$ consistent with a reasonable, physically meaningful model. If one chooses the values at the upper boundary, F_E would correspond to the small difference between the large downward total heat flux $F_H(Z_1)$ and the large outward total radiative flux $F_R(Z_1)$. Integrating the energy balance equation downward also requires some initial ionization and excitation structure (necessary in this nonlinear problem), so that inappropriate initial conditions would produce an unreasonable temperature or temperature gradient at the chromospheric boundary. We do not consider such results meaningful for the solar atmosphere, and there would be no effective way of avoiding these

difficulties because small changes in the conductive/diffusive heat flow would produce large and unpredictable changes in the behavior at the lower boundary.

We recognize that there is some arbitrariness in our models due to the adopted temperature gradient at the top of the chromosphere. Changing this gradient slightly shifts the start of the steep gradient of the transition region. Nevertheless, such small changes only result in changes in the whole model which are small compared with observational uncertainties.

We note that our present models do not extend to temperatures above 10^5 K. The reason for this is that our detailed calculations may not adequately account for the radiative losses of the highly ionized species which dominate in this region. We approximate the radiative losses due to elements other than hydrogen and helium by using the CT optically thin calculations. However, we strongly suspect that the effects of diffusion will change the ionization balance of many elements and hence their radiative losses, as we have found for both hydrogen and helium. Thus, we believe that our present models are not accurate outside the range in which hydrogen and helium dominate the radiative losses.

3. The Structure of the Models

Four models were computed which, in order of increasing UV emission, correspond to a faint area within a network cell (A), an average-intensity quiet Sun area (C), a bright area of the network (F), and a plage region (P). The models include the photospheric layers in which the temperature decreases outwards (i.e. decreases with decreasing column mass). A minimum temperature is reached at a height of around 500 km above the $\tau_{5000} = 1$ level (column mass $\simeq 0.05$ g cm^{-2}). Then the temperature rises rapidly up to a chromospheric plateau where the temperature gradually increases with height over a distance of about 1500 km. The temperatures of the chromospheric plateau are different for the various models. The change in the column mass of the chromosphere in the various models is mainly due to the increase of temperature for the brighter models, which increases the density scale height and

allows higher densities in the chromosphere. In the transition region above the chromosphere, the temperature rises steeply up to coronal values ($\sim 10^6$ K). Our models, however, only extend up to temperatures around 10^5 K because our present computations are not accurate above this point. The column mass (and hence the pressure) remains almost the same throughout the transition region because of its small extent (see below), and its value represents the amount of material in the corona above. Since the scale height at coronal temperatures is around 50,000 km, almost all the coronal mass lies within a distance of 100,000 km above the transition region. This is consistent with coronal loops of the kind proposed by Rosner, Tucker and Vaiana 1978, or with open field lines.

As stated earlier, we have simply adopted chromospheric temperature distributions from the semiempirical VAL models and have appended an energy balance transition region to each of them. The four complete models are shown in Figures 2 through 5 on a scale that shows mostly the underlying chromospheric and photospheric layers.

We now discuss the transition regions that are calculated in these four cases. The characteristics of the transition regions are described in Tables 3 through 6 for selected values of temperature. In our models the temperature continues to rise rapidly at the high temperature end of our calculations ($\sim 10^5$ K). However, the maximum slope of $T(z)$ is reached at around 20,000 K, and this slope is smaller at 10^5 K. In Figure 6 we show another way of presenting our transition region models. Here we plot the emission measure as defined by equation (1). However, as we explain later this plot should not be used to estimate the emissions by hydrogen and helium, nor (we believe) to estimate any low transition-region emissions, but this plot can be used to compare our model of the temperature distribution with other models. When comparing with the semiempirical models based on emission measures (Athay 1981) we find that our models reach similar values of EM (see equation (1)) at a temperature of 10^5 K and that these values rise by orders of magnitude at low temperatures, but the rise occurs in our models at lower temperatures than in the previous semiempirical models (i.e. the slope of the temperature *vs.* height remains high in our models of the low transition region). This is not

a deficiency of our theoretical calculations; rather it is a consequence of the fact that in our model the emission measure curve and the usual temperatures of formation are not locally related to the line emission. In our models, the line emission is computed consistently (including diffusion) and should be compared to the observed intensity; this test is more significant than the assumptions usually made in emission-measure semiempirical studies.

An interesting relationship can be obtained from our models. For temperatures close to 10^5 K (near the upper boundary in our calculations), we find from our numerical results that

$$log(F_H(Z_1)) \simeq 5.865 + 0.65log(\frac{T_1}{10^5}) + (1.096 + 0.022log(p_1))log(p_1) \tag{14}$$

(using cgs units) within the range of our calculations ($0.084 < p < 1.43$ dyn cm^{-2}). Using the Spitzer thermal conductivity for these highly ionized layers, we obtain

$$log(\nabla lnT) \simeq log(F_H) - 11.5 - 3.5log(\frac{T}{10^5}) \tag{15}$$

and, applying the definition of EM (eq. (1)) gives

$$log(EM) \simeq 21.12 + 2log(p) - 2log(\frac{T}{10^5}) - log(\nabla lnT), \tag{16}$$

so that

$$log(EM) \simeq 26.755 + 0.85log(\frac{T}{10^5}) + (0.904 - 0.022log(p))log(p) \tag{17}$$

(in cgs units). This last equation gives the asymptotic behavior of our results for $T \simeq 10^5$ K.

4. The Energy Balance of the Models

Figure 7 shows a plot of K *vs.* temperature where K is the ratio of our total calculated heat flux to the logarithmic temperature gradient

$$K = \frac{F_H}{\nabla lnT}. \tag{18}$$

The dashed curves give the contribution due to the ionization energy flow alone. For most of the transition region the ionization energy flow is smaller than the conductive flow because of the high ionization degree. But at temperatures below 20,000 K the ionization energy flow dominates, and this is true down to the chromospheric layers. The curves for the four different models shown in Figure 7 practically overlap for temperatures higher than 30,000 K. The differences between the different models, in this range, are only due to the variations in the Coulomb logarithm. For the lower temperatures larger differences are found due to the change in the ionization energy transport. However, these differences are not larger than a factor 1.4 over the entire range of the models. This indicates that it is possible to define an "effective thermal conductivity" which includes the thermal conductivity and the ionization energy transport ("reactive conductivity"). This approach of Devoto 1968 was used by Nowak and Ulmschneider 1972 (hereafter NU) for solar cases. Our effective conductivity coefficient K shown in Figure 7 is about the same as that of NU at about 10,000 K, is below the NU values by a factor in the range 1-2 at 30,000 K, and is about one order of magnitude larger than the NU values at 8,000 K. These differences are mainly due to the different degree of ionization and the ionization gradient assumed by NU compared with the values in our detailed calculations.

In Figure 8 we show the total radiative loss function

$$\Phi = \frac{q_R}{n_e n_h}, \tag{19}$$

computed from our models. The dashed curves give the contribution due to hydrogen emission alone. Our total radiative losses include hydrogen and helium emission computed in detail and the optically thin contributions for the heavier elements according to CT. Again, the curves for the different models practically overlap and there is only a residual variation of less than a factor 1.4, except at temperatures below 10,000 K. At the lowest temperatures shown in Figure 8, large variations arise between the models, and the hydrogen losses may even become negative for models A and C. These negative losses by hydrogen are assumed to be compensated by the losses due to other elements. We note that at the higher temperatures

our curves are basically the same as the CT optically thin ones because hydrogen and helium do not contribute significantly to the total losses. However, at low temperatures our results are substantially different from the CT values. For temperatures between 20,000 and 100,000 K our values are larger than those of CT, and for temperatures below 20,000 K our values are smaller. These differences suppress the local minimum around 20,000 K shown by CT and other authors. Instead, Figure 8 shows that our radiative loss function increases monotonically, reaching a maximum at around 40,000 K and then remains almost constant up to 100,000 K. The shift in the maximum and the filling in of the local minimum in the CT curve is due to hydrogen radiation. Another contribution to the elimination of the local minimum is helium radiation, but the helium results will be discussed in a subsequent paper.

In Figure 9 we compare our radiative losses with the optically thin values of Gaetz and Salpeter 1983 and the CT values used by Athay 1981. The quantity $\Psi = q_R/p^2$ is shown as a function of temperature, where p is the pressure in dynes cm^{-2}. As noted earlier, McClymont and Canfield 1983 modified the optically thin radiative loss curve by introducing optical thickness effects. Here we plot our results for models A, C, and F (the model P curve essentially overlaps that of model F) on a figure from Woods, Holzer, and MacGregor 1990.

The reason that negative hydrogen losses occur at the top of the chromosphere in some of our models is that in these layers the Lyman continuum photons which are produced at the base of the transition region produce a downward energy flow which overpowers the upward energy flow in Lyα and Hα. This effect, usually referred to as "backwarming", is non-local and can be accounted for only by solving the radiative transfer equation. The hydrogen backwarming persists down to temperatures around 6,000 and 6,400 K in models A and C, respectively. The effect of the successive increase of chromospheric temperature in models A, C, F, and P is that the downward Lyman continuum radiation flux increases as the temperature increases at the top of the chromosphere, but the increase in the upper chromospheric opacity does not allow this radiation to penetrate as deeply in models F and P as in models A and C. Also, the radiative losses in the Hα line become very important in models F and P. The Lyα line

radiative losses in the chromosphere are positive and comparatively small. This is shown by the following values at the temperature of 7,000 K: the Lyman continuum radiative losses are -1.7×10^{-3} (model A), -2.5×10^{-3} (C) and -6×10^{-4} (F) erg cm^{-3} s^{-1}, while the Lyα losses are 7.4×10^{-4} (A), 8×10^{-4} (C) and 3.9×10^{-4} (F) and the Hα losses are 2.4×10^{-4} (A), 7×10^{-4} (C) and 2.6×10^{-3} (F).

We find that the local hypothesis of "effectively thin" production of radiation does not describe the hydrogen radiative losses in the chromosphere accurately. The important effects of backwarming, photon diffusion, and transition interlocking can only be accounted for by non-local calculations in which the radiative losses at a given height in the atmosphere are related to the photon emission at all other heights, or at least over a range of heights.

5. The Emitted Hydrogen Spectra of the Models

Table 7 shows the emitted fluxes of radiation in the Lyα and Lyβ lines. The values show the large increase in the emissions as the pressure increases. The values in Table 7 can be compared with the heat flux at $T = 10^5$ K from Tables 3 through 6. This comparison shows that a large part of the energy downflow is emitted in these lines. For model A the emitted radiation flux in the Lyman lines is slightly larger than the downward heat flux at 10^5 K. This excess is due to a chromospheric contribution to the emission. As the heat flux and the emission increases in models C, F and P, the hydrogen lines radiate only 65 % of the downward heat flux and the remaining is radiated in the lines of other elements. Moreover, as the energy radiated increases in our models, the Lyβ flux increases relative to Lyα: Lyβ is 2.5, 2.9, 3.3, and 3.9 % of Lyα for models A, C, F, and P, respectively.

Tables 8 and 9 show the emitted intensities resulting from our models at two different viewing angles θ ($\mu = \cos\theta$). Comparing with the observed integrated intensities for the dark and bright features (Vernazza and Reeves 1978) we find that our computed the Lyα values are

too small by a factor of about 2 and that our computed Lyβ intensities are too large by about the same factor.

Comparing the computed Lyα line profiles with observations (Fontenla, Reichmann, and Tandberg-Hanssen 1988), we find that the line profiles we obtain resemble the observed ones. The present computed line profiles have a much higher central intensity than those determined from the VAL models, in better agreement with the observations. However, the entire profile is about a factor of 2 too faint as noted above. Also, the computed separation between the Lyα blue and red peaks is somewhat narrower than the observed. Consequently we believe that some modifications to our models are needed in order to accurately reproduce the Lyman line profiles in various solar features. These modifications are not important for the present discussion and will be treated in a subsequent paper.

Comparing the intensities listed in Table 8 and the downward heat flux F_H at 10^5 K, we find the following approximate relations between the integrated line intensities and the heat flux

$$I_{Ly\beta} = 2.6 \times 10^3 \left(\frac{I_{Ly\alpha}}{10^5}\right)^{1.16} \tag{19}$$

and

$$F_H(T = 10^5) = 4.5 \times 10^5 \left(\frac{I_{Ly\alpha}}{10^5}\right)^{1.2} \tag{20}$$

which hold for the range of models we computed. These relations, together with those in equations (14) through (16) can be used as diagnostics in hydrostatic cases.

The comparison of Tables 8 and 9 gives information about the limb darkening/brightening from our models. The Lyα line center and peak intensities both decrease slightly toward the limb, but the integrated intensity increases slightly at the limb. This behavior of the integrated intensity is due to the slight increase in the line width, which overpowers the decreasing monochromatic line intensity. In contrast, the Lyβ line shows the limb brightening characteristic of a much thinner line; the integrated and line center intensities increase by factors of

about 2 and 1.8 between disk center ($\mu = 1$) and limb ($\mu = 0.3$), respectively. The center-to-limb variations of the Lyα and Lyβ intensities from our models are basically consistent with observations.

In the following we will explain how our model calculations, in contrast to the usual emission measure approach, can explain the Lyα emission of the Sun. We note that chromospheric layers have a significant contribution to the Lyα wing emission, and that these layers are illuminated by the radiation produced in the transition region. Thus the arguments which follow do not apply to the chromospheric layers. If one considers the usual effectively thin approach, the line intensity can be expressed by

$$I_{Ly\alpha} = \int h\nu n_1 n_e C_{12} dz, \tag{21}$$

where h is Planck's constant, ν is the line frequency, and C_{12} is the collisional excitation rate coefficient. This coefficient can be approximated by the expression

$$C_{12} = C_0 \gamma T^{-1/2} e^{-\frac{h\nu}{kT}}, \tag{22}$$

where C_0 is the constant 4.3×10^{-6} while $\gamma \simeq 0.7$ at 10,000 K and $\simeq 1.0$ at 40,000 K; see Scholz et al. 1990. Equation (21) can be modified by introducing the degree of ionization $X = n_p/n_1$, and becomes

$$I_{Ly\alpha} = \int h\nu n_H n_e \frac{C_{12}}{1+X} dz, \tag{23}$$

which leads to the usual expression

$$I_{Ly\alpha} = \int h\nu EM \frac{C_{12}}{1+X} dlnT \simeq h\nu EM \frac{C_{12}}{1+X} \Delta lnT, \tag{24}$$

When these expressions are applied under the assumption of local ionization, it is found that the Lyα line core forms at around 20,000 K because for lower temperatures the collisional rate decreases sharply and for higher temperatures hydrogen becomes highly ionized. However, the situation becomes very different when ambipolar diffusion is considered and non-local effects arise. In this case, our models yield an ionization degree $X \simeq 10$ at 20,000 K and $X \simeq 30$

at 40,000 K. Thus the Lyα line center forms at a temperature of about 40,000 K, well above that in the local ionization models. This has important consequences for the emission because the collisional rate at 40,000 K, $C_{12} = 1.1 \times 10^{-9}$ s^{-1}, is much higher than that at 20,000 K, $C_{12} = 6.5 \times 10^{-11}$ s^{-1}.

We find that if one uses the correct 40,000 K temperature of formation and the range of temperatures $\Delta lnT = 0.4$, as suggested by Figure 8, one obtains the relation between the emitted intensity and the emission measure

$$I_{Ly\alpha} \simeq 2 \times 10^{-22} EM. \tag{25}$$

This combined with the values of EM from Figure 6 explains the large increase in the line center emission compared with models assuming local ionization. Also, this emission accounts for a significant fraction (about 1/4 for model C) of the emitted intensity of Lyα in our models. However, this estimate, based on improved optically thin and emission measure approaches, is not very accurate for an optically thick line such as Lyα in which the total emission includes not only the contribution from a narrow region but also contributions from both hotter and cooler regions and even some contribution from the upper chromosphere.

The Lyman continuum intensity computed from our models is smaller than observed by a factor of about 3. This results from our having appended an energy balance transition region to the VAL models without any modification to the chromospheric structure. In the VAL models, part of the Lyman continuum emission originated in the plateau at 20,000 K. In our new models most the Lyman continuum photons originate in the upper chromosphere. Consequently our computed Lyman continuum intensity is smaller than in the VAL models and does not match the observed. The values of the intensity at the head of the Lyman continuum for our models are 19.9 (model A), 26.1 (C), 55.5 (F), and 172 (P) ergs cm^{-2} s^{-1} sr^{-1}Å^{-1}. The limb brightening at the head of the Lyman continuum (the intensity at $\mu = 0.3$ relative to that at $\mu = 1$) is 1.21 (A), 1.58 (C), and 1.67 (P), indicating that limb brightening can give information on conditions in the chromosphere. The Hα line is not substantially affected by

our transition region and remains similar to that in the VAL models. The line center intensity practically does not change in our models A, C, and F, but it increases for the plage model (P) by about 10 %, in agreement with observations.

Our resulting Lyman line profiles are slightly asymmetric and Doppler shifted. This occurs because, even though the mass velocity is zero in our hydrostatic models, neutral atoms (which are responsible for the Lyman lines) flow upwards with a small height-dependent velocity. As examples we show in Figures 10 and 11 the Lyα and Lyβ disk center profiles computed from model C.

6. Conclusions

We have computed a set of hydrostatic models of the solar atmosphere which are able to explain a number of observations. Our models include an update of the VAL models A, C, and F which correspond to a faint area inside the network cells, an average brightness region, and a bright network element, respectively. In addition we computed model P for a plage area of medium brightness. The photospheric and chromospheric temperature structure for all these models was established by previous semiempirical modeling. Our present models contain chromosphere-corona transition regions which are computed by balancing the radiative losses with the heat downflow from the corona. In the brightest models, F and P, we also included mechanical energy dissipation to obtain a smooth match between the upper chromosphere and the transition region. This mechanical dissipation does not have a great effect in our calculations and is negligible compared to the radiative losses for the regions where the Lyα line forms. The heat downflow is basically carried by electron heat conduction in the upper layers, and diffusive transport of ionization energy in the lower layers of our transition regions. Our calculations take into account the effects of hydrogen and helium diffusion which make our models basically different from all previous ones (except those of our Paper I). The diffusion of hydrogen is characterized by the ambipolar diffusion velocity, i.e., the relative velocity between

the upflowing neutral atoms and the downflowing proton-electron pairs. The ionization energy flow carried by the diffusion of the proton-electron pairs is the dominant energy downflow at temperatures below about 24,000 K where the electron thermal conduction becomes very small. Also, the diffusion affects greatly the ionization balance compared with that computed assuming local statistical equilibrium. This effect corresponds to a smoothing of the ionization gradient and causes the Lyα line to be formed at temperature around 40,000 K instead of around 20,000 K as obtained from local ionization balance. This change, compared with emission-measure, local-ionization calculations, strongly enhances the Lyman line intensities without any *ad hoc* parameters or mechanisms. In our calculations the transport (conductivity and diffusion) coefficients are determined from well-established first-order transport theory by using known collisional cross-sections (which include charge transfer and elastic processes).

In the present hydrostatic models of the transition region, essentially the only free parameter is the pressure at which the transition region occurs. This value controls the amount of emitted radiation and is closely related to the downward energy flow from the corona (see equation 14). The value of the pressure at the transition region corresponds to the mass column density of the corona which increases with increasing brightness of the transition region emission. The variations of pressure of the transition region explain very well the range of the observed Lyman line intensities, and our models give the correct center to limb behavior.

We find several relations between the pressure, the heat flux at $T \simeq 10^5$ K, and the Lyman line intensities. These relations allow us to determine a transition region model from single line observations. We find that while the transition region emission may cover a range of heights, the deeper regions are the brightest. We obtain a characteristic height over which emissions substantially decrease, which is essentially the chromospheric pressure scale height which ranges between 300 and 400 km.

Our calculations show how an "effective thermal conductivity" can be defined which includes electron thermal conduction and the ionization energy diffusive transport. Our results

differ from those of Nowak and Ulmschneider especially at low temperatures, because of the detailed computations of the non-local ionization and ionization gradient we include.

Also we find that it is possible to define a radiative loss function (equation 19) which accurately gives the radiative losses for temperatures above 10,000 K. This function differs from the previous ones in that it increases monotonically for temperatures up to 40,000 K, and then remains almost constant (with only a small decrease) up to temperatures of 100,000 K at the top of our models. This behavior is partially due to the increase in the Lyα line formation temperature. Another factor in the new radiative loss curve is that similar shifts in the line formation temperature occur for the helium lines because of the diffusion of helium atoms and ions. We will describe the helium results in a later paper.

Our calculations open a number of interesting research possibilities, which were suggested in our Paper I. Subsequent papers will describe the helium results and the effects of moderate quasi-stationary mass upflows and downflows. We are also carrying out improved model calculations in which the chromospheric temperatures are adjusted to give better agreement with observations, and to fit the observed Lyman line and continuum intensities and particularly the whole Lyα line profile more accurately.

Much interesting work remains to be done, e.g., in exploring the formation of the lines of other elements such as C and O, including the corresponding diffusion effects, extending the transition region to higher temperatures, exploring the effects of magnetic fields, and investigating the changes in chemical abundances with height that are induced by particle diffusion.

Acknowledgements

This work was supported by the NASA Space Physics Division of the Office of Space Science and Applications. J.M.F. acknowledges support from grant NAGW-2096. E.H.A. and R.L. were supported by grant NSG-7054.

References

Anderson, L.S., and Athay, R.G. 1989. *Ap. J.*, **336**, 1089.

Athay, R.G. 1981, in *The Sun as a Star*, ed. S. Jordan (Washington D.C.: NASA), p. 85.

Athay, R.G. 1988, in *Multiwavelength Astrophysics*, ed. F. Cordova (New York: Cambridge Univ. Press), p. 7.

Avrett, E.H. 1985, in *Chromospheric Diagnostics and Modelling*, ed. B.W. Lites (Sunspot: National Solar Observatory), p. 67.

Braginskii, S.I. 1965, in *Reviews of Plasma Physics*, (New York: M.A. Leontovich Consultants Bureau), p. 205.

Canfield, R.C., Fisher, G.H., and McClymont, A.N. 1983, *Ap. J.*, **265**, 507.

Cox, D.P., and Tucker, W.H. 1969, *Ap. J.*, **157**, 1157 (CT).

Devoto, T.S. 1968, *J. Plasma Phys.*, **2**, 617.

Dupree, A.K. 1972, *Ap. J.*, **178**, 527.

Fontenla, J.M., Avrett, E.H., and Loeser, R. 1990, *Ap. J.*, **355**, 700 (Paper I).

Fontenla, J.M., Emslie, A.G., and Moore, R. 1990, *in Astrophysics in Antarctica*, eds. D.J. Mullan, M.A. Pomerantz, and T. Stanev (New York: American Inst. Phys.), p. 218.

Fontenla, J.M., Reichmann, E.J., and Tandberg-Hanssen, E. 1988, *Ap. J.*, **329**, 464.

Gaetz, T.J., and Salpeter, E.E. 1983, *Ap. J. Suppl.*, **52**, 155.

Lemaire, P., Gouttebroze, P., Vial, J.C., and Artzner, G.E. 1981, *Ap. J.*, **103**, 160.

Maltby, P., Avrett, E.H., Carlsson, M., Kjeldseth-Moe, O., Kurucz, R.L., and Loeser, R. 1986, *Ap. J.*, **306**, 284.

McClymont, A.N., and Canfield, R.C. 1983, *Ap. J.*, **265**, 483.

Mariska, J.T. 1986, *Ann. Rev. Astr. Ap.*, **24**, 23.

Nowak, T., and Ulmschneider, P. 1977, *Astr. Ap.*, **60**, 413 (NU).

Potasch, S.R. 1964, *Space Sci. Rev.*, **3**, 816.

Scholz, T.T., Walters, H.R.J., Burke, P.G., and Scott, M.P. 1990, *Mon. Not. Astr. Soc.*, **242**, 692.

Shine, R.A., and Linsky, J.L. 1974, *Solar Phys.*, **39**, 49.

Spitzer, L. 1962, *Physics of Ionized Gases* (New York: Interscience).

Rosner, R., Tucker, W.H., and Vaiana, G.S. 1978, *Ap. J.*, **220**, 643.

Vernazza, J.E., and Reeves, E.M. 1978, *Ap. J. Suppl.*, **37**, 485.

Vernazza, J.E., Avrett, E.H., and Loeser, R. 1981, *Ap. J. Supp.*, **45**, 635 (VAL).

Withbroe, G. 1981, in *The Sun as a Star*, ed. S. Jordan (Washington D.C.: NASA), p. 321.

Woods, D.T., Holzer, T.E., and MacGregor, K.B. 1990, *Ap. J.*, **355**, 295.

Figure Captions

Fig. 1.- The turbulent velocity as a function of total hydrogen density (in cm^{-3}) adopted in our models.

Fig. 2.- Distribution of temperature in K with column mass in g cm^{-2} for quiet-Sun features A, C, and F, and for a plage model.

Fig. 3.- The electron density distribution (in cm^{-3}) for the four models.

Fig. 4.- The mass density distribution (in g cm^{-3}) for the four models.

Fig. 5.- The continuum optical depth at wavelength 5000 Å for the four models.

Fig. 6.- The emission measure EM determined from equation 1 for the four models.

Fig. 7.- The effective thermal conductivity (κ)for the four models. The dashed lines correspond to the heat flux due to the ionization energy flow alone.

Fig. 8.- The radiative loss function ($\Phi = q_R/n_e n_H$) for the four models. The dashed lines correspond to the hydrogen radiative loss alone

Fig. 9.- The constant-pressure radiative loss function $\Psi = q_R/p^2$ for the four models (solid lines) compared with values given in a recent paper by Woods, et al. 1990.

Fig. 10.- The computed Lyα line profile for model C at disk center.

Fig. 11.- The computed Lyβ line profile for model C at disk center.

Table 1

Parameters of the Models

Model	Z_0 (km)	$T(Z_0)$ (K)	$p(Z_0)$ (dyn cm^{-2})	C_q (erg s^{-1})	$F_E = F_H(Z_0)$ (erg cm^{-2} s^{-1})
A	2125	7828	0.0655	0	580
C	2070	7940	0.138	0	340
F	1969	7950	0.316	2×10^{-15}	692
P	1739	8000	1.225	1×10^{-13}	1.03×10^4

Table 2

Parameters at the upper model boundary

Model	Z_1 (km)	$T(Z_1)$ (K)	$p(Z_1)$ (dyn cm^{-2})	$F_H(Z_1)$ (erg cm^{-2} s^{-1})
A	2200	8.996×10^4	0.0840	4.82×10^4
C	2143	1.028×10^5	0.165	1.06×10^5
F	1991	1.400×10^5	0.448	3.83×10^5
P	1743	1.200×10^5	1.429	1.22×10^6

Table 3

Basic Properties of Model A

T (K)	$Z - Z_0$ (km)	n_p/n_1	V_A (cm s^{-1})	F_H (erg cm^{-2} s^{-1})	q_H (erg cm^{-3} s^{-1})	q_E
1.00E+05	8.05E+01	1.68E+04	1.52E+06	5.15E+04	1.66E-04	3.51E-03
8.00E+04	6.93E+01	2.69E+03	1.25E+06	4.49E+04	5.72E-04	6.78E-03
7.00E+04	6.47E+01	7.36E+02	1.18E+06	4.12E+04	2.09E-03	9.30E-03
6.00E+04	6.10E+01	2.30E+02	1.00E+06	3.69E+04	6.55E-03	1.40E-02
5.00E+04	5.81E+01	1.13E+02	8.05E+05	3.10E+04	1.72E-02	2.44E-02
4.00E+04	5.56E+01	3.81E+01	5.78E+05	2.43E+04	2.87E-02	3.54E-02
3.00E+04	5.34E+01	1.99E+01	3.50E+05	1.62E+04	3.19E-02	3.81E-02
2.00E+04	5.10E+01	1.09E+01	1.55E+05	8.56E+03	1.61E-02	1.99E-02
1.00E+04	4.23E+01	2.72E+00	1.93E+04	3.00E+03	2.02E-03	2.74E-03
8.00E+03	4.21E+00	8.58E-01	2.05E+03	5.80E+02	-5.25E-04	0.00E+00

Table 4

Basic Properties of Model C

T (K)	$Z - Z_0$ (km)	n_p/n_1	V_A (cm s^{-1})	F_H (erg cm^{-2} s^{-1})	q_H (erg cm^{-3} s^{-1})	q_R
1.00E+05	7.17E+01	2.01E+04	1.12E+06	1.04E+05	3.86E-04	1.66E-02
8.00E+04	6.57E+01	1.93E+03	1.39E+06	9.06E+04	3.75E-03	3.28E-02
7.00E+04	6.36E+01	6.82E+02	1.22E+06	8.19E+04	1.67E-02	4.83E-02
6.00E+04	6.18E+01	1.56E+02	1.04E+06	7.28E+04	3.56E-02	6.75E-02
5.00E+04	6.04E+01	7.13E+01	8.06E+05	6.05E+04	7.85E-02	1.09E-01
4.00E+04	5.93E+01	3.21E+01	5.81E+05	4.60E+04	1.27E-01	1.56E-01
3.00E+04	5.82E+01	1.95E+01	3.71E+05	3.06E+04	1.09E-01	1.31E-01
2.00E+04	5.71E+01	1.03E+01	1.72E+05	1.61E+04	6.24E-02	7.49E-02
1.00E+04	5.38E+01	3.06E+00	2.98E+04	7.34E+03	9.88E-03	1.26E-02
8.00E+03	4.90E+00	5.40E-01	6.14E+02	3.40E+02	-1.17E-03	0.00E+00

Table 5

Basic Properties of Model F

T (K)	$Z - Z_0$ (km)	n_p/n_1	V_A (cm s^{-1})	F_H (erg cm^{-2} s^{-1})	q_H (erg cm^{-3} s^{-1})	q_R
1.00E+05	1.49E+01	1.70E+04	7.61E+05	3.16E+05	2.59E-03	1.20E-01
8.00E+04	1.26E+01	2.35E+03	1.06E+06	2.74E+05	1.79E-02	2.61E-01
7.00E+04	1.18E+01	5.40E+02	1.32E+06	2.49E+05	7.67E-02	3.50E-01
6.00E+04	1.12E+01	1.75E+02	1.03E+06	2.21E+05	2.32E-01	4.92E-01
5.00E+04	1.06E+01	6.74E+01	8.22E+05	1.88E+05	5.56E-01	8.07E-01
4.00E+04	1.02E+01	3.21E+01	5.75E+05	1.44E+05	9.32E-01	1.18E+00
3.00E+04	9.80E+00	1.71E+01	3.54E+05	9.49E+04	1.03E+00	1.20E+00
2.00E+04	9.34E+00	9.41E+00	1.63E+05	5.17E+04	5.00E-01	5.97E-01
1.00E+04	8.03E+00	2.76E+00	2.98E+04	2.47E+04	7.29E-02	9.52E-02
8.00E+03	1.07E+00	5.69E-01	1.05E+03	1.50E+03	1.14E-03	5.40E-03

Table 6

Basic Properties of Model P

T (K)	$Z - Z_0$ (km)	n_p/n_1	V_A (cm s^{-1})	F_H (erg cm^{-2} s^{-1})	q_H (erg cm^{-3} s^{-1})	q_R
1.00E+05	3.06E+00	1.65E+04	9.44E+05	1.10E+06	2.79E-02	1.79E+00
8.00E+04	2.41E+00	1.59E+03	1.34E+06	9.49E+05	2.71E-01	2.98E+00
7.00E+04	2.17E+00	4.67E+02	1.23E+06	8.68E+05	9.40E-01	3.67E+00
6.00E+04	1.98E+00	1.63E+02	1.03E+06	7.80E+05	2.69E+00	5.27E+00
5.00E+04	1.82E+00	6.52E+01	8.01E+05	6.68E+05	6.22E+00	8.80E+00
4.00E+04	1.69E+00	3.03E+01	5.82E+05	5.21E+05	1.08E+01	1.39E+01
3.00E+04	1.57E+00	1.60E+01	3.49E+05	3.41E+05	1.21E+01	1.43E+01
2.00E+04	1.42E+00	8.34E+00	1.58E+05	1.77E+05	6.38E+00	6.92E+00
1.00E+04	1.00E+00	2.26E+00	2.70E+04	7.88E+04	9.00E-01	1.13E+00
8.00E+03	0.00E+00	6.52E-01	3.30E+03	1.03E+04	2.36E-01	2.38E-01

Table 7

Lyman Lines Fluxes

Model	$Ly\alpha$ (erg cm^{-2} s^{-1})	$Ly\beta$ (erg cm^{-2} s^{-1})
A	5.29×10^4	1.31×10^3
C	9.02×10^4	2.63×10^3
F	2.25×10^5	7.48×10^3
P	6.79×10^5	2.65×10^4

Table 8

Emitted Intensities at Disk Center

Model	$I_{Ly\alpha}$			I_{Ly3}	
	line center	peak	integrated	line center	integrated
A	1.88×10^4	2.30×10^4	1.64×10^4	1.50×10^3	3.20×10^2
C	3.70×10^4	4.38×10^4	2.83×10^4	3.14×10^3	6.50×10^2
F	1.03×10^5	1.25×10^5	7.09×10^4	8.81×10^3	1.83×10^3
P	3.50×10^5	4.30×10^5	2.14×10^5	3.18×10^4	6.53×10^3

center and peak intensities in ergs cm^{-2} s^{-1} sr^{-1} $Å^{-1}$
integrated intensities in erg cm^{-2} s^{-1} sr^{-1}

Table 9

Emitted Intensities Near the Limb

Model	$I_{Ly\alpha}$			$I_{Ly\beta}$	
	line center	peak	integrated	line center	integrated
A	1.61×10^4	2.12×10^4	1.78×10^4	2.76×10^3	6.46×10^2
C	3.31×10^4	4.00×10^4	2.92×10^4	4.87×10^3	1.07×10^3
F	8.74×10^4	1.12×10^5	7.37×10^4	1.59×10^4	3.67×10^3
P	2.95×10^5	3.84×10^5	2.22×10^5	5.54×10^4	1.28×10^4

center and peak intensities in erg cm^{-2} s^{-1} sr^{-1} $Å^{-1}$
integrated intensities in erg cm^{-2} s^{-1} sr^{-1}

Fig. 1

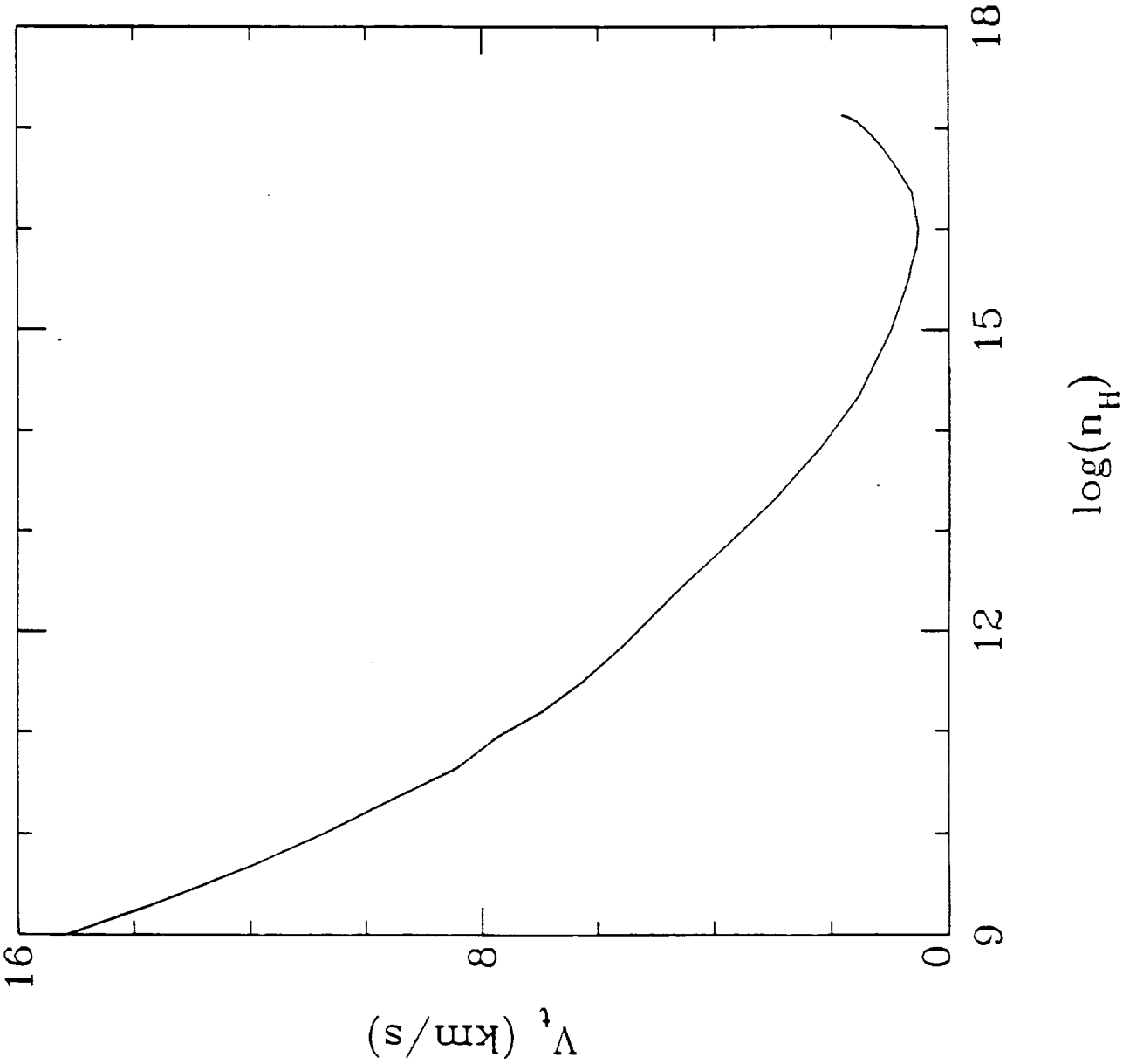

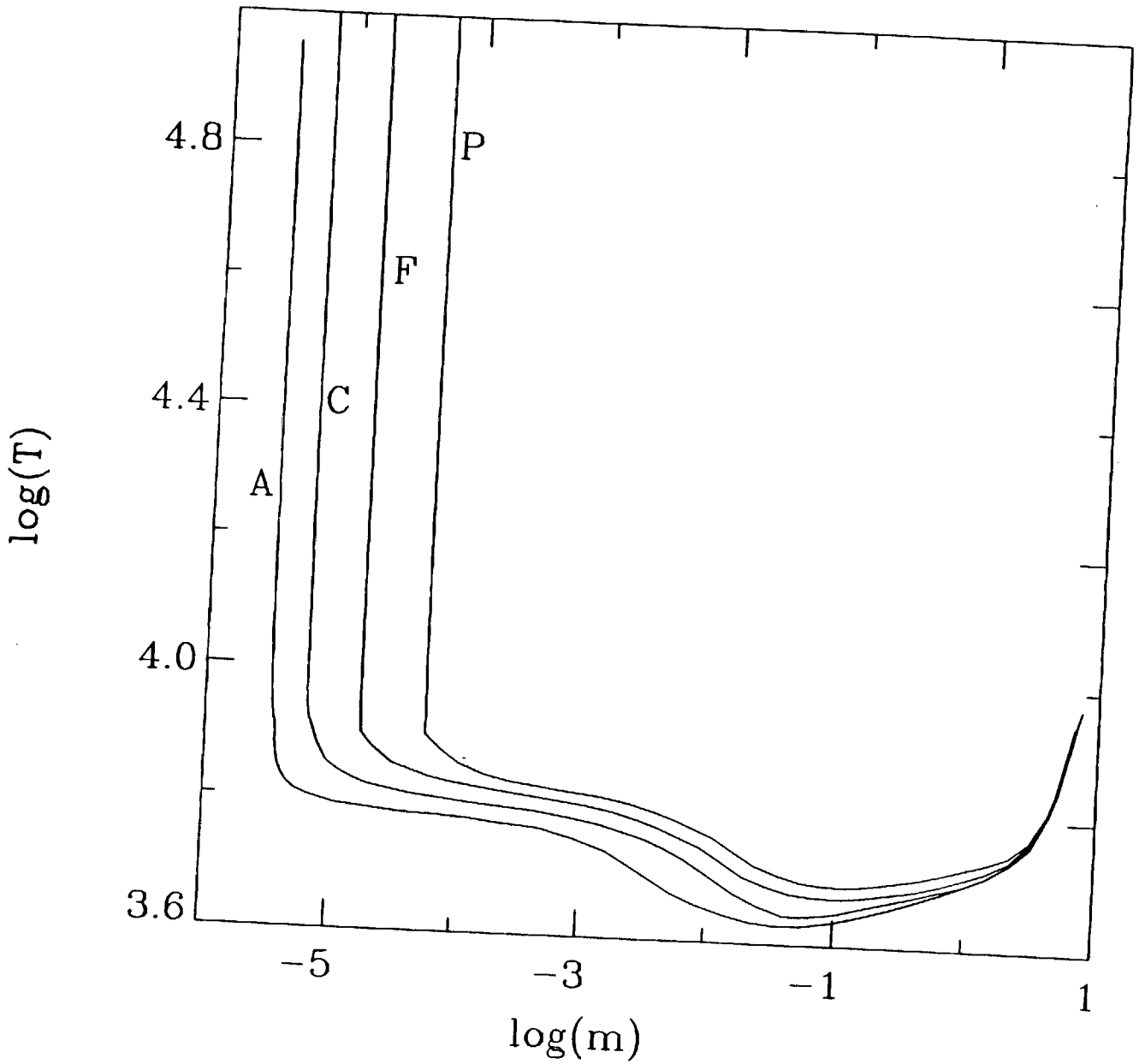

Fig. 2

Fig. 3

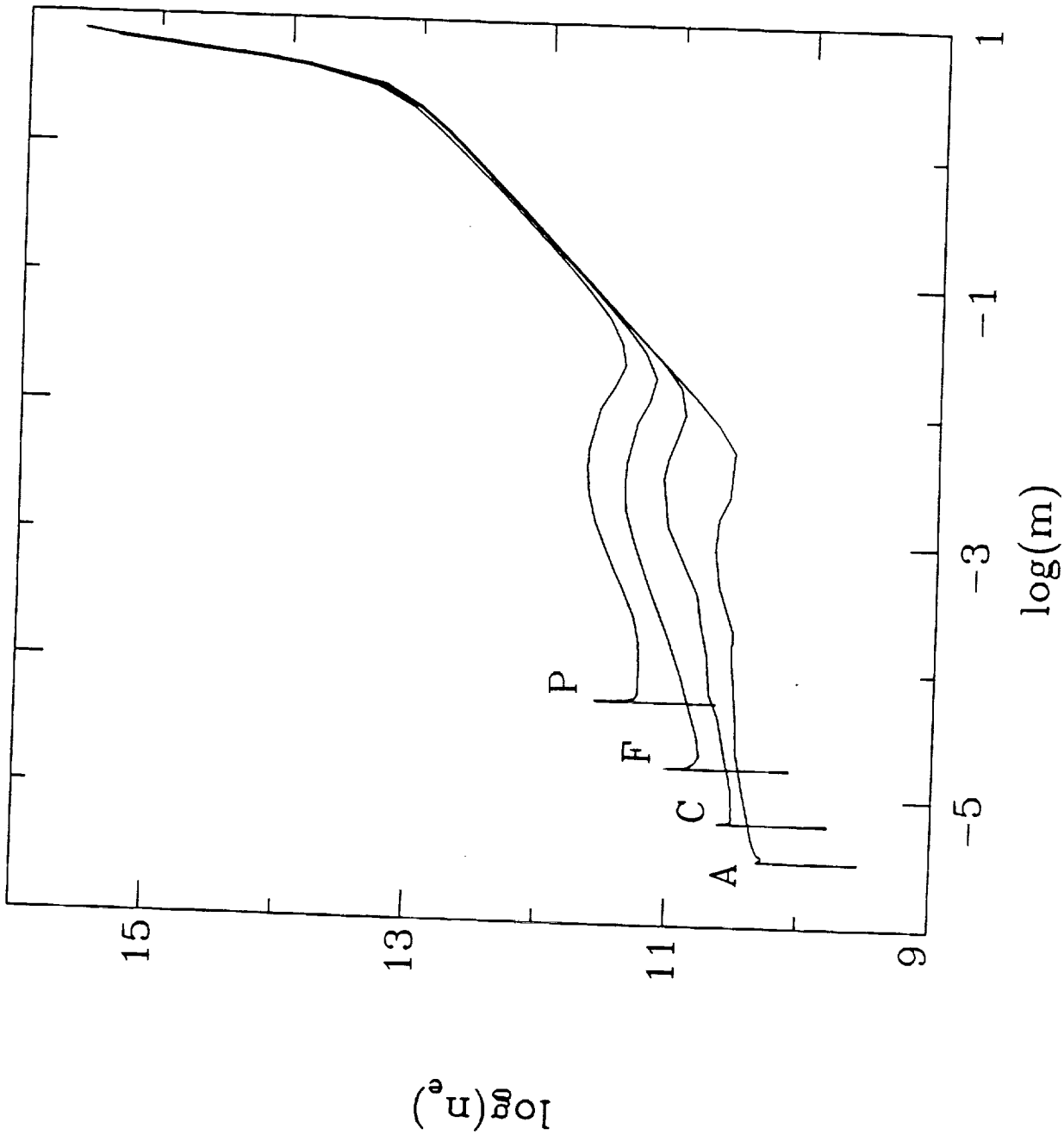

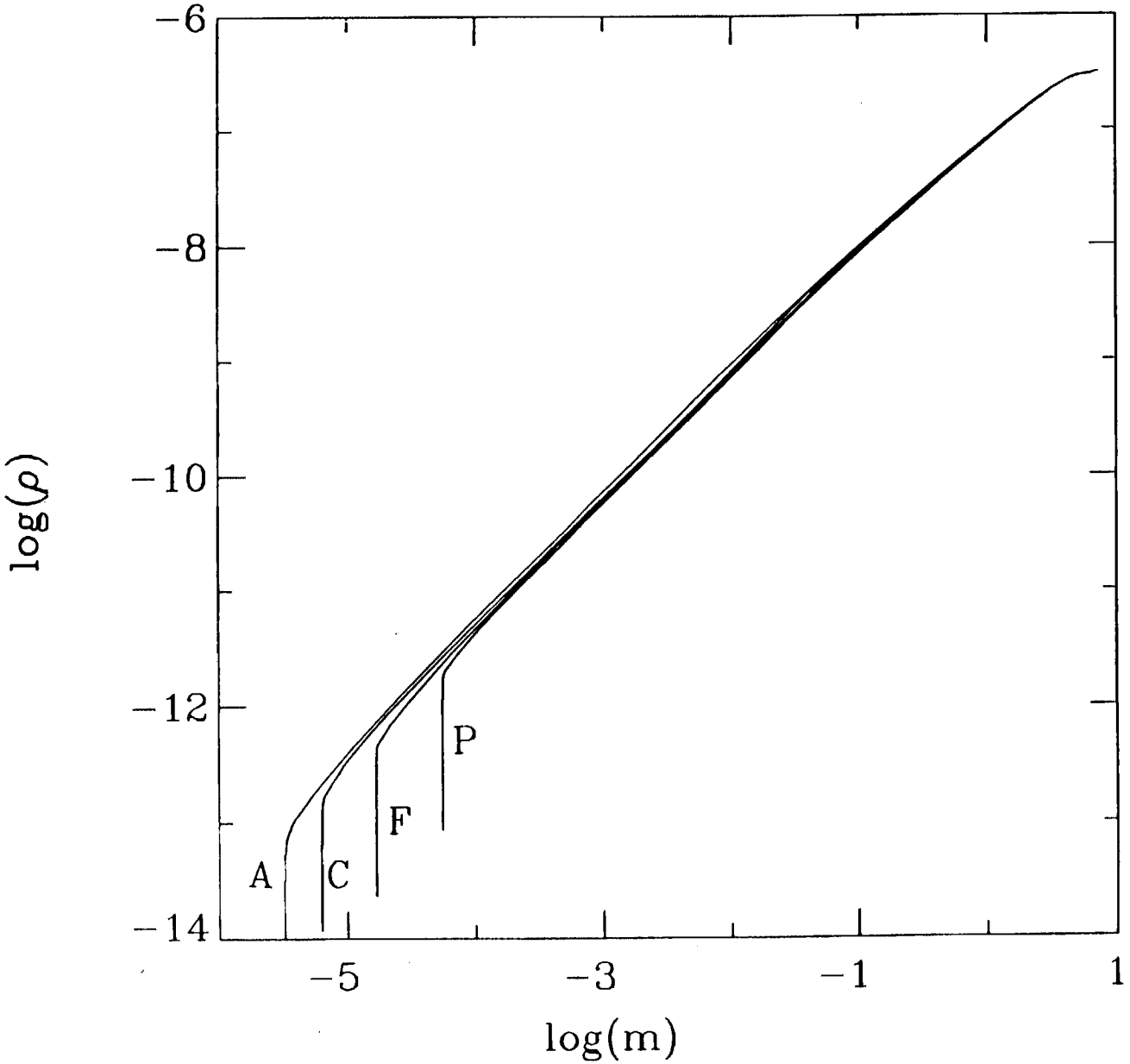
−6
−8
−10
−12
−14
log(ρ)
−5
−3
−1
1
log(m)
A
C
F
P

fig. 5

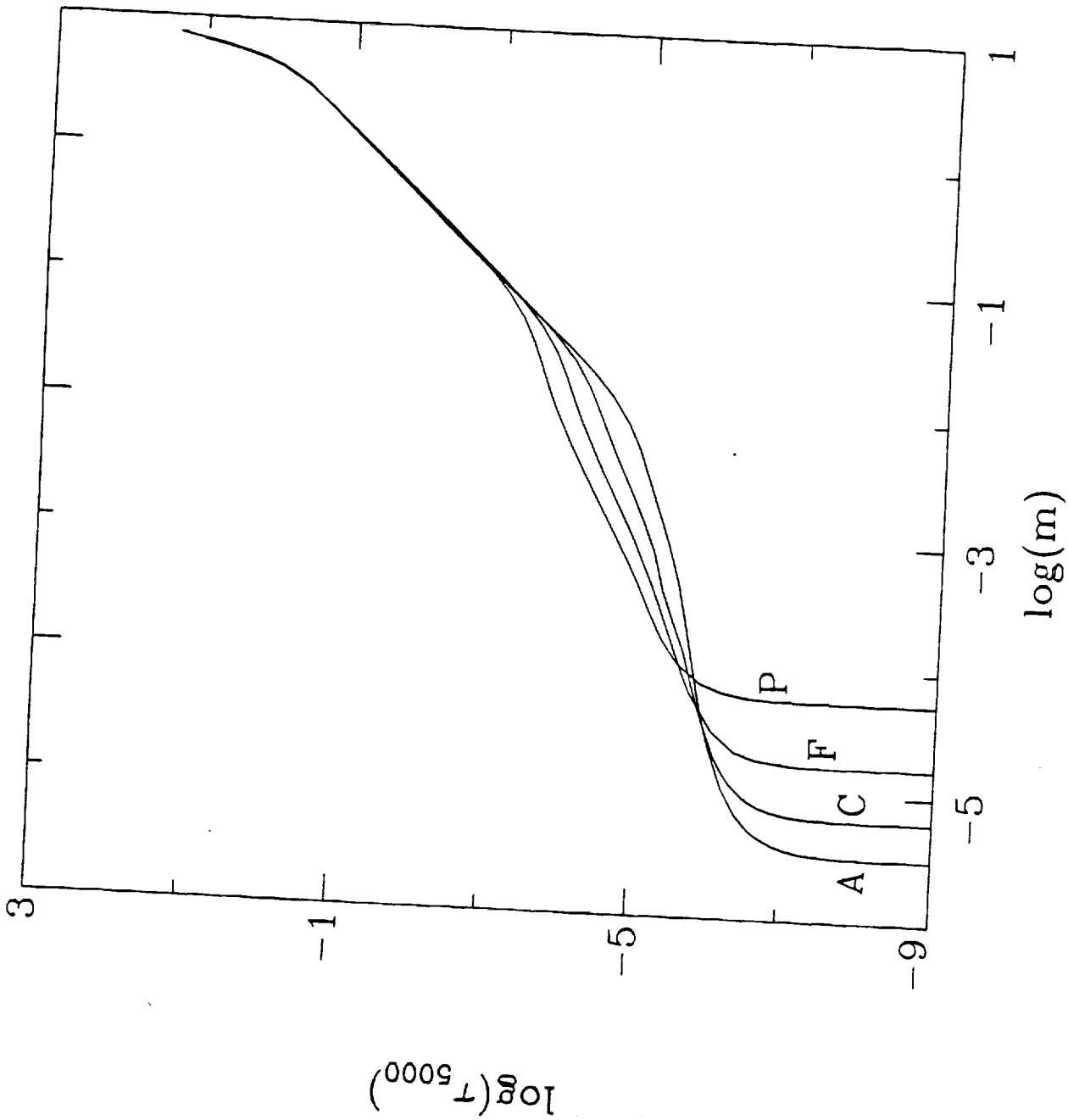

to appear in Proc. Heidelberg Conference on Mechanics of Chromospheric and Coronal Heating

The role of particle diffusion in the lower transition region: revised interpretation of emission measures

Eugene H. Avrett
Harvard-Smithsonian Center for Astrophysics
and
Juan M. Fontenla
The University of Alabama at Huntsville

NASA Support 51-92
N93-13476
p. 2

AV

Our new energy-balance models of the lower transition region are shown in the preceding paper (New Models of the Chromosphere and Transition Region). Here we show the influence of particle diffusion on the calculated hydrogen and helium number densities for a given temperature-density model (model C in the preceding paper).

When there are no diffusion or mass-velocity effects, the ***local*** statistical equilibrium equation for the level-m number density is

$$0 = \sum_{l \neq m} (n_l P_{lm} - n_m P_{ml}), \tag{1}$$

where P_{ij} is the transition rate (s^{-1}) from i to j per particle in the initial state i. When particle velocities are included, this equation becomes

$$\frac{\mathrm{d}}{\mathrm{d}z}[n_m(V_m + U)] = \sum_{l \neq m} (n_l P_{lm} - n_m P_{ml}), \tag{2}$$

where z is geometrical depth, V_m is the diffusion velocity, and U is the fluid or center of mass velocity. V_m has an effect similar to U except that atoms and ions diffuse in opposite directions.

Here we consider only the hydrostatic case with $U = 0$. The diffusion velocity V_m can be calculated from the local temperature and temperature gradient, and the neutral and ion number densities and their gradients.

The derivative term in the statistical equilibrium equation (2) causes the number density at one depth to depend on those at other depths. This is a nonlocal effect that is in addition to nonlocal radiative transfer effects. Both effects combine to modify the ionization of hydrogen and helium.

The proton and neutral hydrogen number densities, n_p and $n_{\mathrm{H\,I}}$, that we calculate for model C are shown in Figure 1 (solid curves) plotted ***vs.*** temperature. Using the same atmospheric model we have repeated the hydrogen calculations without the effects of diffusion; the results are shown as the dashed lines in the same figure. The effect of diffusion is to substantially increase $n_{\mathrm{H\,I}}$ for $T > 25,000$ K and decrease $n_{\mathrm{H\,I}}$ (while increasing n_p) between 8,000 and 18,000 K.

We have also solved the statistical equilibrium and radiative transfer equations for a 13-level He I atom (22 radiative transitions) and a 6-level He II ion (15 radiative transitions) together with He III. The resulting He I and He II level-1 number densities and He III density are shown as functions of temperature in Figure 2. Diffusion substantially increases $n_{\mathrm{He\,I}}$ for $T > 35,000$ K and decreases $n_{\mathrm{He\,I}}$ (while increasing $n_{\mathrm{He\,II}}$) between 9,000 and 25,000 K. Including the effects of diffusion also increases $n_{\mathrm{He\,III}}$ for $T < 60,000$ K.

We are currently preparing a paper for the Astrophysical Journal that will provide the details of these calculations. The overall results shown here indicate that the nonlocal effects of particle diffusion in the statistical equilibrium equations substantially change the hydrogen and

helium number densities in the lower transition region. We plan to carry out the corresponding calculations for heavier elements in the near future.

These results suggest that emission-measure studies of the lower transition region that ignore the nonlocal effects of particle diffusion are likely to be unreliable.

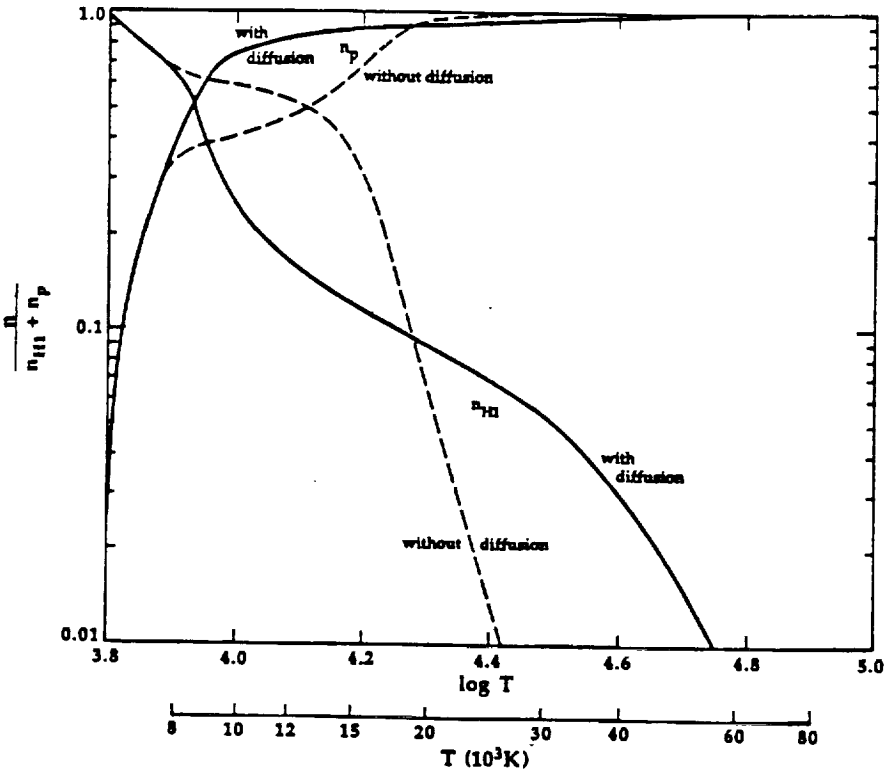

Figure 1. Relative proton and neutral hydrogen number densities *vs.* temperature, with and without the effects of particle diffusion.

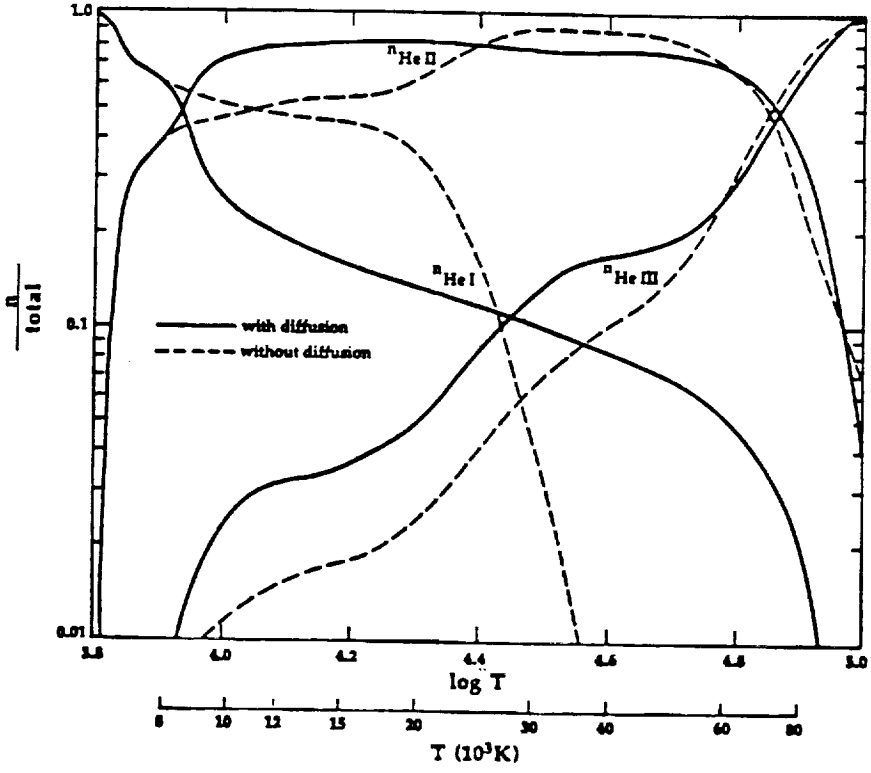

Figure 2. Relative He I, He II, and He III number densities *vs.* temperature, with and without the effects of particle diffusion.

ARCHES SHOWING UV FLARING ACTIVITY

J. M. Fontenla

ES52/Marshall Space Flight Center

to appear in MAX91 Conference Proceedings

Abstract

The UVSP data obtained in the previous maximum activity cycle show the frequent appearance of flaring events in the UV. In many cases these flaring events are characterized by at least two footpoints which show compact impulsive non-simultaneous brightenings and a fainter but clearly observed arch develops between the footpoints. These arches and footpoints are observed in lines corresponding to different temperatures, as Lyman alpha, N V and C IV, and when observed above the limb display large Doppler shifts at some stages. The size of the arches can be larger than 20 arc sec.

Summary

The flaring arches are a rather important constituant of the evolution of active regions in the times between the large flares; also according to Svestka (1988) they constitute a component of the large flares. Their role in the overall energy balance of the active regions is not easy to assess since there is not yet statistics on these events and their distribution and there is no accurate estimate of the released energy in such events.

Since in many aspects the network elements are similar to small active regions, one can expect that these phenomena can also contribute to the energy release in the quiet sun network.

The flaring arches cover a large dynamic range, from rather small events which can be called microflares which are well observed in the transition region lines but at present with no detected counterparts in X-rays and H alpha, up to more energetic events sometimes called compact subflares which display clear X-ray and H alpha signatures.

We belive the less energetic of these events are basically identical to the microflares observed by Porter et al. (1984), and the most energetic are those related with compact flares and can be easily identified in the HXIS X-ray data, like for instance the flaring arches studied by Martin and Svestka (1988).

Some of these UV brightenings are studied by Fontenla et al. (1988) who propose a model of the time development of the brightenings and small UV surges associated with them. The model consists in the sudden release of thermal energy at chromospheric layers where the thermal conduction is not efficiently transmiting the heat to the regions above, nor is able to emit it efficiently in optically thick lines. The resulting overpressure will then accelerate the cold material above along the magnetic field lines and gradually heat it up. This model fits well with the general behavior of the flaring arches we are reporting here, although at that time the X-ray data was unknown to the authors.

The flaring arches are characterized by impulsive brightening of a small area (or primary footpoint) in all transition region lines and (in the cases where we found observations) also in X-rays. Then with extremely short delay, one or more secondary footpoints also display impulsive brightenings. Later, a bridge of fainter emission develops between the footpoints and frequently remains slowly fading after the brightenings of the footpoints dissapear. It is also common to observe more than one simple spike in the primary footpoint (probably in a slightly different unresolved location) and several spikes at different

places along the arch. The phenomenon clearly often shows that the arch consists in several magnetic loops with very close primary footpoints but scattered secondary footpoints, and that there is more than one energy release.

There seem to be a continuous range between the small and the large events. However, in the more energetic events, the footpoints in the UV lines are rather intense; in the brighter events the footpoints were so bright that the UVSP instrument shut off at the times the raster reached the primary footpoint. The bridging material does not show such a large increase of intensity in the transition region lines and may even display a decrease in intensity for the more energetic events. In any case, we observe that the contrast in the transition region temperature material between the footpoints and the bridging material increases dramatically with the intensity of the event.

We have observed flaring arches in lines from Lyman alpha up to Fe XXI, which shows the extreme range in temperature of events of this nature, a span from about 10^4 to at least 10^7 K. It is not clear whether the more energetic events reach higher temperatures or just the emitting volume is not large enough so their high temperature emission can be easily observed. Preliminary comparaison with X-ray shows that at least in the more energetic events, there is a clear correspondance between the transition region lines brightenings and HXIS localized flaring (courtesy of Z. Svestka).

It is of particular importance to observe in several transition region lines with good spatial and temporal resolution, with coordinatedly imaging X-rays to asses the time evolution of the material there. Such observations promise important findings in the process of magnetical energy release which seem to occur in the flaring arches. Particularly the transition region temperature material is able to produce substantial emission that can be detected easier than H alpha emission. The timing between the colder and hotter emissions would indicate wether the material which is being injected into the arch from the primary footpoint is initially hot and cools down (chromospheric evaporation) or is initially cold

and heats up as proposed by Fontenla et al. (1988). The Doppler velocities of the material should also be observed; their relation to the heating or cooling of the material will clarify if the apparent motion constitutes a real mass motion or the progress of a condensation front.

We consider it of great importance to study in Max91 not only the large flares, but also the smaller ones which are more simple in their structure and are more suitable for theoretical modeling and diagnostics.

3-D DESCRIPTION OF VERTICAL CURRENT SHEETS WITH APPLICATION TO SOLAR FLARES

J. M. Fontenla* and J. M. Davis

Submitted To:

The Astrophysical Journal Letters

SPACE SCIENCE LABORATORY
PREPRINT SERIES
NO. 90-119

August 1990

*CSPAR/The University of Alabama in Huntsville
Huntsville, AL 35899

ABSTRACT. Following a brief review of the processes which have been suggested for explaining the occurrence of solar flares we suggest a new scenario which builds on the achievements of previous scenarios, but includes an important addition. This addition is the suggestion that the current sheets, which develop naturally in 3-D cases with gravity from impacting independent magnetic structures (i.e. approaching current systems), do not consist of horizontal currents but are instead predominantly vertical current systems. This suggestion is based on the fact that as the subphotospheric sources of the magnetic field displace or emerge the upper photosphere and lower chromosphere regions, where plasma beta is near unity, will experience predominantly horizontal mass motions which will lead to a distorted 3-D configurations of the magnetic field having stored free energy. In our scenario, a vertically flowing current sheet separates the plasma regions associated with either of the subphotospheric sources. This reflects the balanced tension of the two stressed fields which twist around each other. This leads naturally to a metastable or unstable situation as the twisted field emerges into a low beta region where vertical motions are not inhibited by gravity.

In our flare scenario the impulsive energy release occurs, initially, not by reconnection but mainly by the rapid change of the magnetic field which has become unstable. During the impulsive phase the field lines contort in such way as to realign the electric current sheet into a minimum energy horizontal flow. This contortion produces very large electric fields which will accelerate particles. As the current evolves to a horizontal configuration the magnetic field expands vertically, which can be accompanied by eruptions of material. The instability of a horizontal current is well known and causes the magnetic field to undergo a rapid outward expansion. In our scenario, fast reconnection is not necessary to trigger the flare, however, slow reconnection would occur continuously in the current layer at the locations of potential flaring. During the initial rearrangement of the field strong plasma turbulence develops. Following the impulsive phase, the final current sheet will experience faster reconnection which we believe responsible for the gradual phase of the flare. This reconnection will dissipate part of the current and will produce sustained and extended heating in the flare region and in the postflare loops.

Introduction

It is known that an initially potential or force-free magnetic field configuration containing X-type neutral points, embedded in a highly conducting low-beta plasma, develops magnetic neutral sheets in place of neutral points when strains are externally imposed (see Parker 1983a). This can be understood as the result of the development of electric currents in highly conductive plasma layers arising from externally induced changes of the magnetic field. Because of its diamagnetic character the plasma reacts to these changes by forming rising electric currents which further distort the field and produce forces on the original drivers of the field changes. These forces are such that they oppose the external changes, and are capable of driving substantial motions in a moderate or low beta plasma. The plasma motions are such that the currents collapse into narrow current sheets due to the Lorentz forces. An effect of the formation of the current sheets is to convert the mechanical energy, which went into the driving of the external sources, into the free (and therefore available for dissipation) magnetic energy of the current sheets. The dissipation of the current sheets, through slow magnetic field reconnection, releases this energy and converts it to thermal plasma energy.

The dissipation of numerous small and narrow current sheets produced in the tenuous corona by the shuffling of the magnetic fields by convective motions has been suggested as the source of stellar coronal heating (Parker 1983b). More extended current sheets have been suggested for explaining full fledged solar flares (e.g. Heyvaerts, Priest and Rust, 1977, and Low 1987). These current sheets result from the evolution of large-scale active region magnetic fields. The evolution has been considered a result of emergence of new bipolar field (Heyvaerts, Priest and Rust, 1977), sideways bumping and cancellation of magnetic bipoles (Machado and Moore 1986), or magnetic footpoint displacements (Low 1987). However the problem still remains of how these large current sheets can be built up without in the process experiencing major dissipation of their energy, and why they release their energy impulsively. This requires that the magnetic configuration evolves to a metastable state where it can remain for a substantial time as it builds up its free energy under the action of the slow photospheric mass flows, and that the transition from the metastable state to one of lower energy occurs explosively releasing energy and producing a substantial flux of accelerated particles.

We note that both, the Heyvaerts, Priest and Rust, and the Low scenarios, as well as other flare models (e.g. Kupperus and Raadu 1974, Kopp and Pneuman 1976, and Martens and Kuin 1989), consider the current sheets only in two-dimensions, where the electric currents flow essentially in the horizontal direction while the field expands vertically from a boundary surface at which conditions are imposed. They only consider low-beta plasmas and assume that the footpoints of the field are displaced arbitrarily.

In the case of the Heyvaerts, Priest and Rust scenario the current sheet is nearly horizontal and prevents the emerging field from expanding upwards into the preexisting field (see their Figure 3). These authors suggest that the sheet becomes unstable to reconnection as a result of a thermal instability. In the case of the Low scenario the current sheet is vertical and allows for an upwards expansion of the overlying field (see his Figure 6) as a result of the pulling apart of the magnetic footpoints at the boundary. Both configurations imply the presence of significant forces over the sources which produce the interacting field.

The Stressed Equilibrium

The main difference between our scenario and all others involving current sheets is in the direction of the current flow through the current sheet. All previous models assume that the current in this layer flows horizontally, but our assumption is that it flows vertically. In either case, the currents must close and currents flow in both the horizontal and vertical directions. However, the closing currents are outside of the neutral current sheet, they flow along the magnetic field (i.e. they are force-free) and therefore do not correspond to a strong stress in the field.

Our idea is based on the consideration that, in the solar atmosphere, the low-beta approximation is only good for the coronal layers (beta ~0.0025 for B=100 G). At the photosphere the low-beta approximation does not hold (beta~2.5 for B=1000 G at z=0). In the intermediate layers where the magnetic fields are usually measured (100 <z<600 km) neither the low nor high-beta approximation applies. It is therefore likely that any configuration of the magnetic field which produces Lorentz forces at these levels would result in large scale mass flows such that the magnetic configuration will relax toward net zero force. Of course, these motions will have relatively low velocities, of the order of the subphotospheric flows which are responsible for the stressing. The motions are predominantly horizontal because of the effects of gravity.

Recent measurements of vector magnetic fields have indicated that regions experiencing large flares usually display large magnetic "shear" (Hagyard 1988). This "shear" consists of the departure from a potential configuration of the horizontal component of the magnetic field, and has been interpreted as showing the existence of vertical electric currents (Hagyard 1988, Fan, Canfield and McClymont 1990). These vertical currents are interpreted in a regular force-free magnetic configuration without singular neutral points. However it is not clear whether they bear any relationship to the occurrence of flares. If any of these vertical currents are really current sheets and correspond to neutral sheets (i.e. surfaces of null magnetic field), they would

represent strains of the field which are potential sources of dynamic phenomena and flares. The theory shows that field aligned currents of sufficient magnitude to produce helical magnetic fields would be susceptible to the kink instability before even a few turns are reached. This suggests that helical configurations cannot easily accumulate substantial free energy. However, the electric currents in a neutral sheet can reach high values and are limited only by plasma effects. These current layers correspond to locations in which the magnetic pressure is uniform and the tension forces of two curved magnetic fields balance each other.

In Figures 1 and 2 we sketch the magnetic configuration of our scenario. The figures represent only one of a large number of possibilities depending on the nature of the magnetic fields and possible subphotospheric motions. The figures are simplified schemes intended only for illustrative purposes and must not be interpreted as a detailed model of a particular case. Because of the basic complexity of the three-dimensional representation we give here the details of its construction and present several views. The Figure 1 is generated by plotting the magnetic field lines which result from a system of two parallel line currents (1 and 2) flowing in the y direction. These currents are located in the plane z=0 at x=D and x=-D, and extend from y=-D to y=D with equal intensities I. In Figure 2 we add to the previous currents two antiparallel vertical line currents (3 and 4) which, for practical purposes, represent two vertically flowing current layers. These currents are in the plane x=0 at y=-D/2 and y=D/2, and extend from z=-D/2 to z=D/2 with equal intensities I/5. The sense of the current is opposed in both semi-planes of positive and negative y. In these conditions the field lines emerge from the subphotosphere (plane z=0) and, as they approach the plane x=0, the lines diverge toward large positive and negative values of y in such way as to avoid approaching the vertical currents (3 and 4). Some field lines close without crossing the x=0 plane, others close on opposite sides of this plane by avoiding the vertical currents, while other field lines run above the vertical currents and are not affected by them. Of course, the actual configuration must be more complicated because of the finite size of the current systems and the closing of the currents, for both the line and sheet currents. This closing may occur along the field lines which lie at the boundaries of the sheet and then the configuration would contain both current sheets and related field aligned currents. The configuration shown in the figure can be obtained by setting up an initial potential state with the two line currents and without the current sheet. This state will have a neutral line and it will develop a current sheet as both currents are pulled together. The current sheet will be of the form shown in Figure 2 if the fluid is allowed to diverge horizontally under the action of a central compression and its vertical flow is inhibited by gravity. This structure, as are many of the most interesting cases, will be overlooked in a purely two-dimensional analysis. Considering the magnetic energy of our configuration of Figure 1, we can compute

its energy from the theory of inductance (which saves complicated integral of the magnetic field). If one assumes that the configuration extends to infinity in the y direction one finds that the energy per unit length (along y) diverges logarithmically. However, this is just an artifact of the incompleteness of the model and is due to the lack of consideration of the closing currents (i.e. the whole circuit). In order to deal with this deficiency of the model, and for simplicity, we assume that the currents are limited along the y axis. Under these conditions, the total energy is the sum of the individual self-energies of the two currents plus the mutual interaction energy,

$$E_1 = L_1 I_1^2 + L_2 I_2^2 + M_{12} I_1 I_2$$

where L and M are the self- and mutual-inductances. The total magnetic energy in the configuration of the Figure 2, can be calculated by adding the self and mutual energies due to the vertical currents,

$$E_2 = E_1 + \Delta E$$

with

$$\Delta E = L_3 I_3^2 + M_{31} I_3 I_1 + M_{32} I_3 I_2 + L_4 I_4^2 + M_{41} I_4 I_1 + M_{42} I_4 I_2 + M_{34} I_3 I_4$$

The interaction terms between the vertical and horizontal currents vanish because

$$M_{31} = M_{32} = M_{41} = M_{42} = 0$$

and the mutual term between the vertical currents is negative

$$M_{34} < 0.$$

The energy of this configuration is intermediate between the energies which would result from rotating the two vertical currents into the directions aligned or antialigned with respect to the line currents. The excess energy (ΔE) over the potential case with only the two current lines (E_1) corresponds to stress in the magnetic field and free energy. It is readily seen that dissipating the self-energies of the vertical currents requires the Joule effect and therefore implies reconnection. Alternatively the excess energy can be reduced by a realignment of the currents without Joule dissipation.

We suggest that the current sheet separating two independent magnetic structures must also be vertical in the case where one of the systems emerges slowly within the other (i.e. a current system

emerges slowly into the field of another current system). Horizontal current layers cannot initially develop because in the photospheric layers the plasma beta is lower than unity and the action of gravity makes vertical expansion of the fields very difficult. Instead, vertical current layers can easily develop as the magnetic structures find a stressed, twisted, equilibrium configuration through horizontal motions. In our scenario, these horizontal motions are generated by the field emergence and they are not driven by external horizontal forces. This contrasts with models in which horizontal motions are arbitrarily imposed as a mean to stress the field. During the growth phase of the stressed equilibrium, horizontal motions will occur at the upper photospheric layers. When equilibrium is reached the motions would cease, or at least decrease, while the field remains in a quasi-equilibrium. Slow reconnection will occur at the boundaries of the sheet as the system slowly merges. We consider this stressed equilibrium as an inevitable consequence of the slow merging of the magnetic structures through the upper photospheric layers under the action of gravity. If this merging proceeds faster than the establishment of the stressed equilibrium through the horizontal motions, then, the current sheets may become horizontal and the field will expand upwards as it emerges. This case would not lead to a metastable situation, but only a small stress in the field which is immediately released and would not lead to a solar flare. The situation can be visualized as that of two springs forced against each other while they are prevented from expanding outward by a plane surface. In the stressed equilibrium the lateral tensions balance, but this balance will become precarious as the system emerges slowly into a regime which permits vertical expansion.

We have shown how the slow merging of two current systems through the photosphere drives toward a stressed equilibrium with vertically flowing current layers. Some slow reconnection may be occurring in this stressed state, which will correspond to a heating, or preheating of the area.

The Flare

Now we will show, how this equilibrium unleashes into an erupting phenomena with the capability of particle acceleration. We do not provide any details on how the stressed state is temporarily maintained in the low beta solar corona. However, we suggest that the equilibrium margin is linked both to the fact that the current layers are highly inhomogeneous and composed of many filamentary structures, and to the large size of the whole stressed system. The trigger remains undefined in our scenario. It may be a fluctuation in the position of the footpoints or just a narrowing to zero of the equilibrium margin, due to slow reconnection. We emphasize that

not all currents give rise to a flare, but only those which re responsible for the actual field stress, i.e. those corresponding to the vertical current sheet.

In our scenario the energy available for sudden release is not that of the magnetic pressure but only the part corresponding to the magnetic tension (usually a small fraction). Also, most of the electric currents do not undergo sudden dissipation. Instead, the currents only rearrange themselves in such way as to reduce their interaction energy (i.e. the energy due to their mutual inductance) to a minimum. Once the equilibrium from the previous stressed state is lost, a rapid evolution starts. This evolution corresponds to the releasing of the magnetic stress which was marked by the vertical current layer. As this current layer evolves from vertical to horizontal, the whole magnetic field expands and could even attain an open configuration. This would correspond to a fast eruption, and the unwinding and spreading of the magnetic field over a large volume. The untwisting of the stressed field during this stage releases the magnetic tension and produces strong electric fields. The electric fields, are in turn, responsible for accelerating particles to large energies and for the hard X-ray emission. This phase corresponds to the impulsive phase of the flare. We suggest that during this phase horizontal motions will occur in the low chromosphere reflecting the reaction on the footpoints of the untwisting fields.

Finally, a new pseudo-equilibrium is reached in which the current sheet has evolved to a nearly horizontal configuration. The energy of this configuration is lower than that of the vertical current layer, and the field extends upward to large heights in the corona. The further evolution of the horizontal currents has been suggested previously to relate to prominence eruptions. This final configuration may be either stable or unstable with respect to a fast eruption. Its stability depending on the relative magnitude of the current contained in the sheet to the subphotospheric currents and on the height of the current sheet after it becomes horizontal. If it is unstable the current sheet will collapse and probably be ejected together with a plasmoid of closed magnetic fields. Alternatively it may remain as a quasi-stable feature. In this case slow reconnection will occur and potential loops will appear gradually as the current layer is dissipated. This last process will span times far longer than those of the impulsive phase, and would correspond to the gradual rise and decay phase of flares.

Finally we note that the release of the stress in a particular section of an active region, does not imply the release of all the stress throughout the region. More likely, if the sources of the energy remain (i.e. the approaching of different current systems), the release of the stress in a particular location, will result in the beginning of the accumulation of stress in another area.

The Flux Emergence

The question of magnetic flux emergence is linked to the emergence of new electric currents into a pre-existing field. The pre-existing field, in turn, can be considered as a field produced by some large scale, remote currents. Our view is based in the simple fact that for any magnetic field to exist a current distribution must also exist. We then consider that even at times of minimum solar activity some magnetic field is present in the solar atmospheric regions. Such field is produced by electric currents which are probably buried in the Sun's convective layer, and probably at its base. If a limited size current system emerges toward the solar surface, it will interact with the pre-existing field in two ways. The pre-existing field will exert some force over the current carrying plasma attempting to align the emerging current with that of the original current in the pre-existing field. This force, however, can only affect subtly the deep layers of the Sun because of the large plasma-beta. And could only produce important changes in the motions close to the surface. In addition, there is an effect of generating current layers if the two currents are not aligned.

This is illustrated in the Figures 3 and 4. These figures are again highly schematic and should not be considered as describing an actual model. Rather they are intended to show the physical process which occurs in more complicated situations. In both cases we include a buried line current producing a magnetic field above z=0, and an emerging line current close to the surface.

In Figures 3 the emerging line current is parallel to the buried current and in Figure 4 the emerging current is antiparallel to the buried current, in both cases the emerging current is smaller. In Figure 3a the emerging current is somewhat below the surface z=0, and the net potential magnetic field does not have neutral layers. In Figure 3b, after the emerging current reaches the surface, the field modifies by expanding vertically. In this case the change in the field does not affect the topology of the lines but only their shape. The change can be achieved by slow continuous plasma motions and neither substantial electric currents nor current layers are necessary.

When the emerging current is antiparallel to the buried line current the situation is very different (Figure 4). This case is likely to occur when new active regions emerge in the midst of the pre-existing field left by the previous solar cycle. In Figure 4a, we show the case when the emerging line current is slightly below the surface. In spite of its apparent complexity this field configuration is strictly potential above the plane z=0 and although it contains neutral layers it has no currents above this plane. Figure 4b shows a similar potential case with the emerging current line at the level z=0. Comparing Figures 4b and 4a it is clear that many field lines are, again, distorted without change in the topology. However two of the field lines (marked A in the Figure) have changed their topology by jumping over the others. This change cannot result from a continuous smooth evolution of the field and thus it would lead to the formation of a current sheet at

the neutral layer. The vertical orientation of such current layers will allow the magnetic field to circle around one another in the way it is shown in Figure 5, in which a vertical line currents have been added to describe the current sheet. We suggest that the configuration shown in Figure 5 is an intermediate stage in the evolution of the field from that shown in Figure 4a, as the new field emerges. The slow dissipation of the current layers would, then, bring the configuration to that of Figure 4b through reconnection. Similar formulae to those previously used can be considered to estimate the energy of this configuration, and analogous arguments can be used about its stability and possible flaring.

We stress that in many respects our scenario for the field emergence is similar to that for field "impacting" since they base on approaching currents.

Conclusions

We have presented a scenario for the building up of magnetic stress which in a natural manner leads to a metastable equilibrium in which current sheets result from the strains caused by the large scale motions of sub-photospheric current systems. We show some typical cases which in spite of their highly simplified nature display features commonly observed in coronal images. Our scenario applies to active regions which contain mixed polarity regions in which major solar flares have their origin. In contrast with previous models, our scenario contains vertical current sheets in which the electric current flows vertically. Lateral stresses develop from the predominantly horizontal motions of the upper-photospheric and lower-chromospheric layers. These stresses are released during the impulsive phase of the flare in which the electric currents associated with the current sheet rotate from the vertical to the horizontal direction. The rapid change in the orientation of the magnetic field produces large electric fields capable of accelerating substantial beams of high energy particles. Accompanying this change a large increase in the plasma turbulence allows for an increased rate of current dissipation, heating and reconnection. The realigned currents can result in stable or unstable situations. In the former case the electric currents are maintained subject to a slow dissipation, or in the latter are ejected together with the associated plasmoid of closed magnetic fields.

Our scenario opens a variety of new questions which require both detailed observation and modelling. Detailed observation of the vector magnetic field would reveal the locations and magnitudes of the vertical neutral current layers. Observations of the photospheric motions would give further indication of the locations of the current layers and how they evolve. Modelling is needed to find how these currents interact, how much free energy is stored

and what is the stability margin for its release.

Acknowledgements

We thank Dr. R. Moore for helpful discussions on the characteristics of flares.
JF acknowledges support from NASA/ MSFC grant NAG8-@@

References

Fan, Y., Canfield, R.C., and McClymont, A.N. 1990, 176th AAS Meeting.
Hagyard, M.J. 1988, Solar Phys., 115, 107.

Heyvaerts, J., Priest, E.R., and Rust, D.M. 1977, Ap. J., 216, 123.

Kopp, R.A., and Pneuman, G.W. 1976, Solar Phys., 50, 85.

Martens, P.C.H., and Kuin, N.P.M. 1989, Solar Phys., 122, 263.

Kuperus, M., and Raadu, M.A. 1974, Astron. Ap., 31, 189.

Low, B.C. 1987, Ap. J., 323, 358.

Machado, M.E., and Moore, R.L. 1986, Adv. Space Res., 6, 217.

Parker, E.N. 1983a, Ap. J., 264, 635.

Parker, E.N. 1983b, Ap. J., 264, 642.

Figure Captions

Figure 1. The magnetic field configuration corresponding to the two line currents shown in dashed lines. The currents lie in the plane z=0 and extend parallel to the y axis at x=+1 and x=-1. a) Perspective view; b) front view.

Figure 2. Similar to the previous except that two vertical line currents have been added (shown in dashed line) to mimic the current layers resulting from the approaching of the horizontal currents. a) Perspective view; b) front view; c) top view.

Figure 3. The emergence of an horizontal current line in the field of a deeper seated current. In the case shown in this figure both currents are parallel. A front view is shown here. a) Emerging current below the surface at z=-0.2; b) emerging current right at the surface z=0. Front view.

Figure 4. Similar to Figure 3 but with the emerging current antiparallel to the deep seated current. a) Emerging current below the surface at z=-0.2; b) emerging current right at the surface z=0. Front view.

Figure 5. Similar to Figure 4 but with a vertical line current (dashed line) added to mimic the current layer resulting from the emergence of the upper horizontal current. Notice how some lines remain at the same altitude as before the emergence but move sideways to allow the new field emergence. a) Perspective view; b) front view; c) top view.

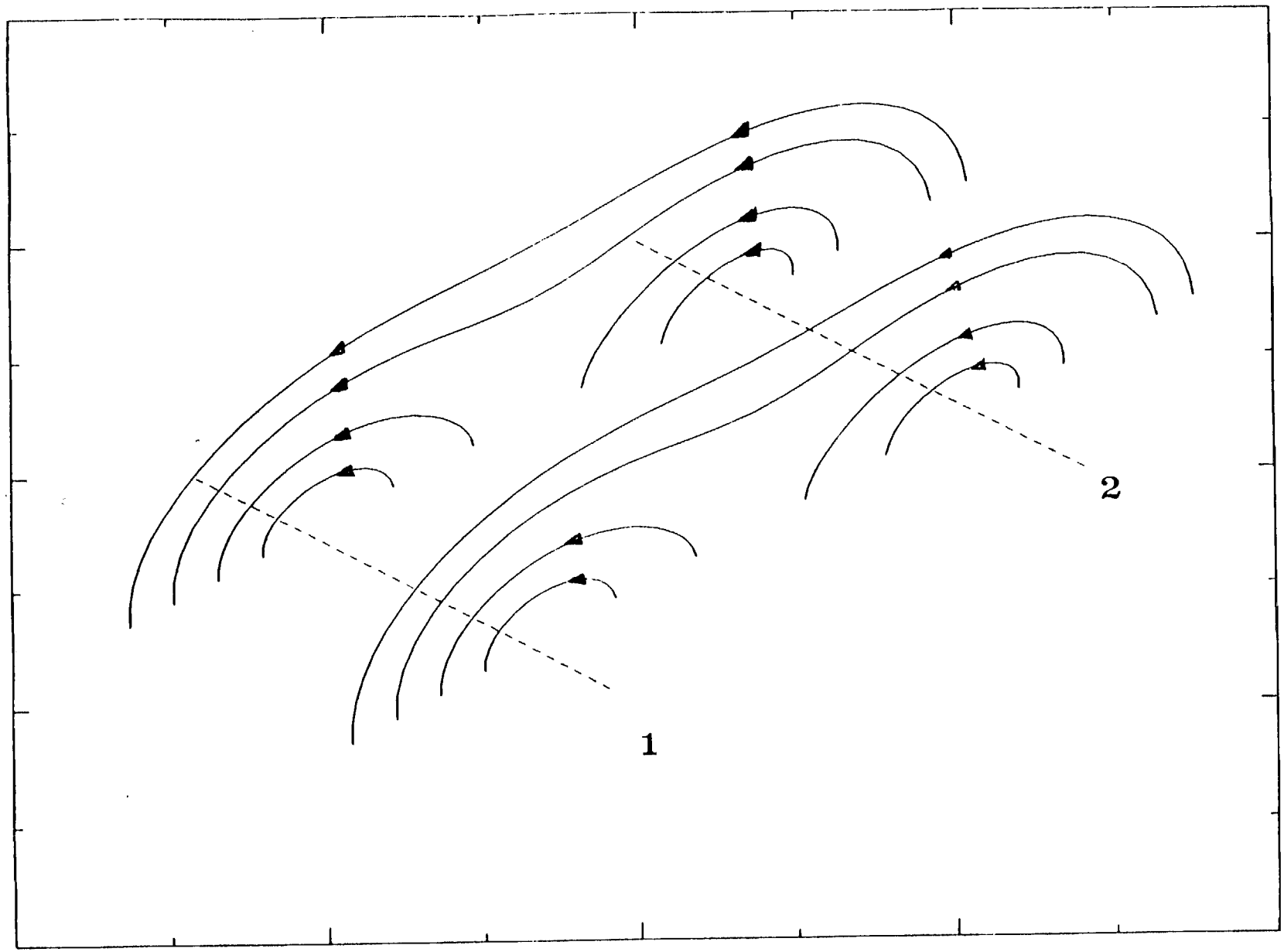

Fig. 1a

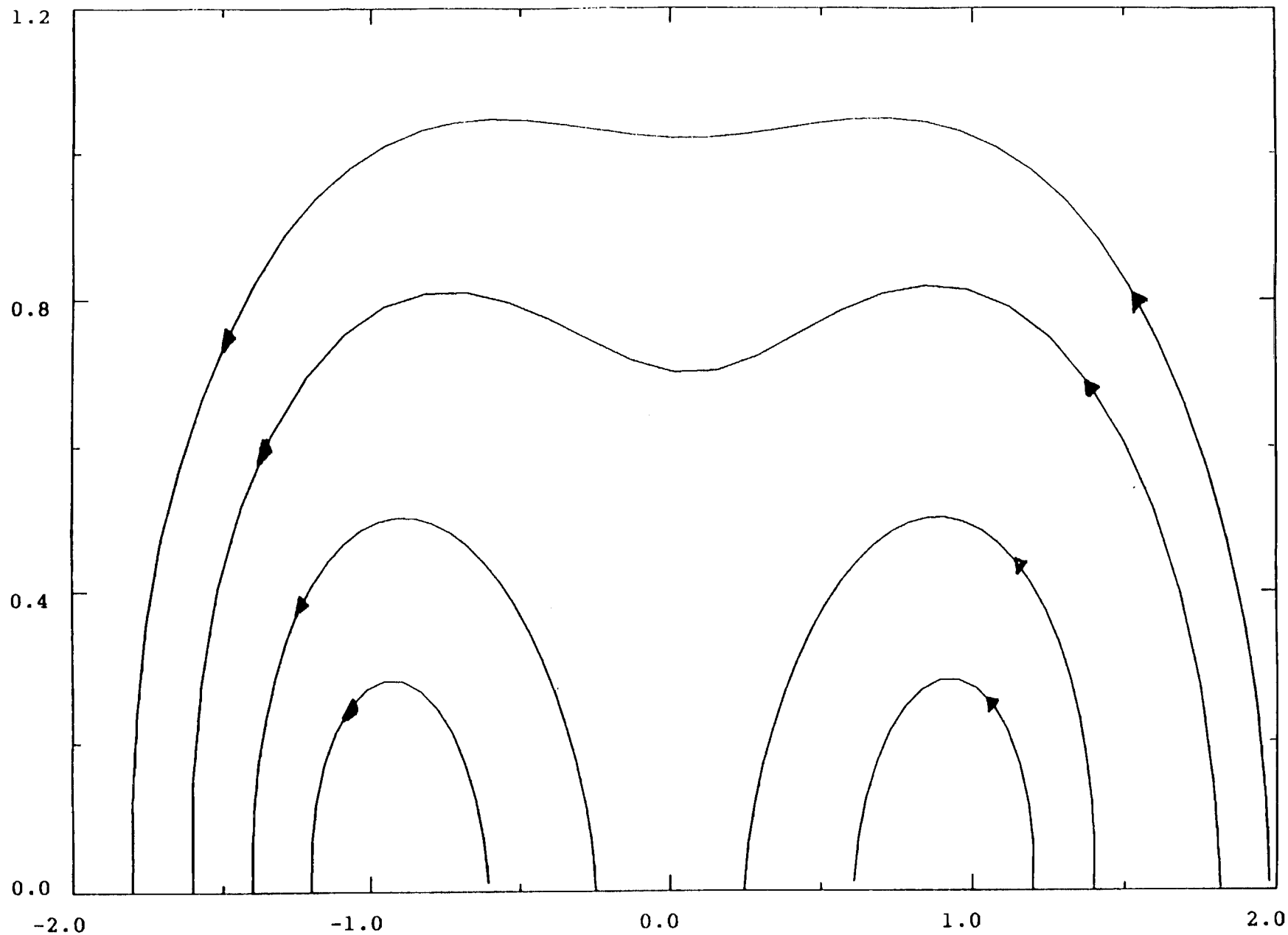
1.2
0.8
0.4
0.0
Z
-2.0
-1.0
0.0
1.0
2.0
X

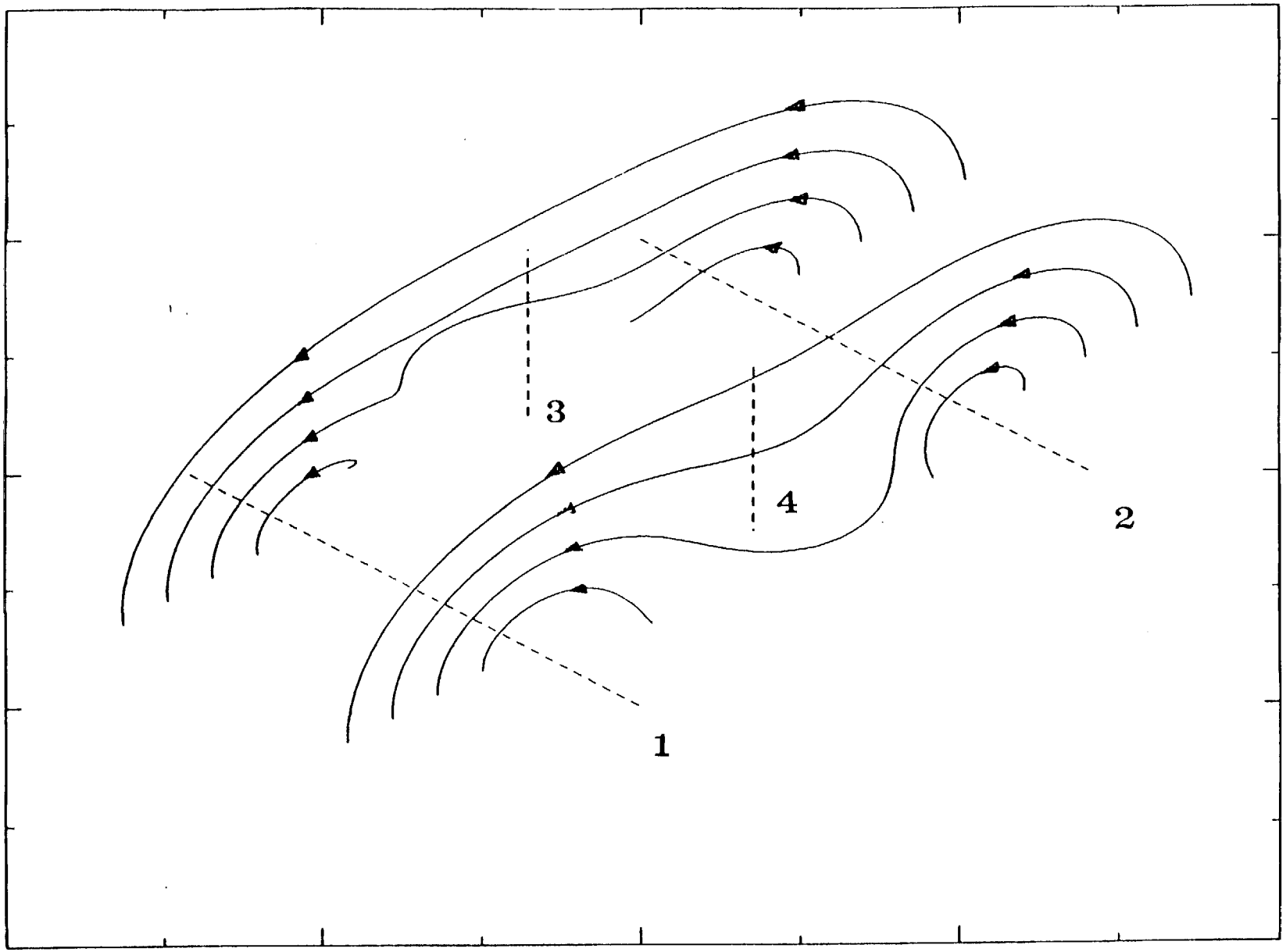

Fig. 2a

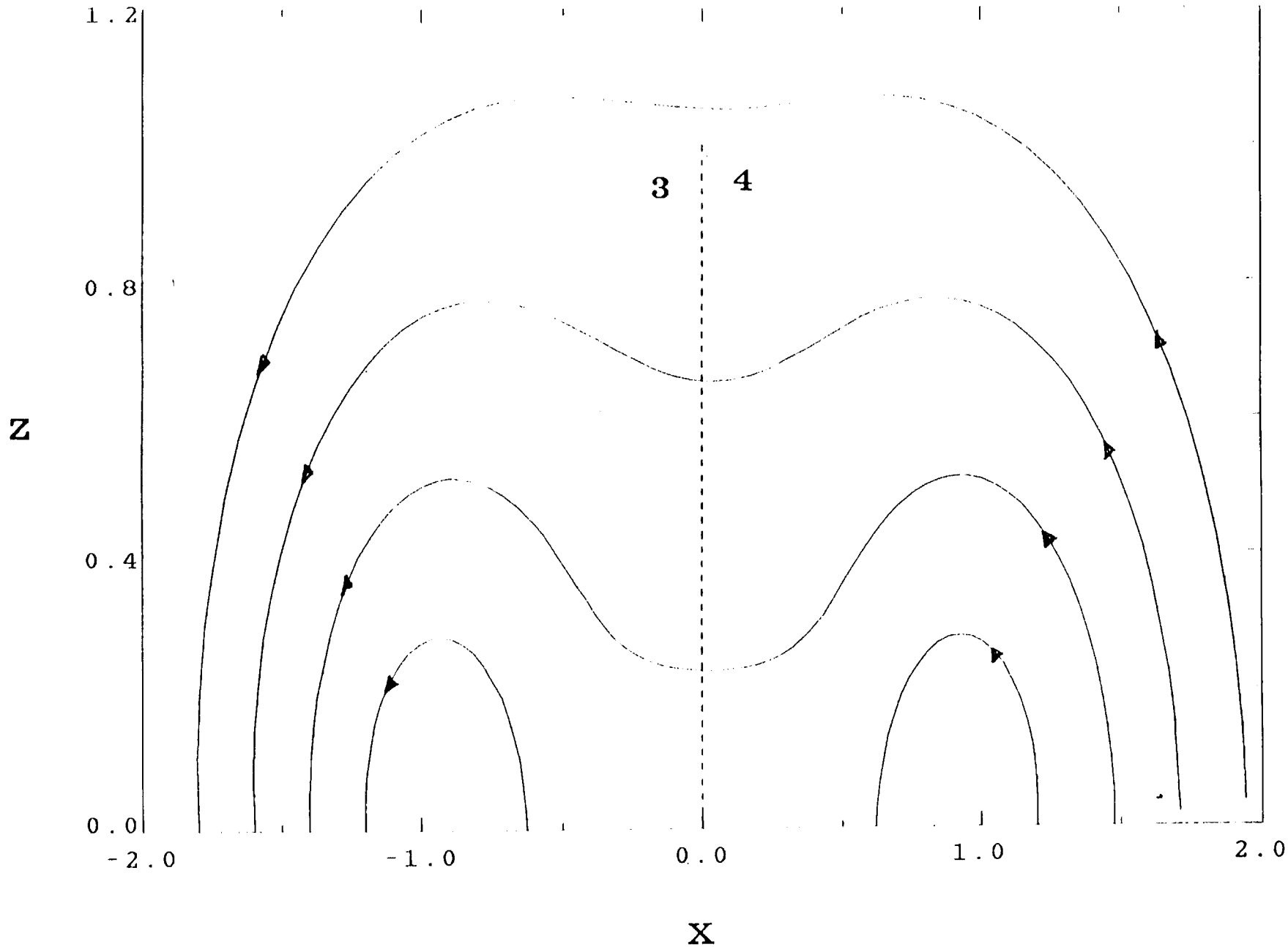

Fig. 2b

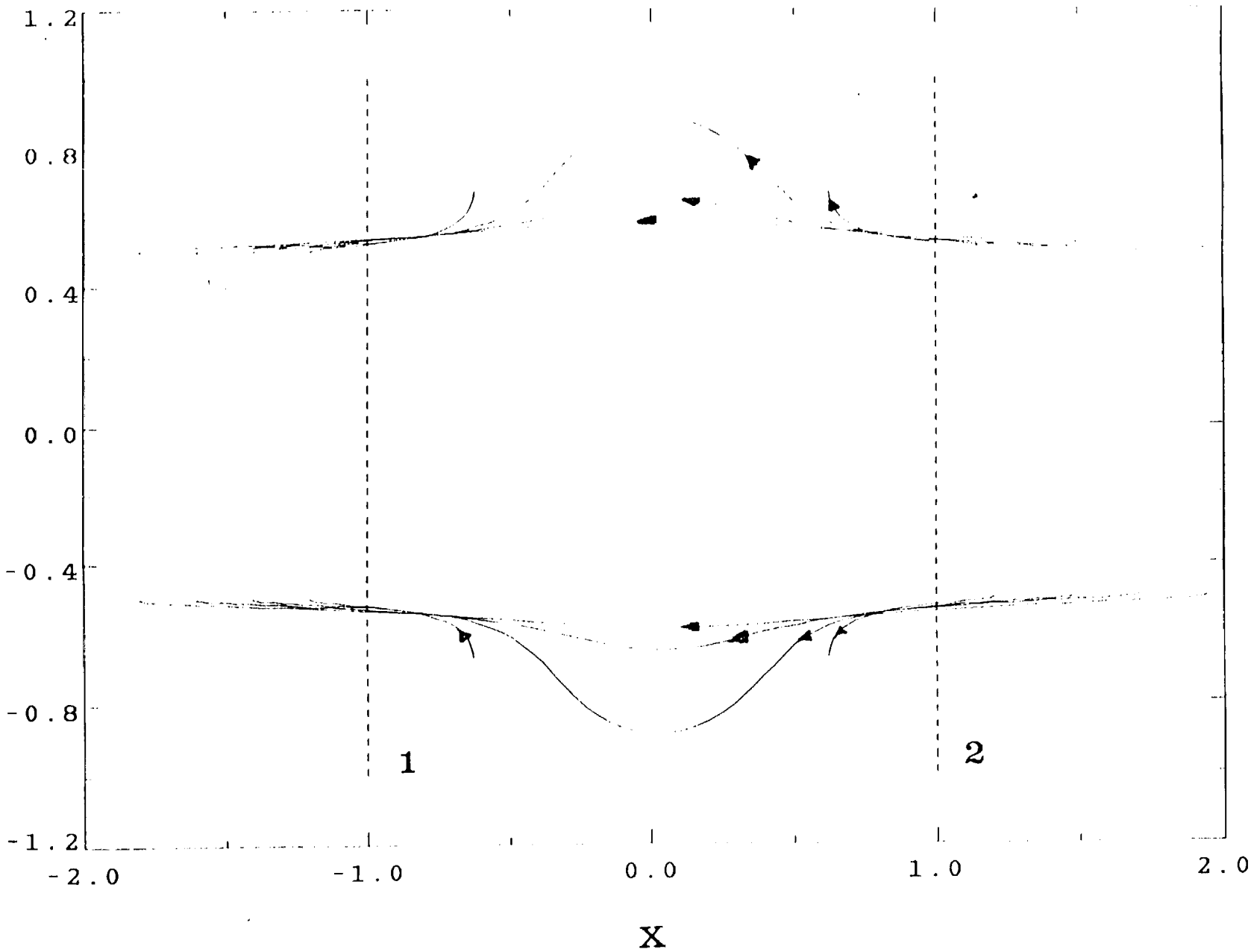

Fig. 2c

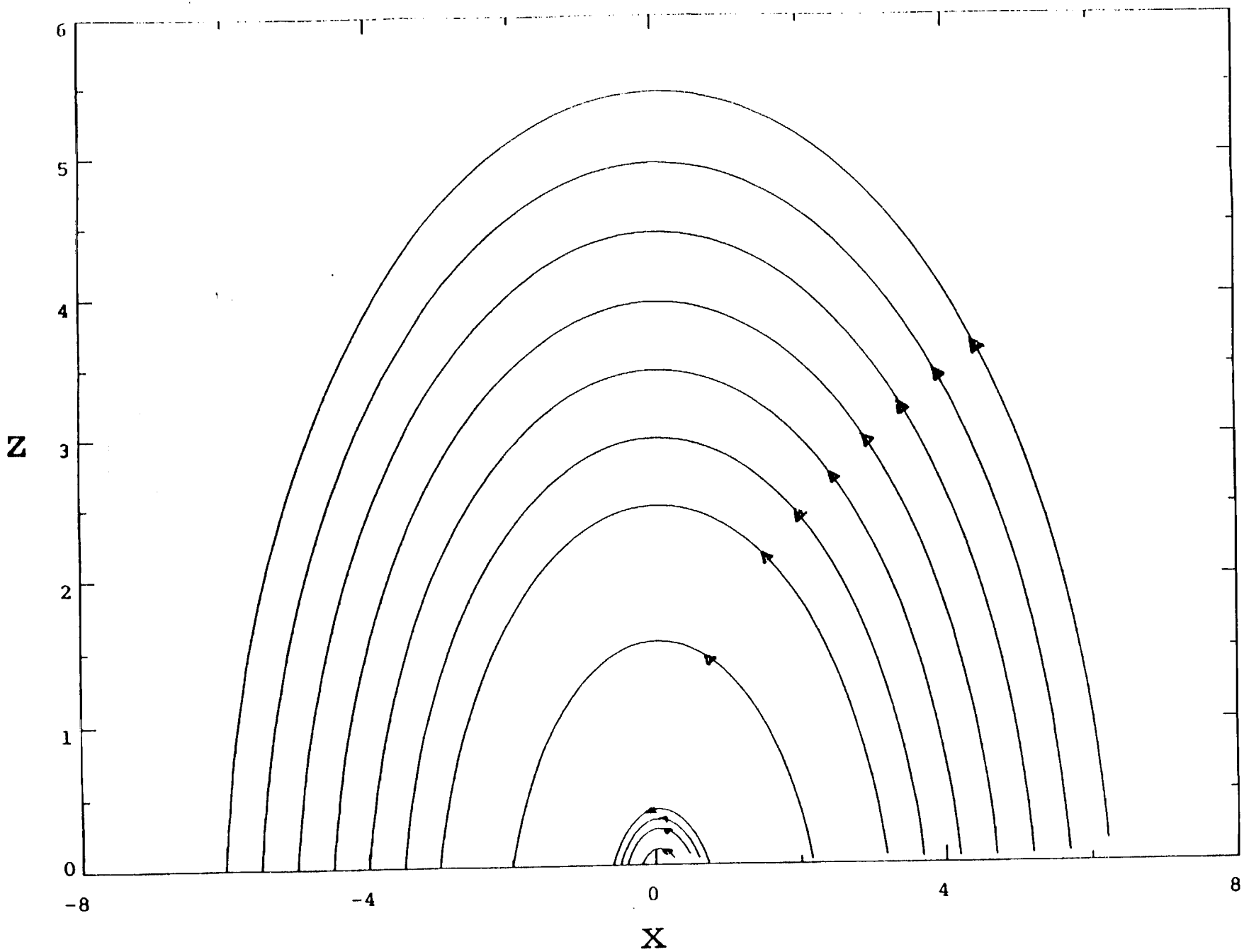

Fig. 3a

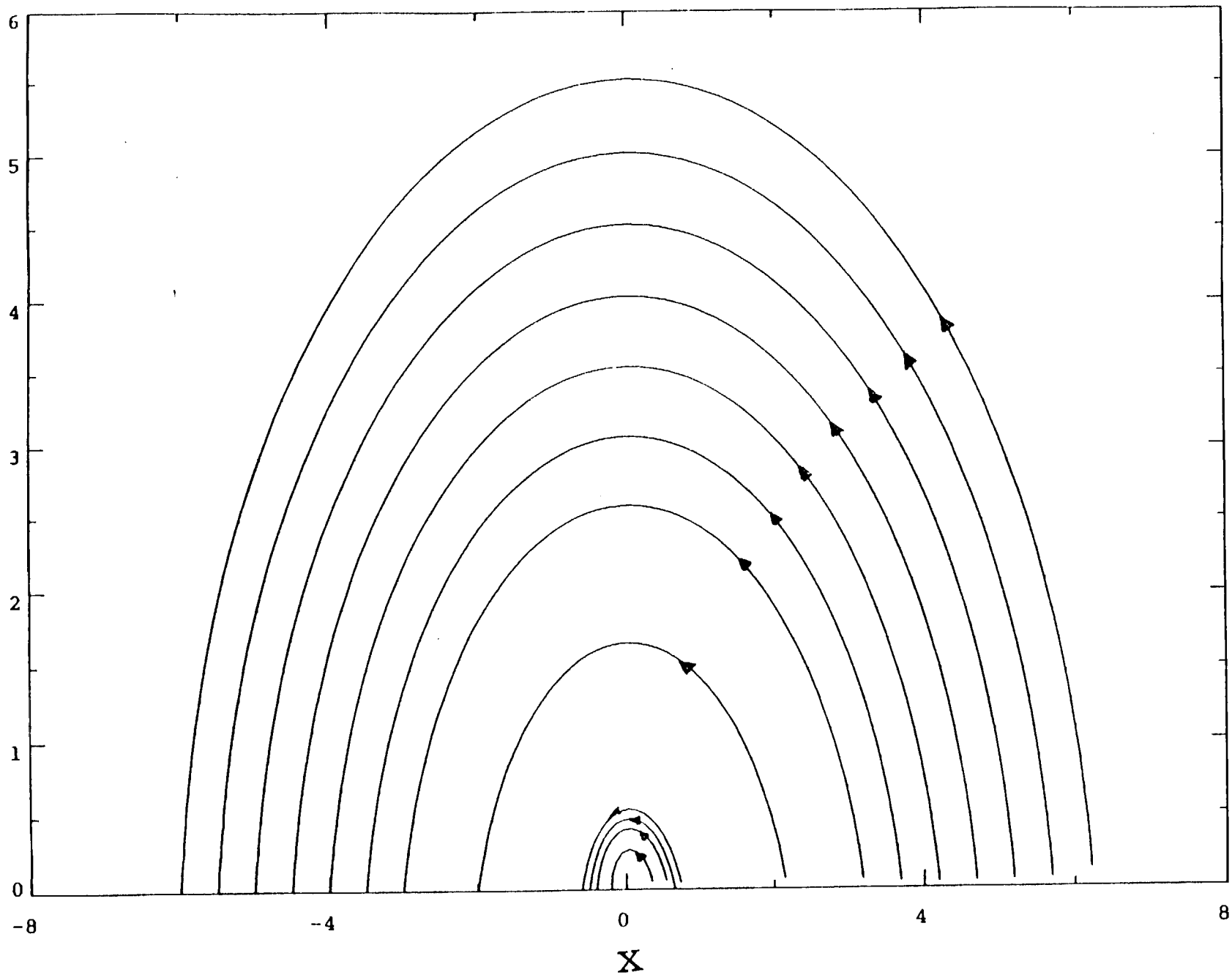

Fig. 3b

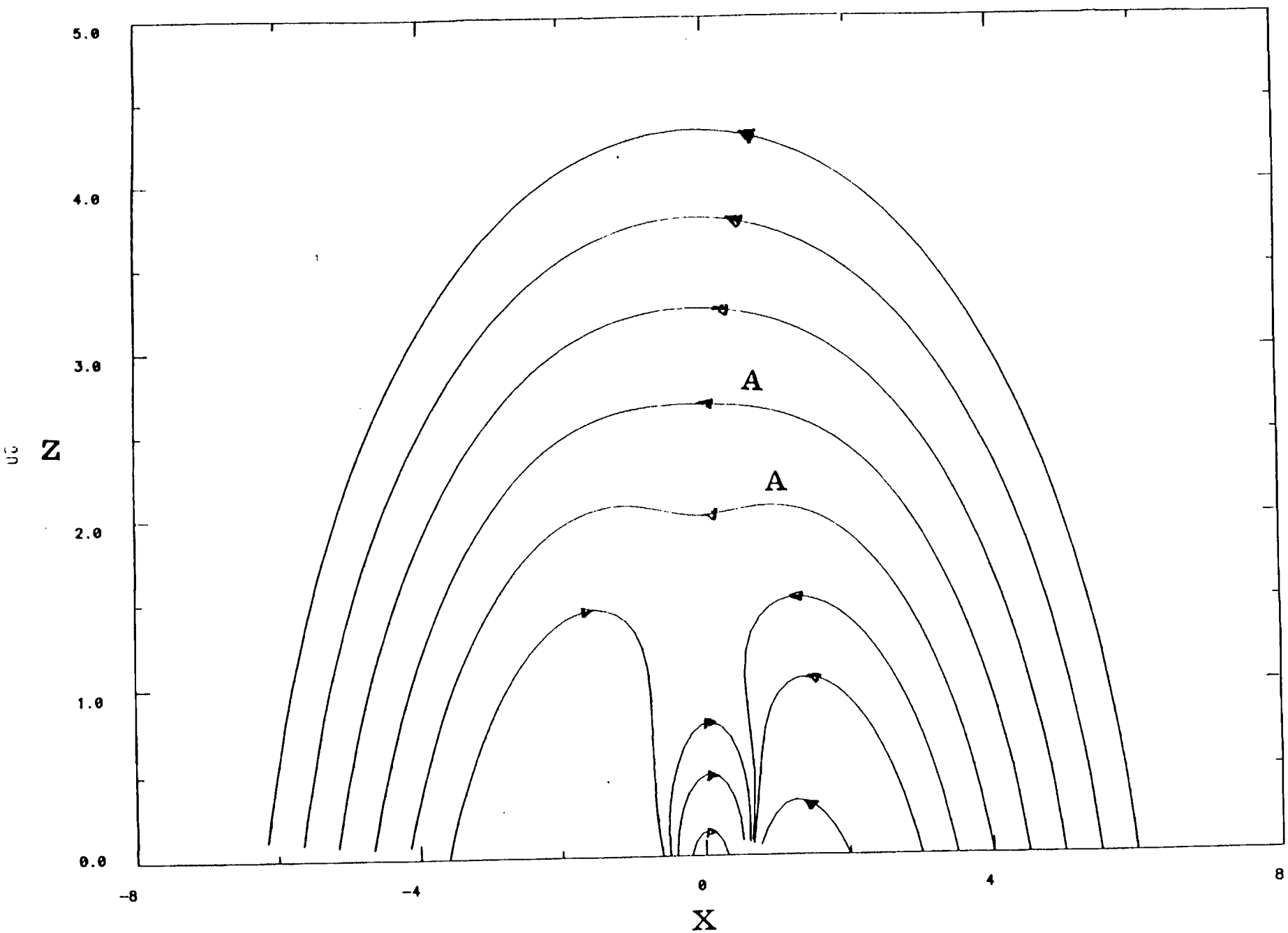

Fig. 4a

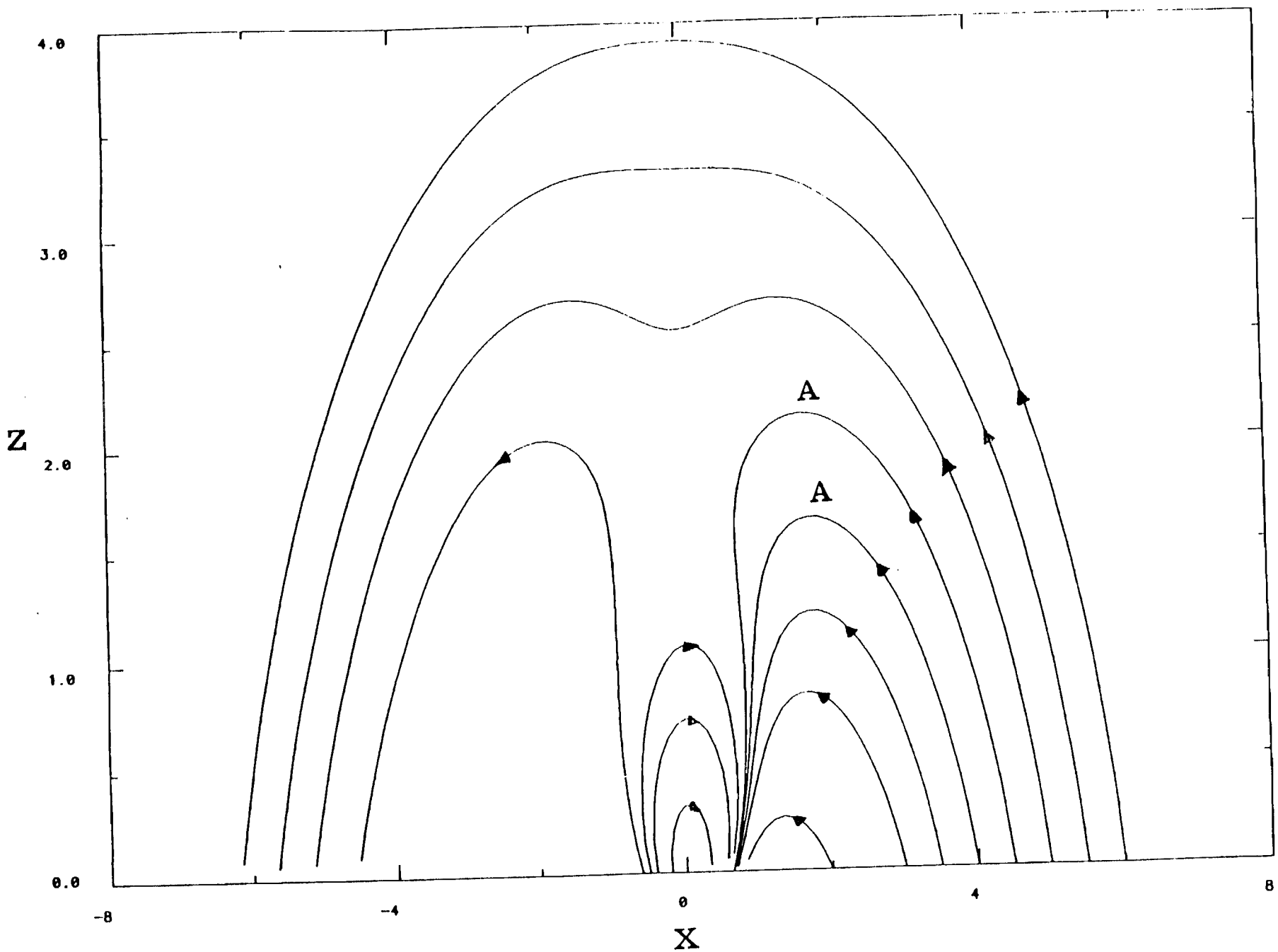

Fig. 4b

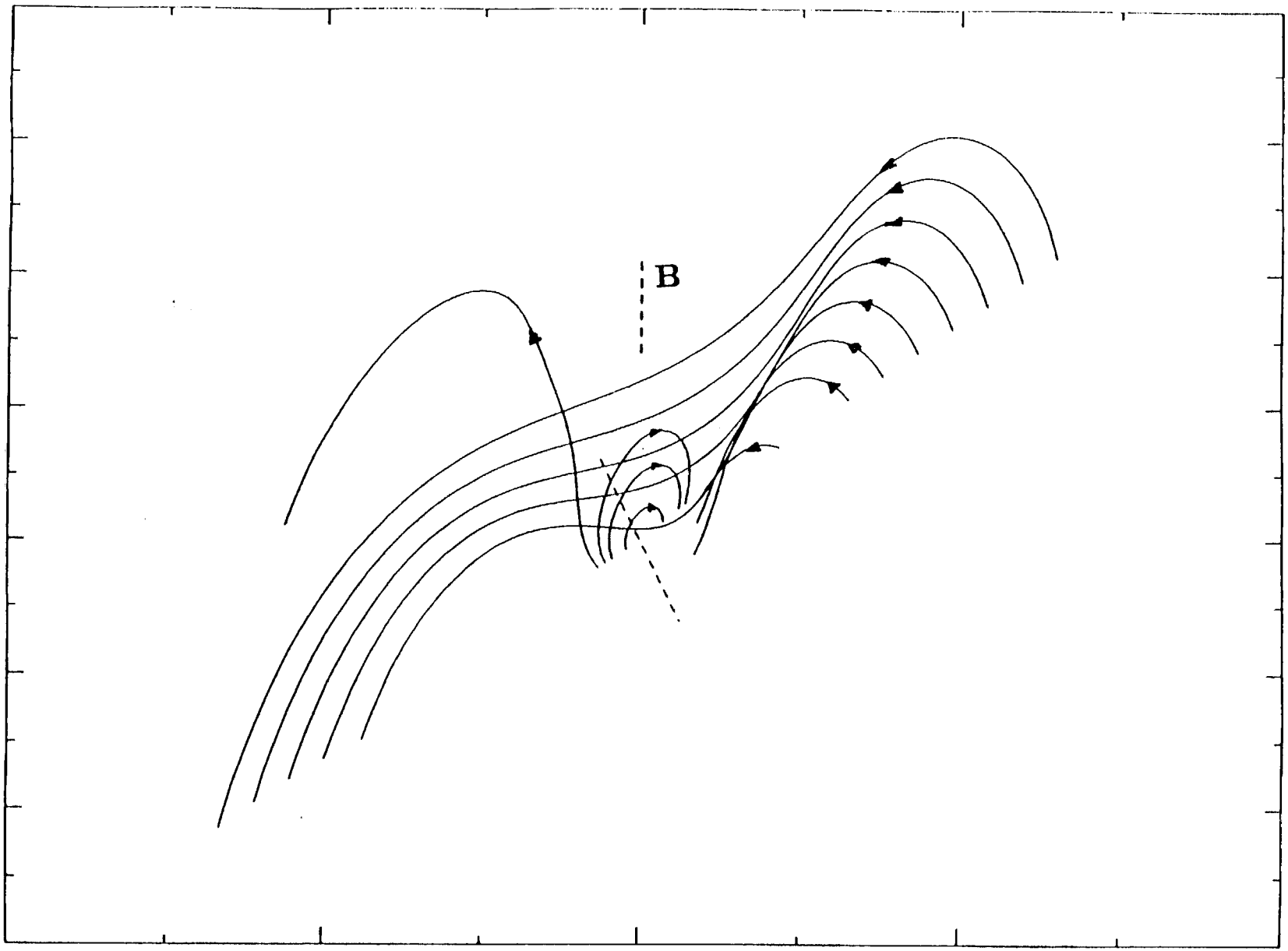

Fig. 5a

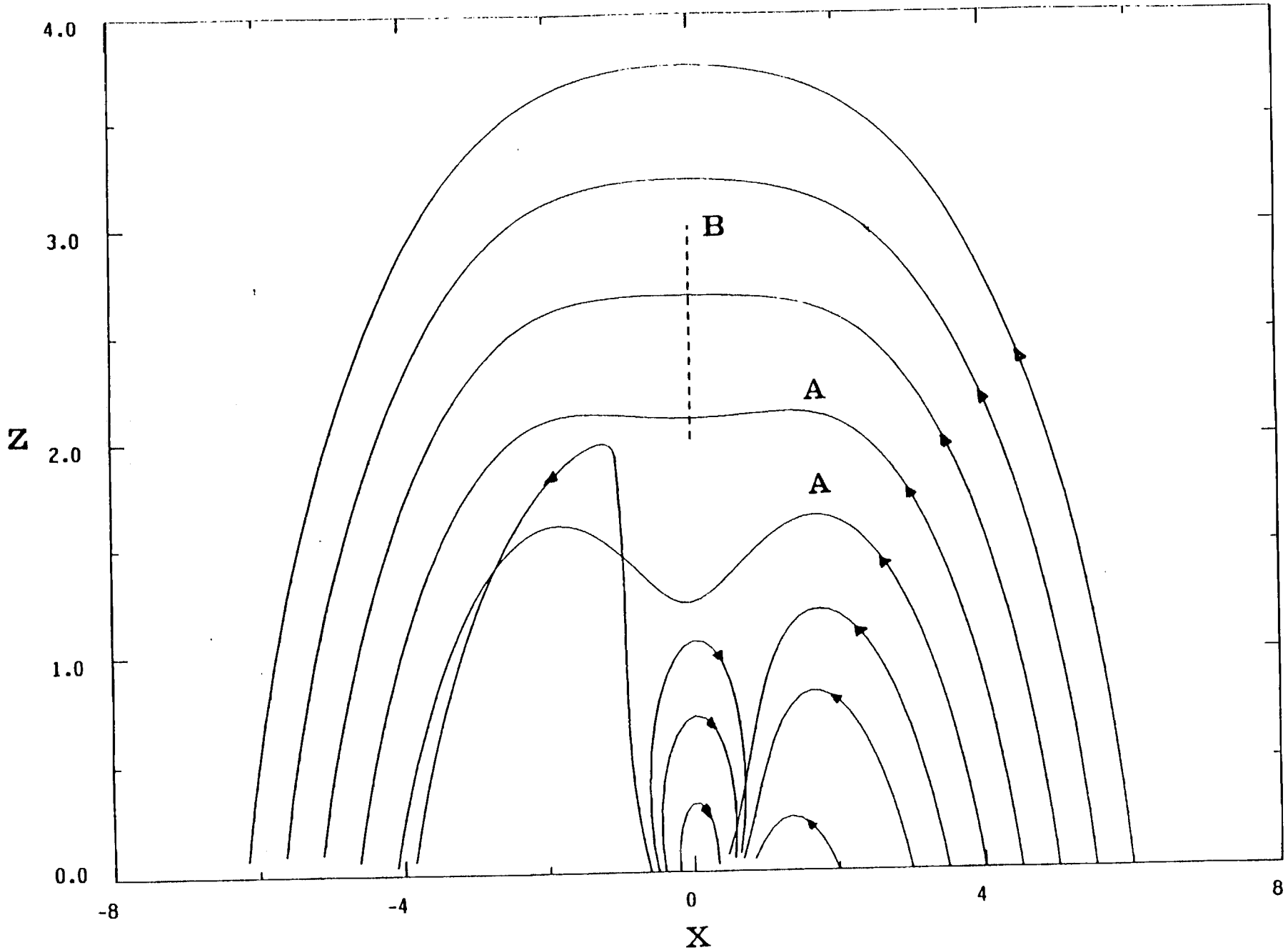

Fig. 5b

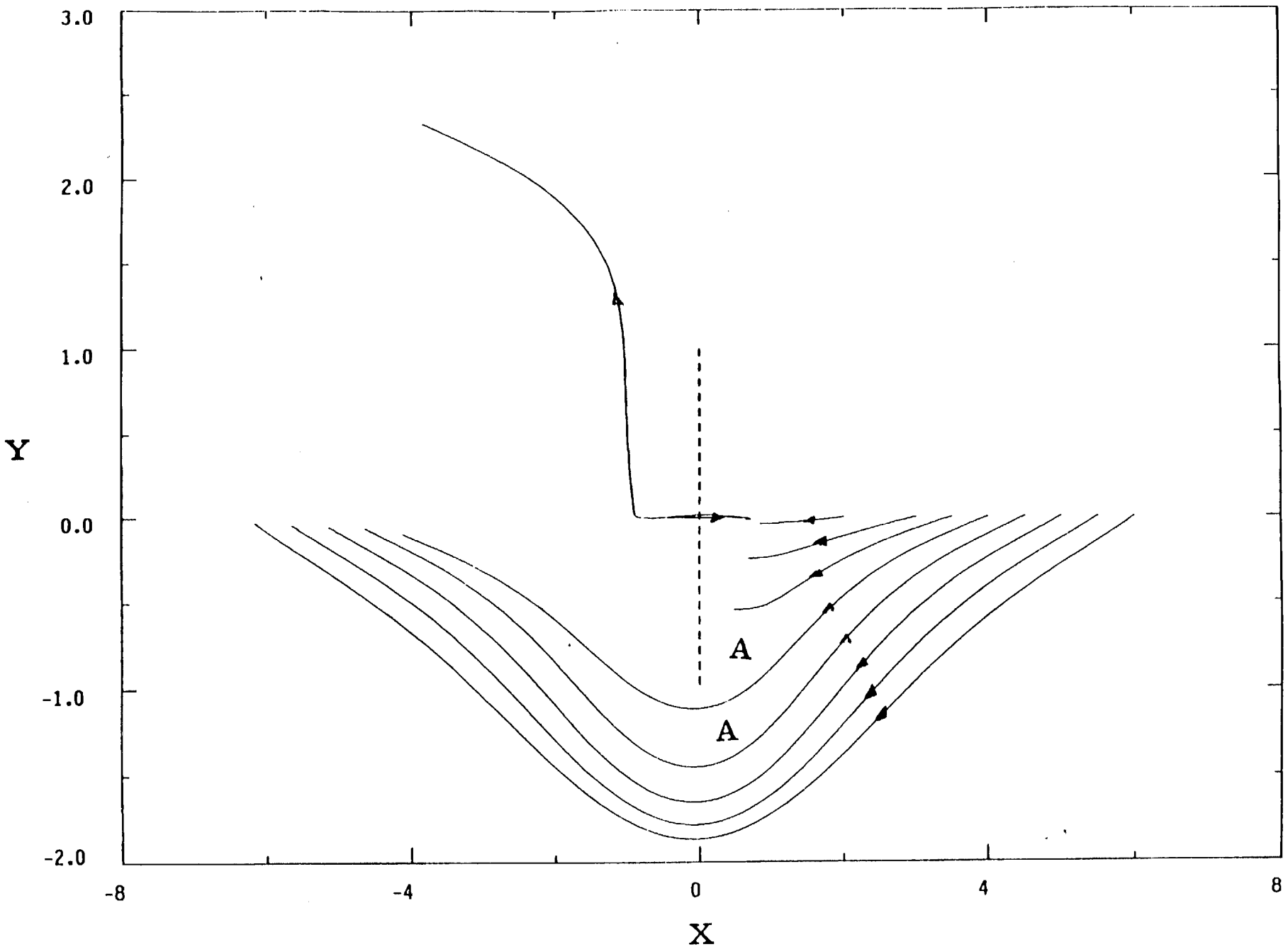

Fig. 5c

ELECTRON IMPACT POLARIZATION EXPECTED IN SOLAR EUV LINES FROM FLARING CHROMOSPHERES/TRANSITION REGIONS

S. Fineschi,[1] J. M. Fontenla,[2]
P. MacNeice,[3] and N. N. Ljepojevic[4]

To Appear In:

Proceedings of the Workshop on
Max '91/SMM Solar Flares: Observations and Theory
(held Estes Park, CO, June 3-7, 1990)

SPACE SCIENCE LABORATORY
PREPRINT SERIES
NO. 90-124

December 1990

[1]NRC/NAS Research Associate
[2]CSPAR University of Alabama in Huntsville
Huntsville, AL 35899
[3]NASA/Goddard Space Flight Center
Greenbelt, MD 20771
[4]University of Cambridge, U.K.

Electron Impact Polarization Expected in Solar EUV Lines from Flaring Chromospheres/Transition Regions

S. Fineschi,[1] *J.M. Fontenla,*[2] *P. MacNeice,*[3] *and N.N. Ljepojevic*[4]

[1]NASA Marshall Space Flight Center
Huntsville, Alabama, 35812

[2]CSPAR University of Alabama in Huntsville
Huntsville, Alabama, 35899

[3]NASA Goddard Space Flight Center
Greenbelt, Maryland 20771

[4]University of Cambridge, U.K.

Abstract

We have evaluated lower bounds on the degree of impact EUV/UV line polarization expected during solar flares. This polarization arises from collisional excitation by energetic electrons with non-Maxwellian velocity distributions. Linear polarization was observed in the S I 1437 Å line by the UVSP/SMM during a flare on 1980 July 15. An early interpretation suggested that impact excitation by electrons propagating through the steep temperature gradient of the flaring transition region/high chromosphere produced this polarization. Our calculations show that the observed polarization in this UV line cannot be due to this effect. We find instead that, in some flare models, the energetic electrons can produce an impact polarization of a few percent in EUV neutral helium lines (i.e., $\lambda\lambda$ 522, 537, and 584 Å).

I. Introduction

The aim of this paper is to find the amount of impact linear polarization expected to be present in atomic spectral lines formed in solar plasmas. This polarization arises because the steep temperature gradient of the transition region leads to non-Maxwellian velocity distributions of electrons carrying conductive heat flux.

The geometry of the adopted model is shown in Figure 1. The emitting upper chromosphere/transition region (hatched area, in Figure 1) of the loop is observed at the solar limb (where the polarization is largest). The curvature of that part of the loop is negligible, and the loop axis and the direction of the local magnetic field coincide with the solar vertical (Z axis). The pitch angle, θ, is measured from the loop axis. The temperature structure of these models is given by $T(s)$, where s is the distance to the loop apex along the magnetic field (or the loop axis). These models are described elsewhere (Ljepojevic and MacNeice, 1987; MacNeice, Fontenla, and Ljepojevic, 1990). The electron velocity distribution is

$$f = f\left(s, \mu, \frac{v}{v_T}\right) ,$$

where v_T is the electron thermal velocity and $\mu \equiv \cos\theta$. This distribution

- is *cylindrically symmetric* around the loop axis;
- follows the *Spitzer-Härm function* for $v < 2 \cdot v_T$ – this function is derived under the assumption of small deviations from Maxwellian, and can expressed as:

$$f\left(\mu, \frac{v}{v_T}\right) = \left[1 - \mu \cdot D\left(\frac{v}{v_T}\right)\right] \cdot M\left(\frac{v}{v_T}\right) , \qquad (1)$$

  where M is the Maxwellian function and D correspons to a perturbative expansion and we droped the variable s for simplicity;
- and is computed solving numerically the *high-velocity form of the Landau equation* (HVL) for $v \geq 2 \cdot v_T$ (Ljepojevic and MacNeice, 1989).

III. Emission-Line Polarization by Electron Impact

The impact polarization has been computed using a recent theoretical scheme based on the formalism of irreducible tensor operators (Fineschi and Landi Degl'Innocenti, 1989 and 1990a). In this scheme, the statistical equilibrium equations of a multi-level atomic system interacting with an electron beam are derived in full generality from the principles of Quantum Mechanics. The collisional excitation is calculated for electrons having arbitrary angular and velocity distributions. In this scheme, the effect of magnetic fields on the impact polarization can also be accounted for. This theory gives analytical expressions for the polarization cross sections of the electric multipole transitions due to atom-electron collisions, provided the Born approximation be assumed.

From the above-mentioned theory the presence of a magnetic field gives, for the emitted polarized radiation, a phenomenon similar to the well known Hanle-effect (i.e., impact

The degree of linear polarization is given by

$$P = \langle S_1 \rangle / \langle S_0 \rangle \,, \tag{4}$$

where

$$\langle S_i \rangle = \int_{v_0}^{\infty} dv \int_{-1}^{+1} d\mu \cdot f\left(\mu, \tfrac{v}{v_T}\right) \cdot S_i(v,\mu); \quad i = 0, 1. \tag{5}$$

Thus, for a given distribution f, the polarization, P, is a function of: the line wavelength λ; the electron temperature T; and the type of atomic transition, $J' \rightarrow J$. In the following, we restrict ourselves to lines where $J' \rightarrow J$ corresponds to $1 \rightarrow 0$. In this case there is no atomic depolarization, and the polarization is maximum, i.e., $W_{10} = 1$.

It is important to note that in the expression of $\langle S_1 \rangle$, the integral over μ corresponding to the part of f which follows the Spitzer-Härm function is

$$\langle S_1 \rangle \propto \int_{-1}^{+1} d\mu \cdot (1 - \mu \cdot D) \cdot (3\mu^2 - 1) = 0. \tag{6}$$

Therefore, no net polarization arises from the bulk of the distribution, and only the strongly anisotropic, high-velocity electrons in the tail are responsible for the polarization.

IV. Results

The results for the expected impact polarization can be expressed as $P = P(\lambda, T)$. For XUV/EUV/UV lines formed in the upper chromosphere/transition we show the "flare" case in Figure 2, and the "quiet Sun" case in Figure 3. In all cases, the direction of maximum polarization corresponds to the vertical. The results shown are for the transition $[J' = 1 \rightarrow J = 0]$.

The location of some lines which are observed in the Sun has been marked. For each of them the cross is drawn at the temperature where the emissivity (in $erg\,cm^{-3}\,s^{-1}$) peaks. The upper and lower ends of the bar correspond to the temperatures where the emissivity drops to about one third of the maximum. These temperature values were taken from the literature, where a Maxwellian electron distribution was assumed for the line-formation computations (Landini and Monsignori Fossi, 1990) and effects of the emitting ions diffusion are ignored. However, these diffusion effects may affect the actual ranges of temperature at which the lines are emitted, as shown by Avrett and Fontenla (1990).

The result plotted in Figure 2 shows that impact polarization by excitation of electrons carrying heat flux would be present in the EUV neutral helium lines 522, 537, and 584 Å.

where Q is a function of the electron velocity and is proportional to the temperature gradient. Consequently, the line polarization resulting from electrons having the Manheimer distribution is zero:

$$S_1 \propto \int_{-1}^{+1} d\mu\,(3\mu^2 - 1) \cdot [1 + Q \cdot (\mu^3 - 3\mu)] = 0. \tag{8}$$

The original Manheimer function was modified by Hénoux *et al.* (1983b) replacing its negative values – physically meaningless – by zero in the range $1.5v_T < v_z < 3v_T$ ($v_z = v \cdot \mu$). This procedure was first suggested by Shvarts *et al.* (1981). We show in Figures 4 and 5 the distribution function we computed, and compare it with the Manheimer and the modified Manheimer functions. In Figure 6, we show the angular distributions which result from our calculation, and we compare it with the modified Manheimer values. The ordinate in this figure reflects the contribution of particular energy electrons to impact polarization. All these figures show that the modified Manheimer function is strongly anisotropic, and in fact *all the impact polarization in Hénoux et al. (1983b) calculations is due to such modification of the original Manheimer function.* For a line excitation energy (threshold energy) corresponding to a few times the thermal energy, the modified Manheimer distribution gives rise to high values of polarization, much larger than the ones obtained in our more accurate treatment. Moreover, for this modified Manheimer function the significant departure from an angular distribution which results in zero line polarization (cfr. eq. [8]) occurs at a lower range of electron velocities ($\sim 1.5 - 2\,v_T$) compared to our treatment ($\sim 3 - 3.5\,v_T$). Thus, by assuming the modified Manheimer function, UV lines with relatively low threshold energy (viz., long wavelengths) can be excited by electrons which already have strongly anisotropic velocity distribution, producing in this way large impact polarization in the line. On the contrary, if we consider the distribution we computed, the low threshold energy lines are mostly excited by electrons having almost isotropic distribution, and thus low impact polarization results (see Fig. 6). Therefore, the only spectral lines which are expected to show strong polarization are those with a threshold energy large enough so that line excitation is predominatly by highy suprathermal electrons ($v \geq 3v_T$). The neutral helium lines ($\lambda\lambda$ 522, 537, and 584 Å), in the EUV wavelength regime, would fulfil this requirement.

As final remark, we point out that this result does not take into account the depolarizing effect due to radiative transfer in these resonance lines. This effect would be important for large optical thickness, τ, of the line emitting region. Optical thickness of EUV helium lines in solar flares depends on a variety of conditions of heating and irradiation of the

and bombard the chromosphere. Proton beams have been proposed by Simnett (1986) to be important in some flares.

In order to assess the relative role played in solar flares by high or low energy electron beams and by proton or neutral beams, further Hα measurements as well as EUV observations with new imaging polarimeters (Fineschi *et al.*, 1990b; Hoover *et al.*, 1990) are highly needed.

Acknowledgments

We thank Marcos Machado for reading the manuscript and giving us valuable suggestions. This paper was completed while S. Fineschi held a National Academy of Sciences/NRC research associateship. J.M. Fontenla acknowledges support from NASA Space Physics Division of the Office of Space Science and Applications through grant NAGW – 2096.

References

Avrett E. H., and Fontenla J. M. 1990, in "Mechanisms of Chromospheric and Coronal Heating," *Proceedings of Heidelberg Conference*, eds. P. Ulmschneider, E. Priest, and R. Rosner (Heidelberg, Germany).

Fineschi, S., and Landi Degl'Innocenti, E. 1989, *J. Math. Phys.*, **31** (5), 1124.

Fineschi, S., and Landi Degl'Innocenti, E. 1990a, *Ap. J.*, submitted

Fineschi, S., Hoover, R. B., Fontenla, J. M., and Walker, A. B. C. 1990b, in "X-ray/EUV Optics for Astronomy, Microscopy, and Projection Lithography," **1343**, *Proceedings SPIE*, eds. R. B. Hoover and A. B. C. Walker (San Diego, CA).

Hénoux, J. C., Chambe, G., Semel, M., Sahal, S., Woodgate, B., Shine, R., Beckers J., and Machado, M. 1983a, *Ap. J.*, **265**, 1066.

Hénoux, J. C., Heristchi, D., Chambe, G., Machado, M., Woodgate, B., Shine, R., and Beckers, J. 1983b, *Astron. Astrophys.* **119**, 233.

Hénoux, J. C., Chambe, G., Smith D., Tamres D., Feautrier, N., Rovira, M., and Sahal-Bréchot, S. 1990, *Ap. J. Suppl.*, **73**, 303.

Hoover, R. B., Fineschi, S., Fontenla, J. M., and Walker, A. B. C. 1990, in "X-ray/EUV Optics for Astronomy, Microscopy, and Projection Lithography," **1343**, *Proceedings SPIE*, eds. R. B. Hoover and A. B. C. Walker (San Diego, CA).

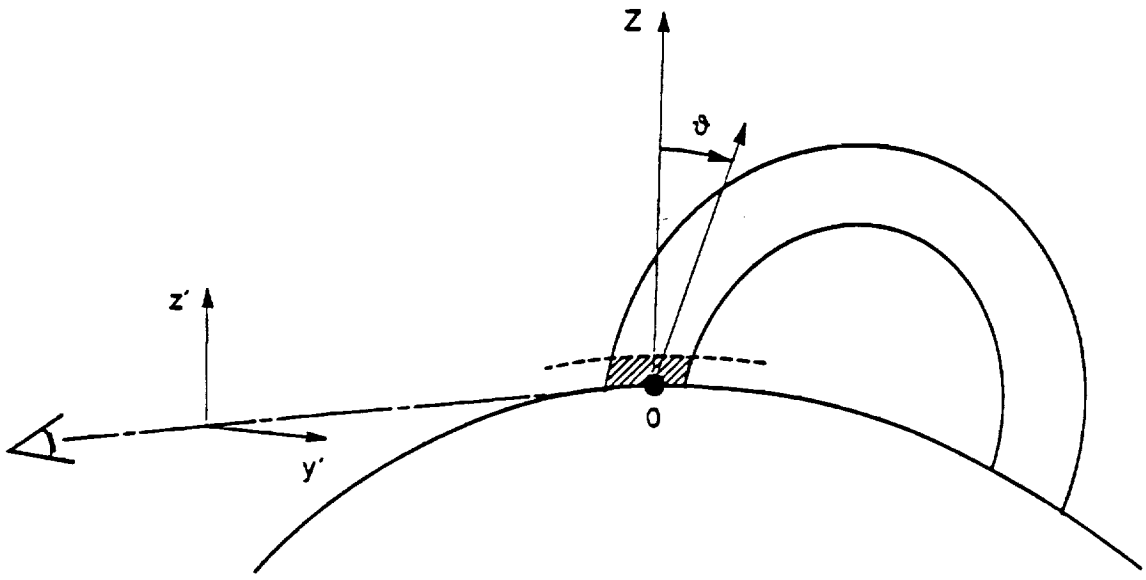

Figure 1. Geometry of the loop model and coordinate system for the calculation of the Impact linear Polarization. The emitting upper chromosphere-transition region (hatched area) of the loop is observed at solar limb. The curvature of that part of the loop is negligible, the loop axis and the direction of the local magnetic field coincide with the solar vertical, Z. The pitch angle, θ, of the electrons is measured from the loop axis.

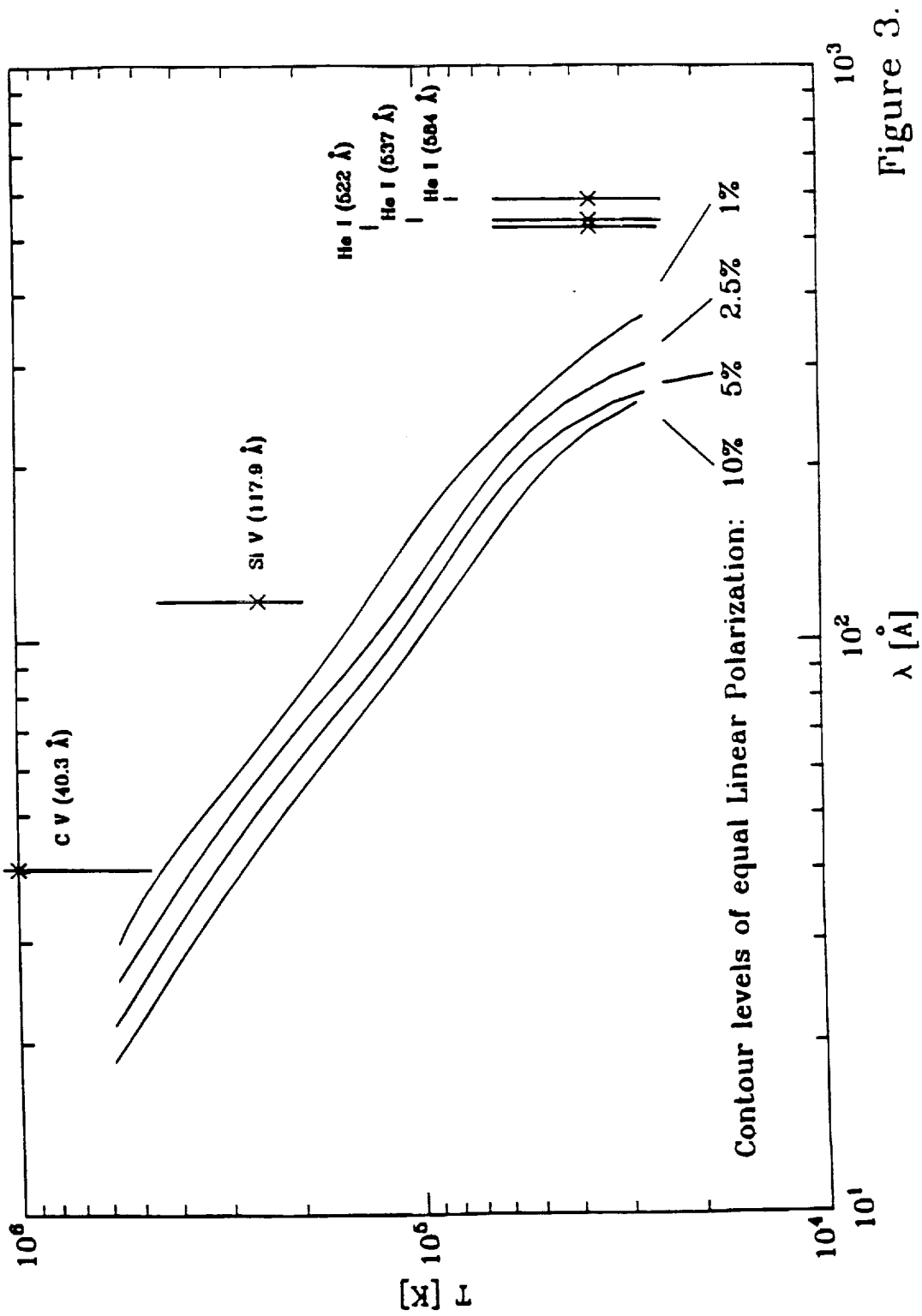

Figure 3.

ANISOTROPY OF THE ELECTRON DISTRIBUTIONS

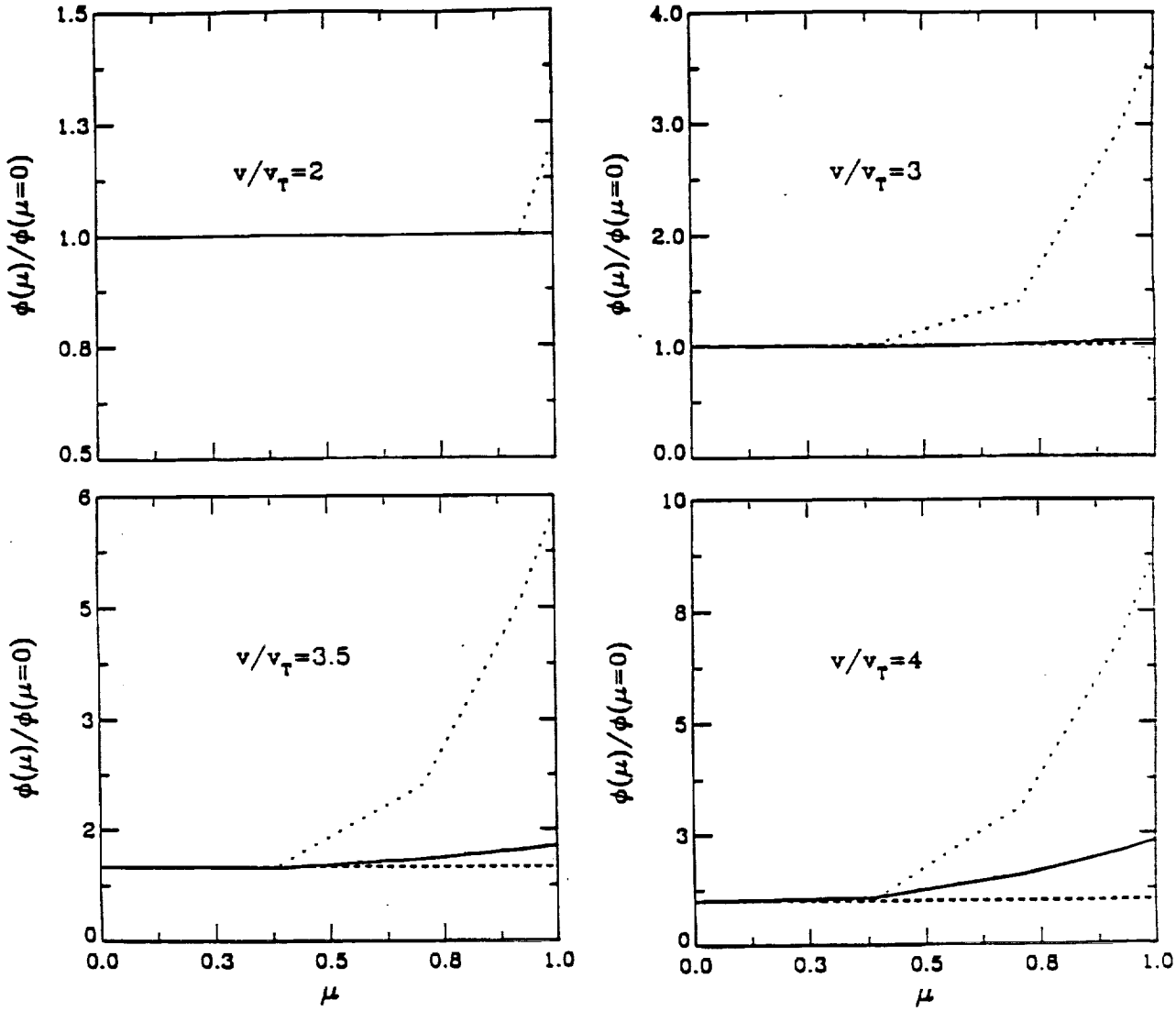

Figure 6. Plots of the symmetrical part,

$$\phi(\mu) \equiv \tfrac{1}{2} \cdot \left[f\left(+\mu, \tfrac{v}{v_T}\right) + f\left(-\mu, \tfrac{v}{v_T}\right) \right] ,$$

of the Spitzer-Härm+HVL (solid line) and of the modified Manheimer distribution (dotted line). (Dashed line: Maxwellian).